PRODUCTION OF ALUMINIUM BASED COMPOSITES REINFORCED WITH EMBEDDED NiTi BY FRICTION STIR WELDING

Luís Gonçalves Mendes

Dissertação para a obtenção do grau de Mestre em

Engenharia Mecânica

Orientadora: Professora Doutora Rosa Maria Mendes Miranda,
Faculdade de Ciências e Tecnologia
Co-orientador: Professor Doutor Telmo Jorge Gomes dos Santos,
Faculdade de Ciências e Tecnologia

Dezembro de 2012

AGRADECIMENTOS

Gostaria de expressar minha gratidão a todos aqueles que, de alguma forma, estiveram envolvidos nesta investigação, sem os quais teria sido impossível apresentar este trabalho.

À Professora Rosa Miranda a minha mais profunda gratidão, por me convidar para este desafiador e pioneiro projeto, pelo apoio dado, pelo interesse despertado e tempo investido e pelos conhecimentos transmitidos ao longo deste curso.

Ao meu co-orientador o Professor Telmo Santos pelo seu apoio e trabalho em domínios cruciais para o desenvolvimento desta investigação.

Ao Professor Pedro Vilaça pelas instalações e suporte técnico durante o trabalho experimental na STM IST.

Também, a minha gratidão para com o Professor Pamies Teixeira pelo seu aconselhamento muito bem-vindo.

À Professora Raquel Brás pelo seu interesse e apoio, nos ensaios de vibração.

Gostaria de agradecer ao Professor Braz Fernandes por todo o seu apoio, tempo investido, interesse e pelo material fornecido. Bem como ao Professor Mahesh e Professor Alexandre Velhinho.

À Professora Virgínia Infante pelo apoio técnico e caracterização mecânica realizada no IST.

A minha profunda gratidão ao Mestre João Gandra pela total disponibilidade e energia, sem a qual, não teria sido possível realizar este trabalho. Acima de tudo, pelo apoio e amizade.

Ao Sr. António Campos e Sr. Paulo Magalhães para a sua assistência e amizade.

Um agradecimento especial à minha família e amigos, que a seu modo, foram cruciais para a elaboração deste trabalho.

AKNOWLEDGMENTS

RESUMO

As ligas de alumínio têm sido amplamente utilizadas em materiais compósitos de modo a promoverem uma melhoria das suas propriedades enquanto reduzem o peso. Na produção de compósitos com uma grande diferença de propriedades mecânicas e termofísicas a soldadura por fusão, devido às elevadas temperaturas, aumenta a formação de intermetálicos indesejáveis. Essas limitações têm levado ao estudo de processos de ligação no estado sólido, como a soldadura por fricção linear (SFL), para unir diferentes materiais.

Neste trabalho estudou-se a possibilidade de criar compósitos de ligas da série AA 1XXX reforçados com NiTi por SFL. Foram investigadas diferentes formas do material de reforço, analisadas as interfaces e os fluxos de material resultantes e caracterizados os compósitos produzidos. Observou-se um aumento de 70% da tensão de ruptura, em relação ao substrato de Al e a ligação entre os dois materiais dissimilares suporta tensões superiores às da ruptura do Al numa junta sobreposta. O compósito produzido apresenta uma conductividade eléctrica de cerca de 62 % IACS, reduzindo menos de 3% IACS em relação à do substrato de Al. Produziu-se assim um compósito com uma forte ligação mecânica entre ambos os materiais, mantendo as propriedades funcionais do NiTi e eléctricas do Alumínio.

PALAVRAS-CHAVE

Compósitos de matriz metálica

Soldadura por friccção linear

Ligação soldada

AA 1100

NiTi

ABSTRACT

Aluminium alloys have been widely used in composite materials in order to promote an enhancement in its properties while reducing weight. As in the production of new composites with a significant difference in mechanical and thermo-physical properties fusion welding processes enhances the formation of undesired intermetallics. Those limitations have driven research on solid state technologies, such as Friction Stir Welding (FSW), for joining dissimilar materials.

This study aimed to develop composites in AA 1XXX series aluminium alloys with NiTi by FSW. Different reinforcing material shapes were investigated, analyzed the interfaces and the resulting material flow. The final product was mechanically characterized. It was observed an increase of 70 % of ultimate tensile strength, compared to Al base material and yielding between the two dissimilar materials was greater than the Al lap joint yield stress. The final composite depicted a good electrical conductivity, reducing less than 3 % IACS of the Al base material. Thus, a composite with a strong mechanical bonding was produced, maintaining the original functional properties of the reinforcement NiTi alloy, and the electrical properties of the Aluminium.

KEY-WORDS

Metal matrix composite

Friction stir welding

Joining

AA 1100

NiTi

TABLE OF CONTENTS

x

FIGURE LIST

TABLE LIST

GLOSSARY OF ACRONYMS AND SYMBOLS

Notation	Description	Unit
AA	Aluminium alloy	
A_f	Austenitic finish temperature of the B19'→B2 transformation	K
A_p	Austenitic peak temperature of the B19'→B2 transformation	K
AS	Advancing side	
A_s	Austenitic start temperature of the B19'→B2 transformation	K
CTE	Coefficient of thermal expansion	K^{-1}
d_{pin}	Pin diameter	mm
ζ	Damping ratio	
δ	Logarithmic decrement	
EDS	Energy dispersed spectroscopy	
EST	Effective sheet thickness	%
$\dot{\epsilon}$	Strain rate	
FSP	Friction stir processing	
FSW	Friction stir welding	
HAZ	Heat affected zone	
HIDAMETS	High damping metals	
IACS	International annealed copper standard	%
IF	Internal friction	
IMC	Intermetallic compound	
l	Minimum distance between pin interfaces in consecutive overlap passes	mm
L_e	Depth of the dynamically recrystallized zone	mm
LPPD	Low-pressure plasma spray	
M_f	Martensitic finish temperature of the B2→B19' transformation	K
MMC	Metal-matrix composite	
M_p	Martensitic peak temperature of the B2→B19' transformation	K
M_s	Martensitic start temperature of the B2→B19' transformation	K
NASA	National Aeronautic and Space Administration	
OM	Optical microscopy	
OR	Overlap ratio	
PcBN	Polycrystalline cubic boron nitride	
PD	Plunge depth	mm
PET	Percentage effective thickness	%
PH	Pin height	mm
Pitch	Distance travelled by the tool along the welding direction in one	mm /rev

	revolution	
Q	Activation energy for diffusion	J/mol
R	Gas constant	J/mol·K
r_e	Radius of the dynamically recrystallized zone	mm
R_f	Rhombohedral finish transformation temperature	K
R_m	Average material flow rate	
R_p	Rhombohedral peak transformation temperature	K
RS	Retreating side	
R_s	Rhombohedral start transformation temperature	K
SE	Superelastic effect	
SEM	Scanning electron microscopy	
SMA	Shape memory alloy	
SME	Shape memory effect	
SPD	Severe plastic deformation	
SWW	Sound weld width	mm
SZ	Stirred zone	
T	Temperature	K
t_0	original thickness of lap jointed sheet	mm
TA	Tilt angle	°
t_e	Reduced thickness of lap jointed sheet	mm
TMAZ	Thermo-mechanically affected zone	
UTS	Ultimate tensile strength	
ν	Traversal velocity of the FSW/FSP tool	mm/min
ω	Angular velocity of the FSW/FSP tool	rev/min
$ω_n$	Natural frequency	rad/s
$ω_f$	Forced frequency	rad/s

1.   INTRODUCTION

1.1.   Motivation

Metal matrix composites (MMCs) are one of the most important class of composites for structural, thermal and kinetic applications. They consist of two or more materials chemically and/or mechanically bounded with distinctive interfaces between them. A multitude of production technologies have been searched. Production methods can be separated into two large technological groups: Liquid state, where one or more materials are melted; solid state, where none achieve its melting point, and viscoplastic and diffusion mechanisms ensure the final material integrity.

High purity aluminium alloys show a good electrical conductivity and but low hardness and tensile strength. In fact, aluminium alloys are largely used in industrial applications due to their good oxidation and corrosion resistances and light weight. AA 1100 exhibit poor mechanical resistance, but good electrical conductivity which is relevant for specific electrical applications.

Limited research work exist on Friction Stir Welding of AA 1100 aluminium alloys but, the possibility to join this formable alloy with very dissimilar and hard alloys by FSW is promising. NiTi is well known for its functional properties as shape memory effect and superelasticity. A metal matrix composite, produced by FSW, with good electrical conductivity and functional properties is thus of scientific interest.

The motivation for this work was to develop a composite using AA 1xxx alloy and embedded NiTi material, the former has good thermal and electrical properties, the second has a superelastic and thermal induced phase change behavior. Since both materials have very different properties, Friction Stir Welding was investigated in this application – where the resulting material can have potential applications.

1.2.   Objectives

The overall aim of this investigation was to produce Al based composites reinforced with NiTi by FSW and characterize the composite produced. Specific objectives were:

1. Develop a FSW technique based on lap joining Aluminium alloys with reinforcements (those being very distinctive materials), in order to achieve bonding between the material and the reinforcement.

2. Exploit several strategies for positioning the reinforcing materials prior to processing.

3. Test the influence of tool geometry (pin height) to produce multi-step weld passes and the effect of processing parameters on the quality of the joint (in depth and on the surface).

4. Characterize the composites produced for mechanical, thermal and electrical properties.

1.3.   Structure

The thesis is structured into five chapters. Chapter 2 outlines the current state of the art, from a theoretical background, common terminology and technologies for producing composites.

Chapter 3 identifies the materials used and provides a concise description on the experimental methodology, including the characterization techniques adopted.

Chapter 4 presents and discusses the results of this investigation.

Chapter 5 gathers final conclusions and presents future work proposals for improving the developed technique.

# 2.	STATE OF THE ART

## 2.1.	Composite Materials

It is a truism that the field of materials is a building block of technological development. Although in its bulk state they have shown great improvements, it is in composite materials that they truly break ground to an ever increasing attempt of optimization in materials. The capability to scramble along with different materials can, theoretically, create infinite new possibilities. It is fairly easy to understand how a bulk of Aluminium alloy, with a high specific strength but poor surface properties, would improve if a ceramic coating could provide its very own attractive properties, in a sandwich type geometry.

A composite material is a multi-phased material, manufactured with two or more physically and/or chemically distinct well deployed phases, with a distinctive interface between them. It acquires properties that are not exhibited by any individual material [1-3].

Composites are classified according to their matrix material. The main classes are polymer-matrix, cement-matrix, metal-matrix, carbon-matrix and ceramic-matrix composites [2]. Figure 2.1 summarizes the major fields of application of each class of composites and it is clear from this the impact composites had in industry.

There has been a tremendous increase in applications of composites in sophisticated engineering items. Modern aircraft group Boeing launched his latest model in 2011, the 787, with 50% of the materials being composites [4].

It is noticeable the wide range of applications for polymer-matrix composites besides high temperature, due to poor high-temperature resistance. Electrical applications are also interesting, limited to polymer and ceramic-matrix composites, which provide better insulation and semi-conductor properties.
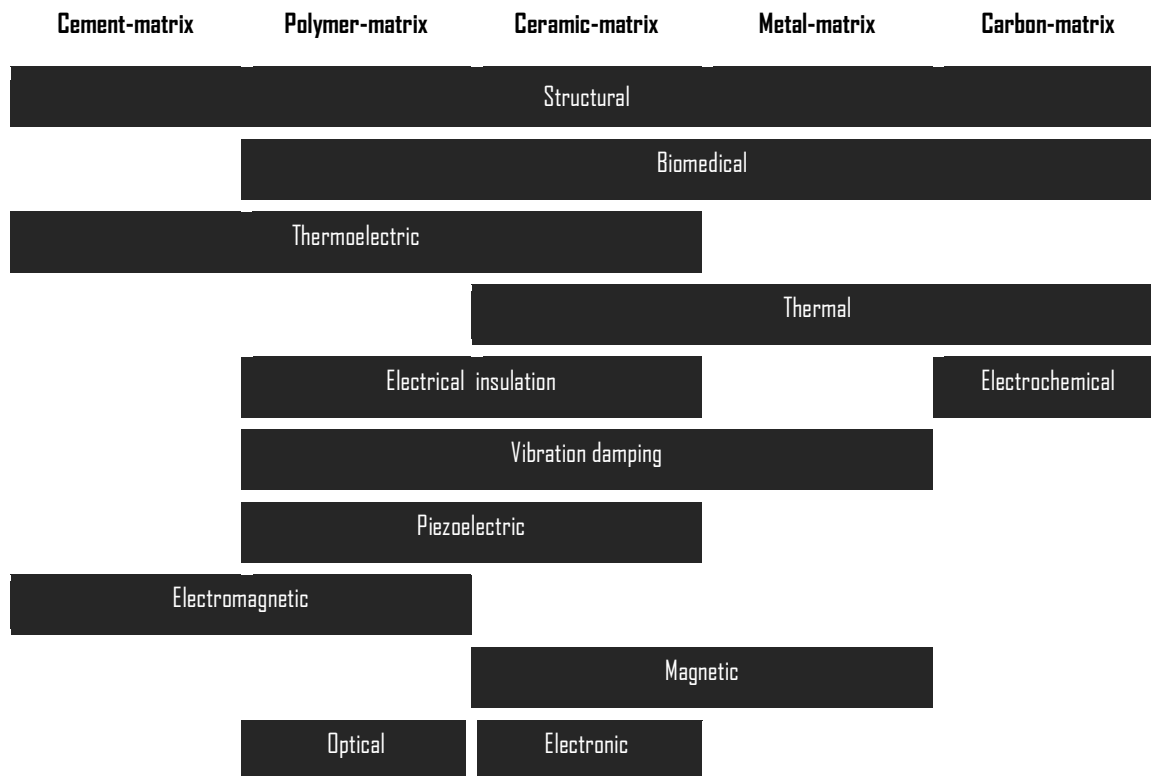
Figure 2.1 – Representative chart of engineering domains incorporating composite materials.
Adapted from [2, 3, 5]

Carbon-matrix is one of the most important composites in electrochemical, due to its electrical conductivity and chemical inertness [6]. Another development was the integration of materials knowledge with manufacturing technologies aiming to improve overall properties of composites, satisfying design requirements along with concepts of product life-time from design to disposal. Figure 2.2 depicts the properties of composite material compared to bulk individual ones, emphasizing the benefits in terms of mechanical resistance and weight.
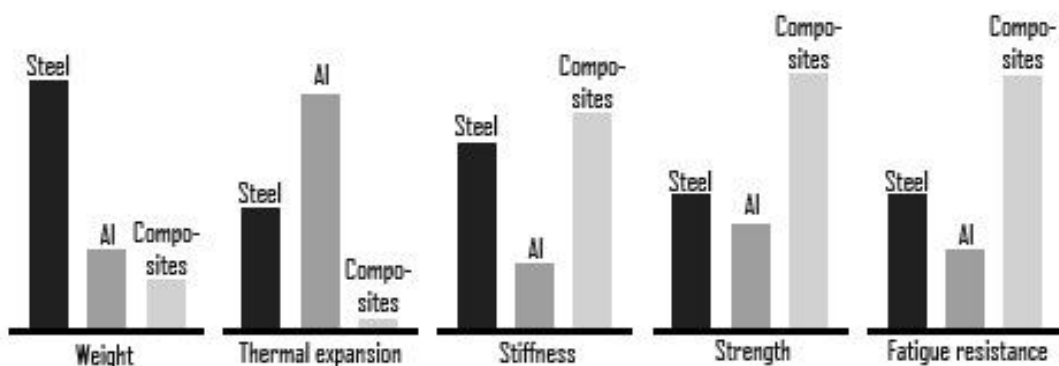
Figure 2.2 – Comparison between conventional bulk materials and composite materials [1].

Metal matrix-composites have gained importance in thermal applications, since the beginning of the 1960's, when boron metal-matrix combined the fire resistance of boron with the structural properties of aluminium alloys for aerospace purposes. Nowadays, research aims to reduce the coefficient of thermal expansion (CTE) while increasing strength and Young modulus [2]. The same author reports on the interest in damping metal-composites, particularly, in the combination of structural lightweight materials with super-elastic materials (with high damping capacity). This structure should confine the capacity of vibration absorption thus avoiding redundant damping systems. Most developed MMCs are lightweight metal-matrices containing high-strength ceramic reinforcements [5].

Figure 2.3 illustrates three different MMC plate combinations and those are: (a) homogeneous orthotropic composite, (b) fiber reinforced composite (c) laminated composite.
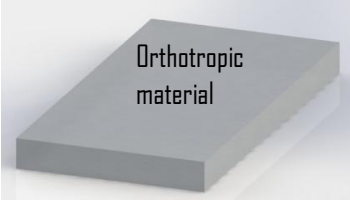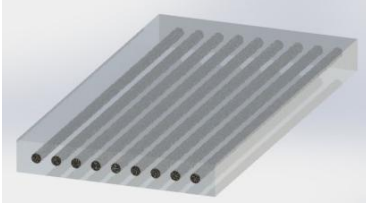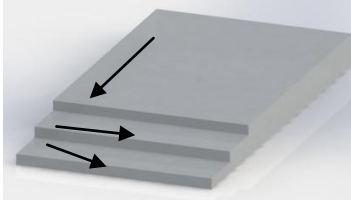
(a) Particle reinforced	(b) Fiber-reinforced	(c) Structural
• Large particle	• Continuous (aligned)	• Laminated
• Dispersion strengthened	• Discontinuous (short) – aligned or randomly oriented	• Sandwich panels

Figure 2.3 – Classification scheme for the various composite types.

Laminated composites are the most common MMC available [5], each layer being of a different material or the same material in a different pattern (figure 2.3 c). Thus, there is a physical layer distinction along the thickness of the composite material, and these can be joined by various processes, further discussed in section 2.3.

The most common laminated composites are sandwich configuration, they result of an assembly by bonding (or welding) two surfaces on a lighter bulk which maintains its distinctive interface [3]. Moreover, "sandwiches" have a good strength-to-weight ratio, can bear much higher loads than its original bulk shapes and have exceptional thermal properties. On the down side, they present risk of buckling failure and layer delamination.

In Fiber reinforced composites, the added fibers have high Young modulus and very low diameter to length ratio (commonly not exceeding 100 µm of section width). Fiber reinforcement improves stiffness by incorporating high-modulus fibers in the metal-matrix can be also advantageous by reinforcing the whole material with lighter fibers.

This results in a lighter but stiffer composite, which from a structural perspective, has a maximized E/ρ^2. Figure 2.4 allows to understand the type of materials that can be used to improve a structural composite. Tungsten alloys (W alloys) have high modulus and density, while aluminium alloys are usually light and soft.
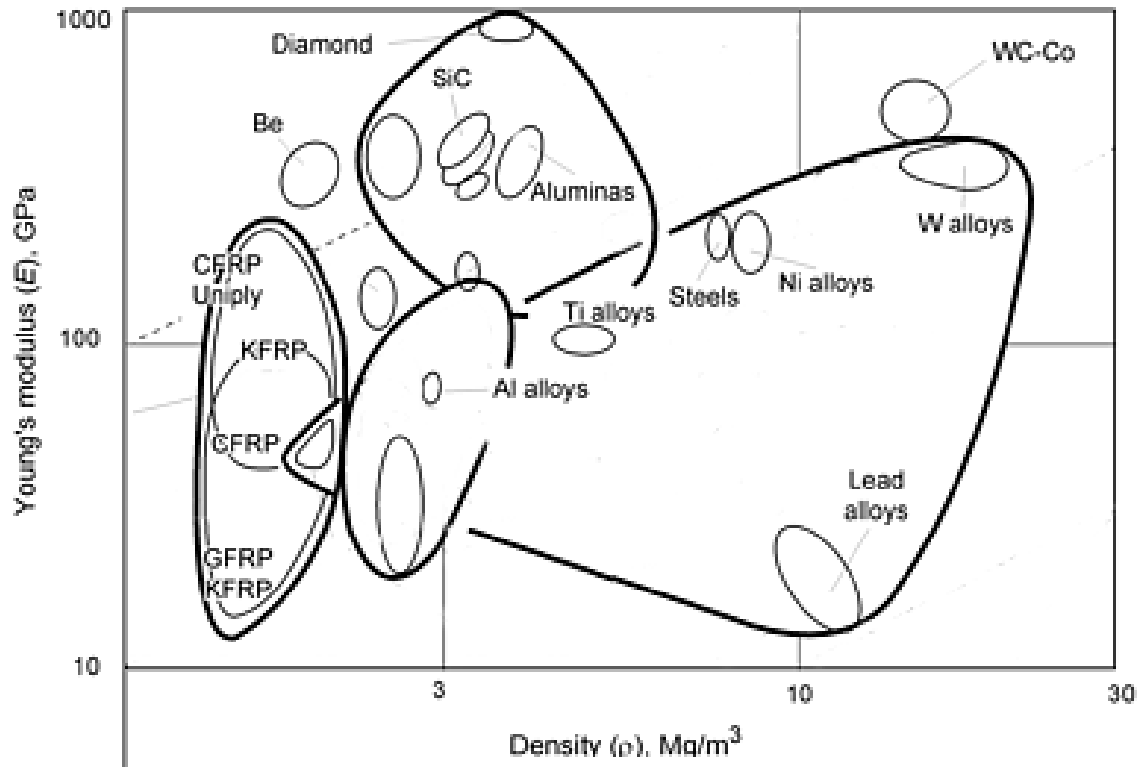
Figure 2.4 – Young modulus plotted against density for various engineering materials [7].

Thin (less than 1mm) high carbon steel wires can have very high strength levels (~5GPa), despite having low toughness at high strengths [1]. Table 2.1 summarizes the major properties for some commercial metallic wires.

Table 2.1 – Typical properties of some commercial metallic wires [1].

Material	Diameter (μm)	Density (g·cm^{-3})	Tensile strength (MPa)	Young's modulus (GPa)	Coefficient of thermal expansion ($10^{-6} \cdot K^{-1}$)	Melting point (ºC)
Steel, 0.9%C	100	7.8	4250	210	11.8	1300
Stainless steel, 18-8	50-250	8.0	700-1000	198	18.0	–
Beryllium	–	1.85	1260	300	11.6	1280
Tungsten	<25	19.3	3850	360	4.5	3400
Molybdenum	<25	10.2	2450	310	6.0	2600

6

The type of bonding can be split into: (a) chemical bonding and (b) mechanical bonding.

(a) Chemical bonding refers to a microstructural bonding provided by a good wettability condition – that is the extent at which a liquid spreads on a solid surface, or how the contact is at their atomic scale – resulting in interaction between components at an electronic scale and the atomic transport, controlled by a diffusion process.

(b) Mechanical bonding recalls to simpler mechanical locking, or keying effects, between materials. The internal compressive forces of the metal-matrix with the reinforcing fibers have been reported to create an effective composite [8, 9]. A composite fracture surface is depicted in figure 2.5 showing a brittle fracture and a diameter reduction just beneath the fracture, due to local load transfers. The same study, reported by Vennett *et al.* [10], investigated the occurrence of multiple necking in tungsten fibers, and discussed local load transfer from the wire to the surrounding matrix.
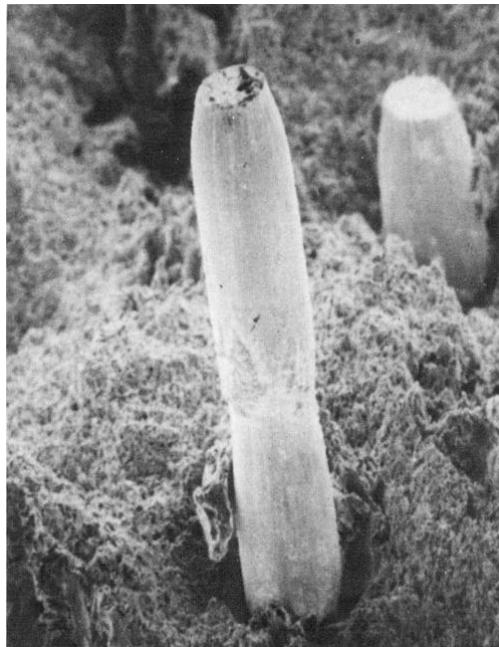
Figure 2.5 – SEM image of a tungsten wire at composite fracture [10].

2.2.   Shape memory alloys for composite damping enhancement

It was not until 1962, when Buehler, first discovered the effect of equiatomic NiTi alloy. In no more than 10 years first Nitinol™ commercial products hit the markets, and since then SMA captured definitely the interest of the scientific community [11].

The main characteristics of SMA are the superelastic effect (SE), reversible deformations at very high strains and shape memory effect (SME): the ability of recovering their original shape after being deformed [12]. SME may be further defined as yielding a thermoelastic martensite. In this case, the alloy undergoes a martensitic deformation by a twinning mechanism, as figure 2.6 illustrates, bellow the transformation temperature. The twinning deformation is then reversed upon heating to the parent austenitic phase. According to Callister [13] mechanical twinning occurs mainly in metals that have BCC and HCP crystal structures, at low temperatures or at high loading rates (*e.g.* shear stress induced martensite), conditions under which the slip deformation process is restricted, due to few operable slip systems.
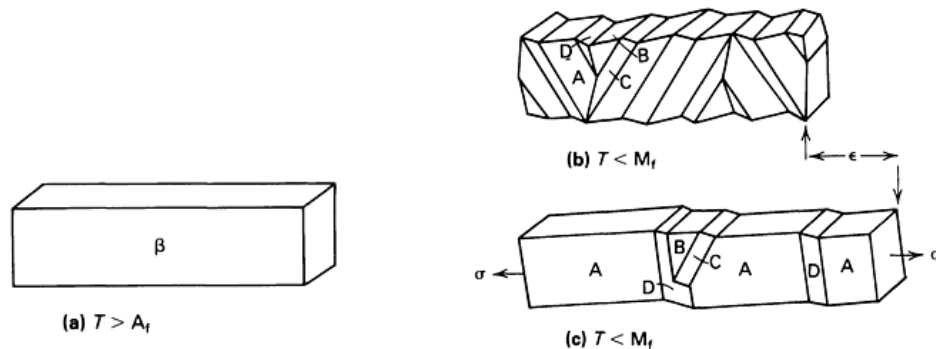
Figure 2.6 – (a) A β phase crystal. (b) Self-accommodating, twin-related variants A, B, C, and D, after cooling and transformation to martensite. (c) Variant A becomes dominant when stress is applied [11].

NiTi is an ordered intermetallic compound. According to the phase diagram in figure 2.7, they attain a stable phase down to room temperature; however the stoichiometric range is equiatomic at ambient temperatures. Dixit *et al.* [12] indicates an atomic ratio of the powders used in his experience of Ni 55 %, Ti bal.; Paula *et al.* [14] applies a NiTi alloy with Ni 49 %, Ti bal., annealed at 600, 700 and 800 ℃ for 60 min, and water quenched to room temperature; Tobushi *et al.* [15] used a Ni 49.82 %, Ti bal., on the experiment.
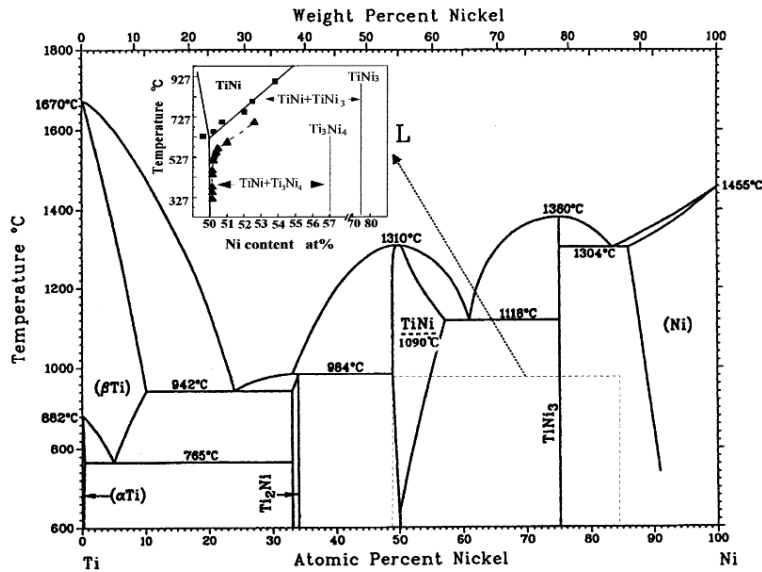
Figure 2.7 – Binary Ti-Ni alloy phase diagram [16].

Figure 2.8 depicts a common thermal induced heat flux phase change cycle, measured by differential scanning calorimetry (DSC). This cycle can be repeated in a two-way shape memory effect, the SMA can be deformed below M_f and, when heated, it returns to its original shape [12].

Between phase transformations, thermal flux analysis shows a phase change in the heating cycle with a single endothermic peak corresponding to the B19'-B2 phase change. In the cooling cycle, there are two exothermal peaks, corresponding to a two-stage B2-R-B19' phase transformation [14], although the latter R-phase transformation depends on the stoichiometry of the NiTi alloy and the thermo-mechanical treatments undergone by the material.
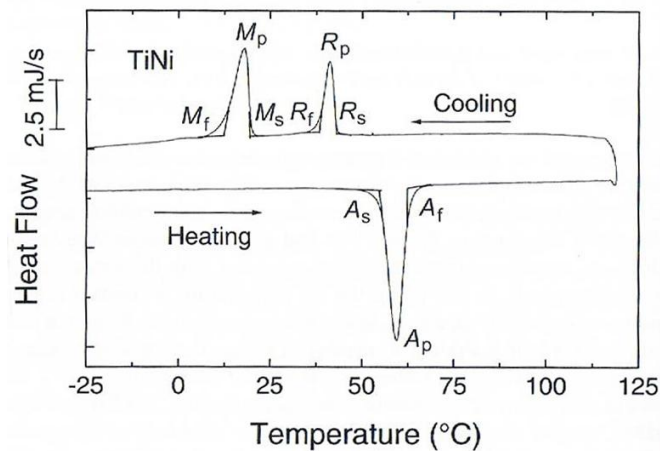
Figure 2.8 – DSC measurement of a NiTi alloy with a Ti content of 50 at.% [17].

Ti-rich and completely annealed equiatomic alloy undergoes a single-stage martensitic transformation (B2-B19´). In Ni-rich alloys and thermomechanically treated equiatomic alloys a two-stage transformation is observed.

High damping metals (HIDAMETS) have unique structural benefits (*e.g.* the high recover rate from induced vibrations, see figure 2.9), internal friction is the capacity of a material to convert its mechanical vibration energy into heat that is dissipated outwards [18].
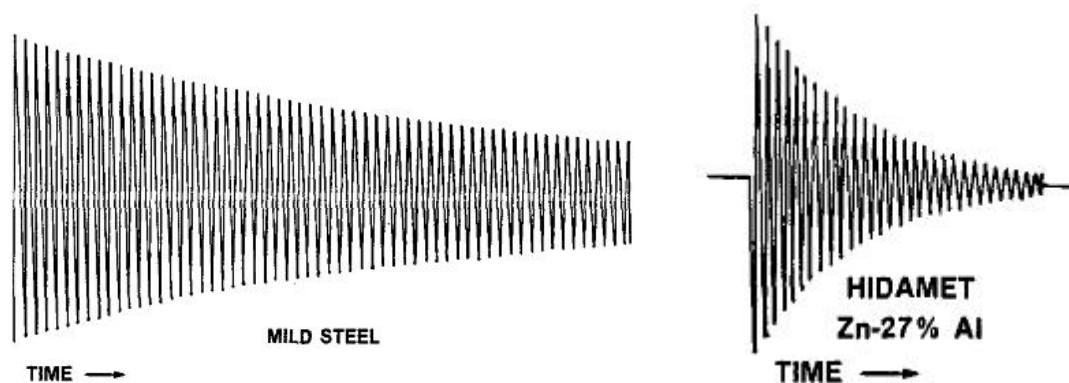
Figure 2.9 – Comparison of free-decay damping curves at low frequencies (~5Hz) for mild steel and for Zn-Al HIDAMETS [18].

Damping mechanisms, in general, involve the stress induced movement of defects (heterogeneities) on the microstructural level greatly increasing damping of a composite. Dislocations, precipitates, incongruent crystal structures are some of the responsible 'deflectors' of vibrations [19]. For HIDAMETS, the major mechanisms are stress-induced movement of dislocations or planar defects. Some metallic material exhibit a high level of damping in the region of a phase transformation – for example, in the temperature range of a thermoelastic martensitic transformation of smart materials, or shape memory materials, where the energy dissipated per unit of volume is much higher than in commonly used elastomers.

Specially, Cu-Zn-Al alloys shape memory materials exhibit the highest damping capacity of all HIDAMETS [20]. The two main material phases, austenitic and martensitic, result in two distinctive energy absorption mechanisms: From the austenitic phase, the superelastic reversible response is capable of absorbing energy in tensile cycles; in the martensitic phase, an irreversible energy absorption hysteresis is also responsible for energy absorption, upon changing between tensile or compression states. Although the origin of energy loss is not clear, a mobile and ordered dislocation network has been pointed out as the cause for damping increment [20]. Gandhi *et al.* [21] refer that if SMAs could be integrated into structures, several potential advantages over traditional damping materials could arise. Clearly, high damping capacity and controllability of SMA-based damping systems make them attractive candidates for composites with active damping functions.

10

Nitinol™ has been applied in the so-called 'kinetic applications'. Keats *et al.* [22] studied the feasibility of SMA phase temperature change for resonant frequency filters. Nagaya *et al.* [23] studied the applicability of SMAs for resonant control of rotating shafts at critical speeds. The same author refers a principle of the active control method, the capability of SMA to change phase (heat-induced) alters the material overall stiffness, and thus avoids the resonance zone in forced vibration modes. The correspondent "on" and "off" heating controls are illustrated in figure 2.10.
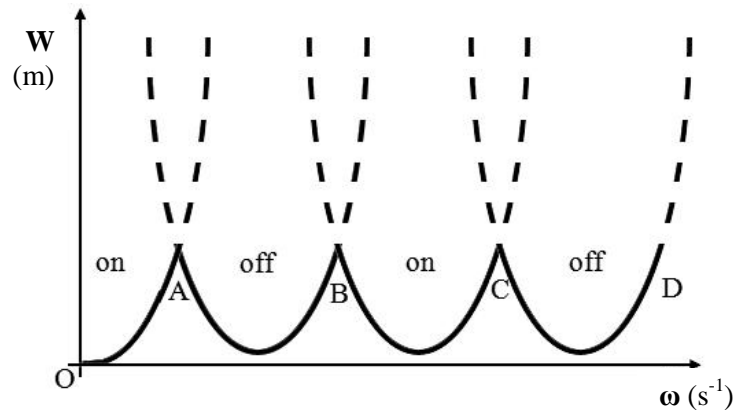
Figure 2.10 – Geometry of the principle of the method for passing through critical speeds.
W – amplitude, ω – natural frequency, OABCD path of the SMA designed response curve, dashed lines resonance zone.

Limited work was reported on the use of NiTi in the production of metal-matrix composites. An attempt was made to add NiTi powders in the surface of aluminium alloys, by Dixit *et al.* [12], with limited results due to the manufacturing methodology adopted. According to Dixit, considerable interfacial reactions developed between the SMA and the matrix material, which generated unwanted intermetallic particles such as Al_2O_3, Al_3Ti, Al_3Ni, Ni_3Ti and Ti_2Ni.

Blair London *et al.* [24] studied the friction stir processing of NiTi with $A_f = 15.0$ ºC, 49.2 % Ti and 6.35 mm plate thickness. After processing, the plate was hot-rolled for a 76 % total reduction. This process produced excessive flash and irregular surface weld beads, although tensile tests show that after hot-rolling the NiTi is stiffer and the process alters transformation temperatures and superelastic plateaus, compared to base material.

The possibility to join NiTi to dissimilar alloys is very appealing. NiTi alloys have an exceptional high bonding energy between nickel-titanium, resulting in low integrity with other elements at lower temperatures, and temperatures above 500-600 ºC induces titanium oxide consumption (migrating from its equiatomic ratio).

According to Miranda *et al.* [25] and their extensive study on the possible joining processes for SMAs, traditional fusion weld processes are not suited for joining these materials due to their strong dependency on an equiatomic ratio, resulting in the formation of brittle

intermetallic that lead to cracking and lose of SMA functional properties. The increased affinity of Ti with elements such as oxygen, nitrogen and hydrogen and precipitation of Ti_2Ni and $TiNi_3$ from high temperatures are major factors of embrittlement and strength degradation. Nitinol™ welding is very sensitive since joints are commonly very brittle and can seriously alter, if not destroyed, the NiTi shape memory and superelastic properties. Solutions such as riveting, fastening or crimping have been advanced for joining NiTi alloys [25, 26].

2.3.   Manufacturing processes

It is commonly referred in literature that at least two manufacturing steps are necessary for the fabrication of a metal-matrix composite. An intermediate step, known as preform (for sheets, bulks or wires), are normally held together by a binder or glue for the main manufacturing phase [27]. Cornie *et al* [28] have reviewed the processing techniques of MMC and categorized the fabrication techniques in three main areas: Liquid state, solid state and in-situ (the third comprises the both liquid and solid state techniques).

Amongst the solid state joining techniques, diffusion bonding requires both pressure and heat for a certain time: The metallic plates and reinforcing material are laid up in a stack; followed by heat and pressure, metal flow through the layers encapsulating the fibers inside; this process requires a vacuum atmosphere to avoid oxidation of the metallic sheet. Deborah Chung [2] addresses a variation of diffusion bonding process where the reinforcing fibers were first coated with filling metal therefore the previous intercalated metallic foils are not required.

Powder metallurgy is based on applied pressure up to 75% increased density and, normally, followed by heating (sintering) or hot working (*e.g.* extrusion, forging or rolling) [29].

While the diffusion bonding has a smooth interlayer preform, the latter forms a chaotic mix of materials [6, 30]. Figure 2.11 shows a turbine blade from NASA made from several diffusion bonding, hot pressing and other processes, depicting the complexity of solid state multi-phased processes.

12
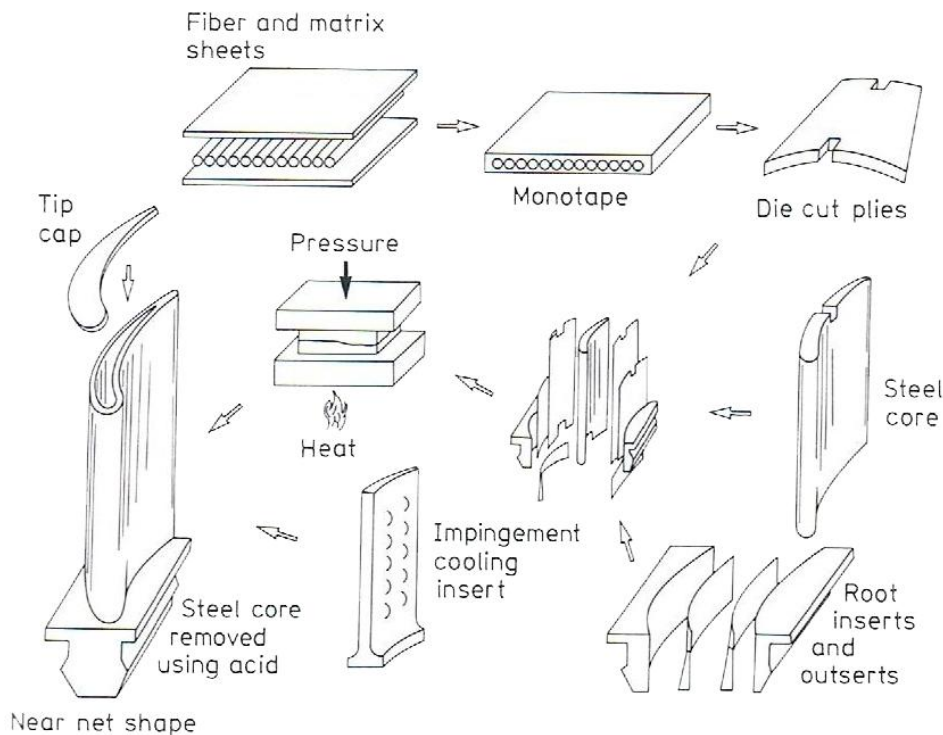
Figure 2.11 – Steps in a hollow air-cooled blade, made of tungsten fiber reinforced superalloy, fabrication process [1].

Hot pressing requires pressure, heat and exposing time. The main difference with the above stated diffusion bonding is the less pressure applied whilst higher temperatures are used. The higher temperatures degrade the reinforcements, therefore a third material (metallic foil with lower melting point) is applied to pre-form a consolidating bulk [2]. Friction stir welding belongs to the solid state category and will be discussed in section 2.4.

Liquid state fabrication methods are also particularly interesting for composite productions: Infiltration method, involves liquid metal under pressure to wet the reinforcing material and the pressure is provided by gas. The infiltration method is used to produce near-net shape composites. There is also a variant of this process that uses a piston (instead of gas) as the pressure source, known as squeeze casting [2]. Gas arc welding, laser beam welding, electron beam welding and brazing are also referred fusion techniques by Schwartz [5].

Plasma spray is another technique where matrix material is deposited, in vapor state, onto a substrate or reinforcing fiber composition [1]; Low-pressure plasma spray (LPPD) is a variation found to be much more versatile, often used to produce ceramic coatings onto metallic substrate materials [31]. It is known to be a process with high versatility, but barely produces a bonding interface and requires a post-consolidation process (similar to the above techniques). It consists of an inlet of powder mix into a plasma jet, the latter formed with an electric discharge

13

in a protecting gas mixture, the matrix material is melted into the high-velocity plasma jet and deposited to the target material.

There are a number of problems peculiar to MMCs: In the case of particulate reinforcements, the particles may have different densities from the matrix and this can lead to pronounced segregation effects. Undesirable chemical reactions may take place between the particle and the matrix, especially in fusion processes. The ductility disparities between matrix and reinforcements are triggers to crack initiation in the weldment, particularly in liquid-state joining processes [5].

Table 2.2 summarizes some of the most common techniques used in MMC production with metallic wires.

Table 2.2 – Metal matrix composite systems with metallic fibers [1].

Fibers	Matrix	Fabrication method	Field of application
Stainless steel	Al	Powder metallurgy, lamination	Aircraft industry
Be ribbons	Al, Ti	Al or Ti clad Be rods are inserted in drilled Al or Ti preforms; mechanical deformation of the preform	Shafts for high-speed rotating engines, *e.g.*, rotor shafts in helicopters and control rods in aircraft
Ta	Mg	Infiltration technique	Aircraft industry
Mo	Ti or Ti alloy	Powder metallurgy, fiber alignment by extrusion, rolling, etc.	Supersonic aircraft rocket propulsion
Be or Ti clad Be	Ti alloy, pure Ti	Explosive welding of interposed layers of Ti and Be fibers	Aircraft construction
Ni_3Al	Ni, (2-10%) Al	Powder metallurgy; the fiberlike phase is formed in situ during the mechanical working	Oxidation resistant, high strength at high and low temperatures
Ni-Cr-Al-Y	Ni alloy	Powder metallurgy	Sealing elements in turbines and compressors
W/1% ThO_2	Superalloy	Investment casting	Jet engines
W	W-Ni-Fe alloy	Liquid phase sintering; the W fibers are recrystallized to avoid dissolution	
Stainless steel	Ni alloys	Electroforming	Rocket engines
Mo, Ti, Nb	Ni superalloys	Powder metallurgy	
W	Cu	Melt impregnation	Electrical machinery
Nb filaments	Ni, Cu, Ag	Nb filaments embedded in a Cu, Ni, or Ag matrix are passed through a molten bath of Sn to form Nb_3Sn	Superconductors

14

2.4.   Friction stir welding

FSW is a solid-state joining technology, in which a rotating tool with a shoulder and a pin moves along the faying surfaces of two rigidly clamped plates, faying surfaces are the inner compressed sheet interfaces (due to the mechanical axial forces applied by the tool). FSW joint configurations typically used are the ones depicted in figure 2.12 [32, 33]. The shoulder makes a firm contact with the surface of the work-piece; the heat generated, by friction of the shoulder and pin surfaces, softens the material being welded. Severe plastic deformation (SPD) and flow of this plasticized material occurs as the tool is traversed along the welding direction. Material is transported from the front of the tool to the trailing edge where it is forged into a joint [34].
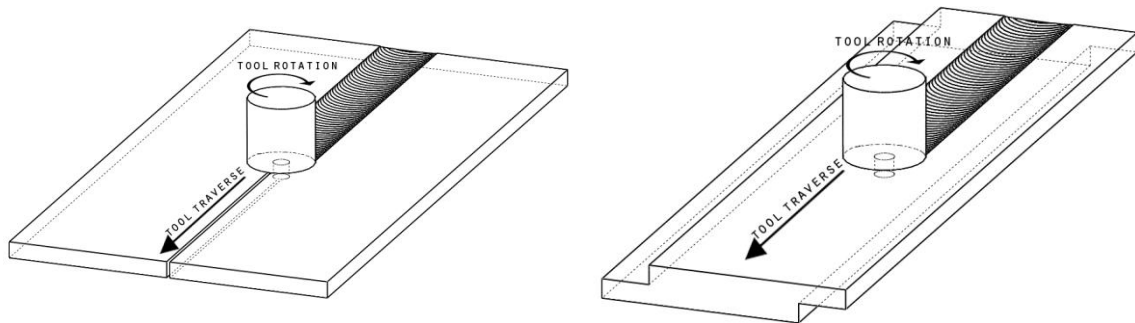
Figure 2.12 – Illustration of butt (left) and lap (right) joint configurations: tool traverse and rotation movements depicted above.

The side where the speed of rotation is the same as that of traverse speed of the tool is called the advancing side (AS), with the opposite designated as retreating side (RS). The former is characterized by the positive vectorial sum of the tool feed rate and of the peripheral tool velocity; whereas in the latter the two velocity vectors are opposite. This difference can lead to an asymmetry in heat transfer and material flow. Since, a vertical movement of the material flow is desired, special tools have been designed to amplify this flow [35].

The mixture of the material at a given temperature reorganizes the grain microstructure and the pressure applied on the welded zone forges the material with a good dimensional stability and low distortion of the processed zone [36]. Four distinct zones can be identified in figure 2.13, a FSW or friction stir processed bead exhibits different microstructural features in volume, thus mechanical properties.
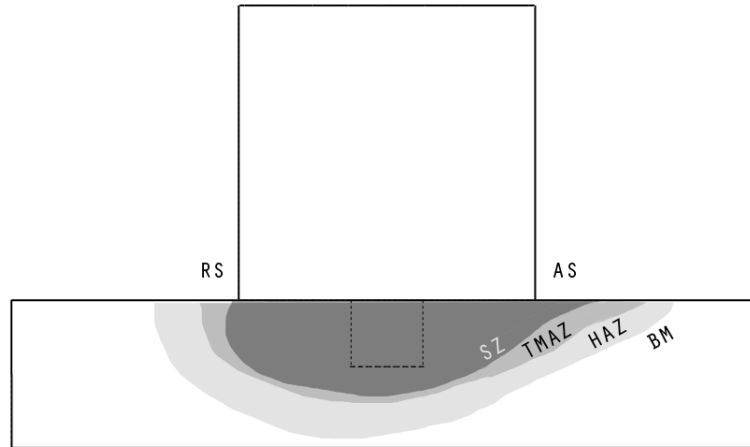
Figure 2.13 – Illustration of the four main zones in a transversal section of a friction stir welded bead. SZ – stirred zone, TMAZ – thermo-mechanically affected zone, HAZ – heat-affected zone, BM – base material, AS – advancing side, RS – retreating side.

The stirred zone (or nugget) presents a severe plastic deformation and high temperatures, enabling dynamic recrystallization and producing an equiaxial grain structure. The asymmetric geometry of the nugget between the advancing (AS) and the retreating side (RS) results from unequal strain rates, creating a typical tail on the advancing side. Therefore, the advancing side has a higher plastic deformation and a reduced grain size. Reynolds [37] reported that the nugget zone was slightly larger than the pin diameter and as the pin diameter increases the nugget geometry acquired a more rounded shape, with a maximum diameter in the middle of the nugget. Mishra *et al.* [34] related the decreasing of recrystallized grain size with decreasing annealing temperature of the base material.

Thermo-mechanically affected zone (TMAZ) also experience high temperature and deformation during FSW, although deformation strain is insufficient to promote recrystallization and thus to develop a new crystal structure. TMAZ is characterized by an upward grain elongation, due to the stirred zone boundary. Thermal cycle experienced by TMAZ induces precipitate coarsening and dissolution.

The heat-affected zone (HAZ), is the least affected zone by FSW and is characterized by experiencing a thermal cycle but no plastic deformation.

Figure 2.14 depicts the contribution of processing parameters when the objective is to control heat generation and material flow around a non-consumable tool. The sum of rotational and traverse speed result in two asymmetrical vectors of velocity, in literature is very common to study the relation between them, sometimes referred as (ω/v) ratio, heat index or pitch. Process pitch is the distance travelled by the tool along the welding direction in a single revolution.
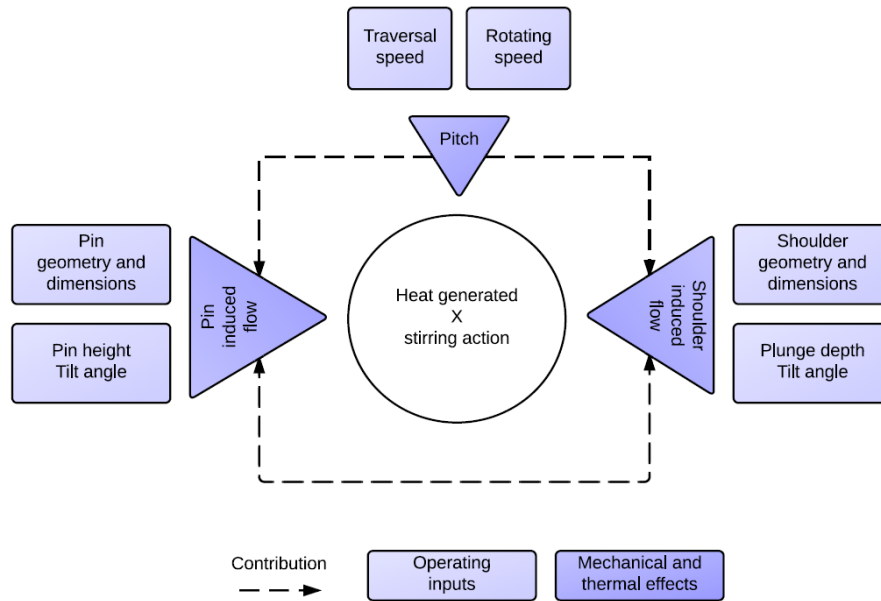
Figure 2.14 – Diagram of FSP operating parameters.

Tool features induce the material flow around pin and shoulder. The mechanisms of material flow suggest that (a) surface friction between tool and material at the leading edge softens the base plate and initiates a plasticization swirl around the tool, (b) after the complete plasticization of the material, the heat is generated by the severe plastic deformation of the material whilst the friction of the shoulder, and to a lesser extent the pin, is negligible. It is the correct control of (a) and (b) that avoids common issues like excessive heat generation and stirring in welds [38]. It is fairly easy to realize that tool rotation vector has not only a great impact on the stirring action but also on the heat generated.

Known as the angle between the shoulder axis and the workpiece figure 2.15 a), the tilt angle (TA) enables a correct flow of material from the front to the trail of the tool. Higher TA results in a more dispersed softened material, the opposite in an inefficient material flow. It has been pointed as one of the least significant parameters [39-41].

Plunge depth (PD) parameter is also illustrated in figure 2.15 a). Although PD and pin height might seem redundant (both parameters level the lowest tool point depth), modifying the PD does not increase/decreased the length of the pin in relation to the shoulder, therefore the pin induced flow pattern should maintain constant. The figure 2.15 b) shows PD increment along the weld bead, there is a clear relation of surface finishing and appearance with the higher PD, increasing PD results in higher heat input, material consolidation and plasticized material. Low PD results in brittle fracture and poor surface appearance due to insufficient heat input to soften the material. The opposite, ever-increasing tool PD or axial pressure generates excessive heat input, forming defect sites and shear lips in both AS and RS. It is also responsible for the tool sticking with the matrix.

Tool geometry is one key parameter for proper FSW runs. Tool design affects weld properties, defects and stress on the equipment – several tool geometries have been patented, especially for FSW, although they are currently designed empirically by trial and error [42, 43].

Important factors are shoulder diameter, shoulder surface angle, pin geometry, including its shape and size, and tool material nature. Shoulder generates the most heat, therefore its diameter is important, and its sticking action on the plasticized materials largely establishes the material flow field. The torque delivered by the tool has been studied to better understand the mechanics that affect the sticking of the tool interface. With increased temperature, flow stresses of the bead decreases and stirred area increases with the shoulder diameter. The product of these opposing factors leads to a maximum grip of the shoulder on the volume stirred [42].
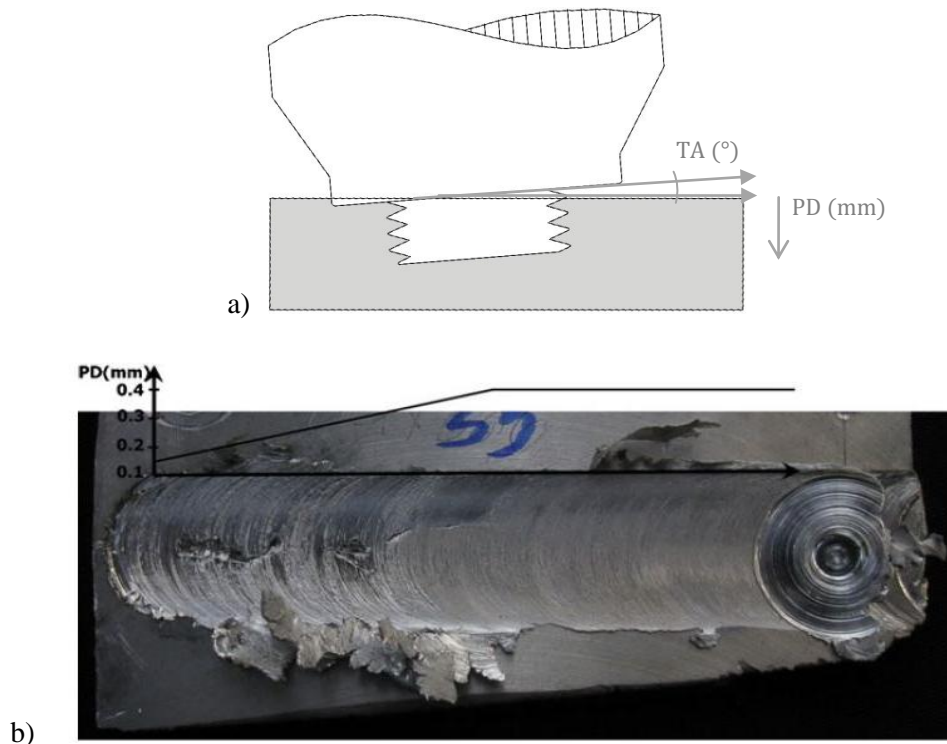
Figure 2.15 – Plunge depth – PD (FSP parameter); a) Schematic illustration of PD, b) Effect of the PD variations from 0.15 mm to 0.4 mm in the right, rotational and traverse speeds were 900 rev/min and 63 mm/min, respectively [39].

A set of different surface shoulder patterns have been developed to enhance the material flow around the tool. Hirasawa *et al.* [44] studied flat, concave and convex tool shoulders, and cylindrical, tapered, inverse tapered and triangular pin geometries. Microstructure, geometry and failure threshold of a weld may be significantly altered if the tool

shoulder chosen is concave rather than flat. On the other hand, pin threads on the surface influence the axial force of the tool on the processed plate and pin induced flow [45]. Fuji *et al.* [46] studied various tool shapes in FSW butt welds, for softer aluminium alloys a columnar tool pin without any thread would produce defect free welds – they also suggested that for less formable alloys, a triangular prism shaped tool pin would be more suitable. Zhao *et al.*[47] used columnar and tapered pins, both with and without threads. They observed that tapered threaded pins produced welds with the minimum defects in 2014 aluminium alloys.

Another technique used to reduce the rapid tool wear of FSW joining of dissimilar materials is to plunge the tool in the softer material while avoiding contact of the tool and the harder material. This technique is setting the pace especially on lap joint FSW technique.

Softer aluminium alloys are especially interesting for reducing tool wear while increasing joint efficiency using this solid-state process. Aluminium alloys are by far the most widely used in metal–matrix because of its low density, low melting temperature (adequate for composite fabrication and joining), low cost and good machinability. Main applications include structures, heat sinks, substrates [2] and, recently, electric-conduction alongside with copper [48]. FSW of some aluminium alloys is especially interesting due to its difficulty in joining with fusion processes [40, 41, 49, 50]. Also, 5xxx alloys shows great improvement with heat generated in FSW, often above the dissolution temperature of precipitates, allowing reprecipitation, overaging and other tempering processes to occur [51]. AA 7xxx hard alloy series often suffers from brittle fracture, the implementation of FSW enhances the alloy ductile and stress-strain response [52].

On the other hand, commercially pure aluminium alloys (with more than 99% purity) have shown very little interest. Manisha *et al.* [12] developed new surface processing techniques (by FSP) for Al100 alloys, although with no further researches on this subject from 2007 onwards. Kurt *et al.* [53] also developed new ceramic coatings in pure aluminium matrices, more than doubling hardness with a SiC powder coating, although aluminium ease of formability and/or the heterogeneity of the material promptly created large amounts of flash, inconsistent weld beads and so on. Elrefaey *et al.* [54] pointed out several inner morphology defects in the welded zones, probably caused by slight pin depth differences along the weld bead. The overall research developed sound welds, with often occurrences of very underperforming joints. Few dissimilar material joints with unalloyed high purity aluminium have been also reported.

AA1xxx aluminium alloy series are characterized by good electrical and thermal conductivities and corrosion resistance, with poor mechanical properties and high workability. In fact, standard for the electrical conductivity of materials in international annealed copper

standard (IACS) ranks this high grade aluminium series as the best wrought aluminium alloy with 62 % of electrical conductivity, compared to the normalized value for annealed copper wire [55].

Cold worked pure aluminium has increased strength, but it does not support heat-treatments. Chemical equipment, heat exchangers, electrical conductors and capacitors, decorative trim are a short-list of possible applications [11].

Threadgill *et al.* [51] exhaustive review on Friction Stir Welding is solely focused on aluminium alloys. According to author's summary, a few interesting points on the use of this process can be listed:

(i)   the absence of fusion state roughly reduces distortion of the welded beads, due to the non-existing thermal contractions associated with solidification and cooling;

(ii)   highly flexible process, applicable in butt, lap or spot welding geometries in any dimension;

(iii)   high welding rates. FSW con produce single-lap welds in thick materials, whereas other processes require multiple passes.

Due to the asymmetrical phenomena of FSW, the advancing side of the welded lap joints are often related to a pull effect, while the opposite, retreating side, pushes the material (interface). The pull effect resulted one of the most common defect in lap joints, figure 2.16, described as hooking and it occurs mainly on the AS, it is characterized by an upward rotation of the unwelded interface up to 90º [56]. On the opposite side, the RS experiences a plate thinning on the unwelded region, the sum of the shoulder induced flow and the pin induced (in volume) flow results in a pronounced bump of the base plate and a thickness reduction on the former plate. This can severely compromise the joint mechanical properties and integrity.

Advancing side   Retreating side
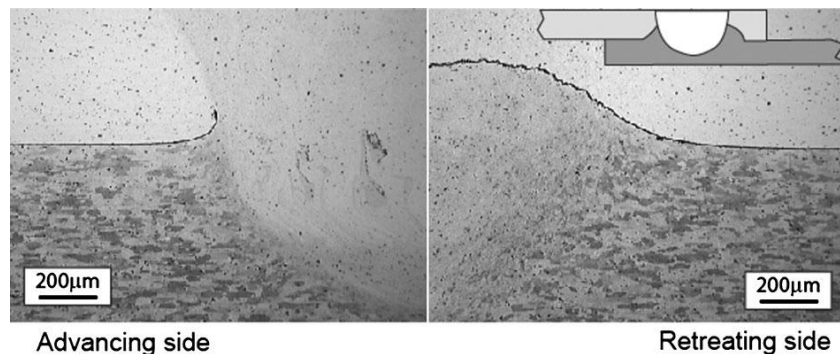
Figure 2.16 – Lap weld defects showing hooking on advancing side and plate thinning on retreating side in lap welds between AA 7075 (upper) and AA 2024 (lower) alloys [51].

20

Percentage effective thickness (PET) is a term to quantify this thickness reduction, and is defined by equation 2.1 [56]. Figure 2.17 illustrates hooking and thinning after FSW, t_e is measured from the Advancing hooking side.

$$PET = \frac{t_e}{t_0} \times 100 \qquad (2.1)$$
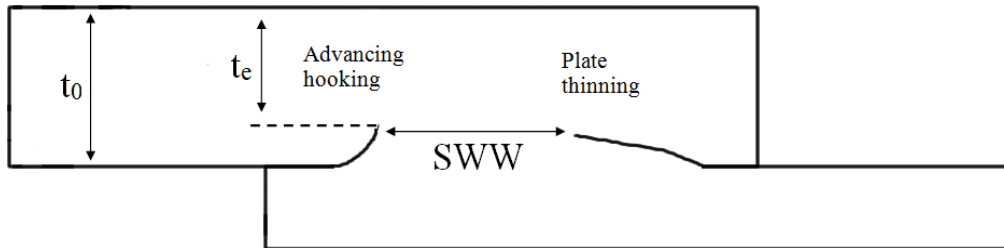
Figure 2.17 – Illustration of hooking and thinning effects after FSW, t_e and t_o indicators for the percentage effective thickness measurement.

There is a consensus that tool rotation speed (ω) is the major factor affecting the joint strength. Excessive rotation results in larger hooking size, lowering the joint strength [41, 54, 56-62]. A slight variation in this parameter may result in very dissimilar joint strengths. The pitch was lately found to be more relevant than the rotational speed [41]. With the same purpose, Yazdanian [56] studies the impact of this relation on the quality of the deformed faying surfaces. This was reported not to be a good indicator (two welding cross sections with the same pitch can be found in figure 2.18) same pitch but different set of rotation and traverse speed produced very dissimilar weldings. Nevertheless, with a fixed pitch, increasing the tool rotation augmented both the horizontal and the vertical material flow during FSW.
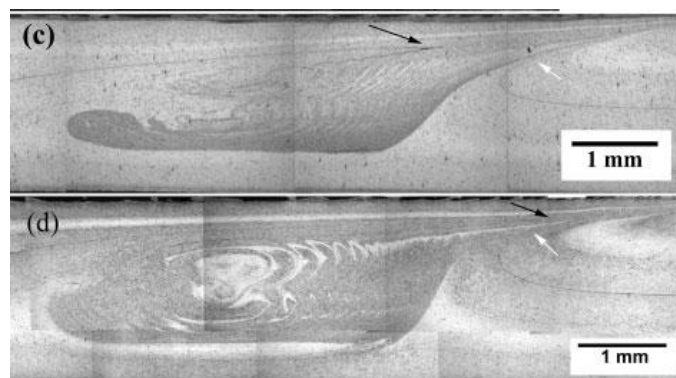
Figure 2.18 – Tranversal sections of welded lap joints with equal pitch values (0.127 mm.rev[-1]). Modified from [41]

Yazdanian reported the dependency of percentage effective thickness value on the HI. Lower HI resulted in higher PET, consequently deformed less material in the interface. High HI increased the pin induced material flow volume thus contributing significantly to the upward rotation of the original interface (hooking).

The tangential velocity of the material flow around the pin has to high enough for the material to refill the void created due to the tool movement. To achieve maximum lap shear strength, the rotational speed must hold at the lower end of possible range. Soudararajan *et al.* [57] shows that the void free weld formation takes place under a range of welding parameters for both the similar and dissimilar aluminium sheets joining.

On the impact of the pin height (PH) and plunge depth (PD), Elrefaey *et al.* [54] studied different pin depths in Al-Steel lap jointed alloys. With 2.0 mm of PH (tangent to the steel base plate), the joints exhibited very low strength; most of them failed during the preparation of specimens. Furthermore, a slight increase in pin depth (0.1 mm) had a significant effect on the performance of the lap joints. Several authors reported similar results for the pin height, Yadava *et al.* [41] achieved a maximum lap shear strength FSW with a pin of the same height as the sheet thickness. Although, Cederqvist *et al*. [60] showed that a shorter pin result in less pull-up on the retreating side of the weld. According to Yadava, PET values on AS and RS increased with increasing PD, this latter conclusion may validate the former.

A PD of 10%−20% more than the pin height would diminish hooking size in the AS, while for RS a smaller value of the PD would attenuate plate thinning, giving a higher effective thickness. An increase in pin height of the FSW tool in lap welding increases the pin penetration across the faying surface, alloying a more effective oxide disruption [41].

Such PD precision, in the tenths of millimeter, requires an accurate control of the plunge depth of the tool. It was found from previous study [57] that weld flash increases as the plunge depth increases and the weld crack occurs on the surface for plunge depth greater than 0.5 mm. Also, if contact between the shoulder and workpiece is lost during the weld formation, a crack develops. The plunge depth should be fixed when the process parameters are bounded within an upper and a lower limit.

Research made on pin diameter shows that FSW runs on 3mm thick sheet had improved lap joints for 4 mm pin diameter, while 6 and 7 mm resulted in void formation, excessive shear lip and incomplete joints. An optimum pin diameter of 5 mm attained the maximum shear strength [40]. Kulecki *et al.* [63] extended to the former conclusions, reporting that an optimized fatigue strength weld is a correspondence between tool pin diameter, rotation and traverse speed. Ericsson *et al.* [61] obtained an improvement of fatigue fracture obtained

with a broader tool shoulder and a concave pin end. Also, found lower fatigue thresholds for lap joints, against butt joint geometry.

Leal *et al.* [38] researched on the impact of the axial force during FSW. With the increasing in the axial force, with the remnant parameters fixed, defects appear in the surface only in the beginning (5xxx series annealed Al alloy). More, increase of the axial force was also responsible for a decreased of 15 % in the hardness of welded material.

Fersini *et al.* [64] tested for fatigue Al 2024 lap jointed alloys, reporting that failure occurred through the weld on the AS of the top sheet (Hooking side), and all of the specimens have ruptured this way – several reports conclude the latter [38, 65].

The possibility to eliminate the critical AS defect was proposed by Ericsson [62]. In this study, double pass welding have shown to increase joint efficiencies of lap welds substantially. Reason for this are the increased interface weld with, enhanced oxide disruption, and the hooking reduction, or elimination. Cederqvist *et al.* [60] showed that a double pass weld can provide higher joint efficiency (shear strengthened until failure), with strengths comparable to those of butt joints and higher than riveted joints – their results reveal the existence of a critical interface between the faying sheets, suggesting that a higher weld nugget would lower the secondary bending on overlapping, therefore a tool with a wider pin is beneficial in the case of overlap joints.

2.5.   Conclusions

This chapter introduced a technological background of the subjects investigated in this work. A thorough research on the most advanced processes and methodologies is presented. Composite materials proved to be beneficial for an extensive range of applications since they can combine the strengths of involved materials. Development of technologically different joining methods is crucial for material engineering. Solid state techniques have pushed forward on new welding possibilities and properties. FSW is amongst these, the capability to join materials bellow fusion point is of great advantage for critical alloys, such as aluminium and NiTi.

Scarcely addressed, lap joint FSW of AA 1100 aluminium alloys must be thoroughly characterized and documented; also, the development of reinforced aluminium-matrices with wires or ribbons by FSW has not been documented. Limited and unsuccessful work is reported on the manufacturing of composites involving NiTi alloys. Thus, this work aims to address this problem.

3.   EXPERIMENTAL PROCEDURE

3.1.   Materials

AA 1100 aluminium alloy sheets were used as substrate. The following tables 3.1 and 3.2 display the chemical composition, mechanical and physical properties for this alloy.

Table 3.1 – Chemical (wt.%) and mechanical properties of AA 1100 [11].

Element	Al	Si + Fe	Cu	Mn	Zn	Other
Max	-	1.00	0.20	0.05	0.10	0.15
Min	99.00	-	0.05	-	-	-

Temper	UTS (MPa)	Yield strength (MPa)	Elongation at break (%)	Hardness (HB)
O	90	34	35	23
as-received AA 1100	56	35	33	-

Table 3.2 – Physical properties of AA 1100 [11, 66].

Alloy	Density (g/cm^3)	Coefficient of thermal expansion ($\mu m/m \cdot K$)	Thermal properties			Electrical properties	
			Thermal conductivity (W/ m·K)	Annealing temperature (ºC)	Melting point (ºC)	Electrical condutivity (% IACS)	Electrical resistivity (nΩ·m)
1100	2.7	23.6	218 to 222	343	646	57 to 64	59

The as-received sheets were guillotined, from the original 1.6 mm thick plate into rectangular samples, of 50x200, 100x100 and 50x100 mm.

NiTi ribbons of 0.9 x 2.8 mm were used as reinforcements, these are: Type N alloys, with a superelastic phase change austenitic finish temperature of -15 ºC. Ribbons were sectioned in 200 mm length samples. Table 3.3 summarises commercial information NiTi.

Table 3.3 – NiTi alloy specifications [11].

Chemical composition (at.%)		
Element	Ni	Ti
Max	51	52
Min	49	48

Mechanical Properties			
	UTS (MPa)	Yield strength (MPa)	Elongation at break (%)	E (GPa)
Austenite	895	195 to 690	15.5	83
Martensite	895	70 to 140	15.5	28 to 41

Physical properties

Thermal properties			
	Density (g/cm^3)	Thermal conductivity (W/ m·K)	Melting point (ºC)	Electrical resistivity (nΩ·m)
Austenite	6.45	18.0	1300	100000
Martensite	6.45	8.5	–	70000

The NiTi ribbons presented an oxidized surface and no superelastic plateau, therefore the as-received material was subjected to a heat treatment prior to composite production (the tensile testing results of the as-received NiTi alloy are further discussed in section 4.1). After heat treating at 500 ºC for 20 minutes, the NiTi ribbons austenitic phase changed to a martensitic phase, at ambient temperature, therefore altering its microstructure. Figure 3.1 shows the stress-strain response curve, a martensitic reorientation plateau is depicted. The reheated ribbons depicted an overall UTS reduction from the initial 1096 to 924 MPa together with an elongation at break increment of 211 %.
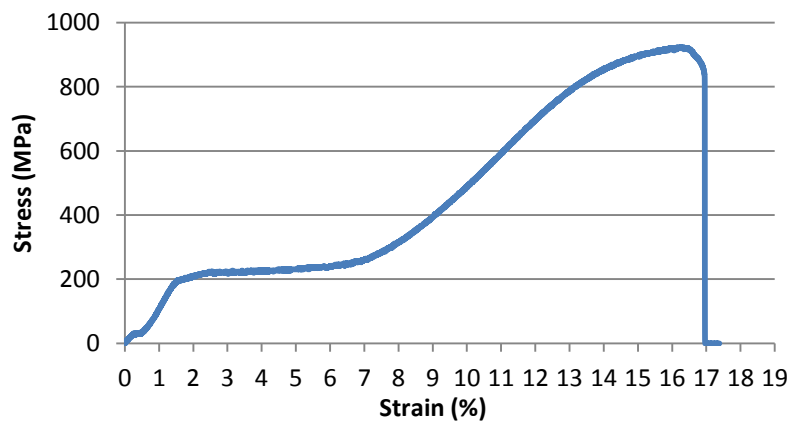
Figure 3.1 – Stress-strain curve of NiTi after heat treatment at 500 ºC for 20 minutes.

Steel wires of 0.8 and 1.0 mm diameter were used to study the effect of processing parameters on the processed depth, homogeneity of weld bead, among others. Those have remarkable low price when compared to NiTi and allowed to test the effect of sample configuration and positioning method on the bonding mechanism.

For this, a low alloyed steel wire was used with the mechanical properties shown in table 3.4

Table 3.4 – Mechanical properties of steel wire (AristoRod™ 12.5) [67].

UTS (MPa)	Yield strength (MPa)	Elongation (%)
560	470	26

3.2.   Equipment

In order to produce MMCs with embedded wires, a two stage joining process was implemented: First, the preform of the aluminium alloy base plate was produced with three different methods (to test and devise a proper groove opening technique); secondly, reinforcements were positioned into the base plates in a lap joint configuration and Friction Stir Welded.

Pre-processing comprised three different techniques: (a) A scriber, made from hardened and tempered tool steel; (b) a milling machine equipped with a HSS 10 mm diameter two flute end mill, the milling head supports an angle variation (the normal to worktable rotating axis admit a parallel position to the worktable, from -90º to +90º), and the groove opening required a 45º angle working condition; (c) a 100 ton manual hydraulic press machine equipped with specially designed steel plates, to endure the pressing conditions while forming the AA 1100 aluminium alloy to their correct shapes.

For the aluminium composites production, an ESAB machine with three degrees of freedom, LEGIO™ 3UT model, for Friction Stir Welding was used.

Figure 3.2 the FSW ESAB machine, X and Y-axis outputs 200 cm/min processing velocities, and up to 1000 cm/min [68]. The Z-axis is controlled by a hydraulic cylinder with a closed loop system. The FSW prompts an accurate guidance of the vertical tool movement, by either force control or position control. This is a hierarchy control method, that is, if position control is adopted, the force will be leveled to maintain the required position and *vice versa*. Although it is more advantageous to use the force control to ensure a more stable process along the weld length, position control must be set for the initial tool plunge depth.
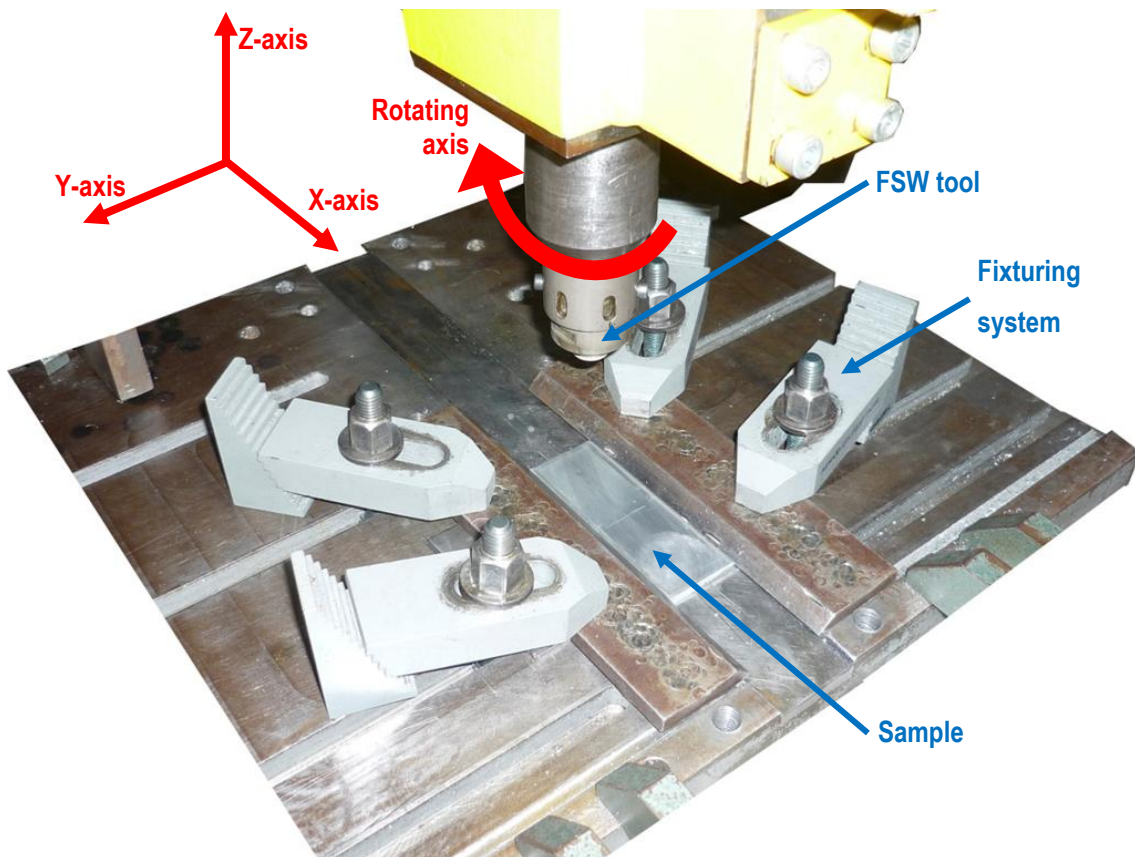
Figure 3.2 – Sample set up and degrees of freedom in FSW machine.

The worktable and the machine frame are fixed, as shown above, while the human machine interface (HMI) console, the power unit and the welding head move along the X and Y-axis. An internal water refrigeration system passes through the machine's spindle shaft up to the welding tool upper interface. Tilt angle (TA) can be changed by a set of screws. The tilt angle has a limit of 5º in a single direction. The HMI panel controls every other variable, apart from the TA.

A set of parameters can be manipulated during operation, or pre-set and saved for automation purposes, and these are:

- Traversal velocity (cm/min)

- Rotational velocity (rev/min)

- Tool force (Kg)

- Plunge depth (mm) and speed (mm/s), normally negative because is downwards

- Dwell time (s)

- Control method (force or position control)

FSW Tool

A special tool, developed and patented by Santos and Vilaça, at IST-UTL, was used [69]. Figure 3.3 shows a tool for welding processes, compact and modular disposable, allowing different combinations of geometric parameters between shoulder (1) and pin (2). It supports the FSW machine water cooling system (3) with an inner chamber close to the upper pin interface. It can be adjustable to different thickness of weld plates by changing the pin height. The system is composed of a body tool (4), a built-in shoulder (1), an adjustable pin (2), screws fixing the shoulder (5), and a threaded stud fixing pin (6). Machine spindle shaft and fixturing system are comprised by (7) and (8), respectively.
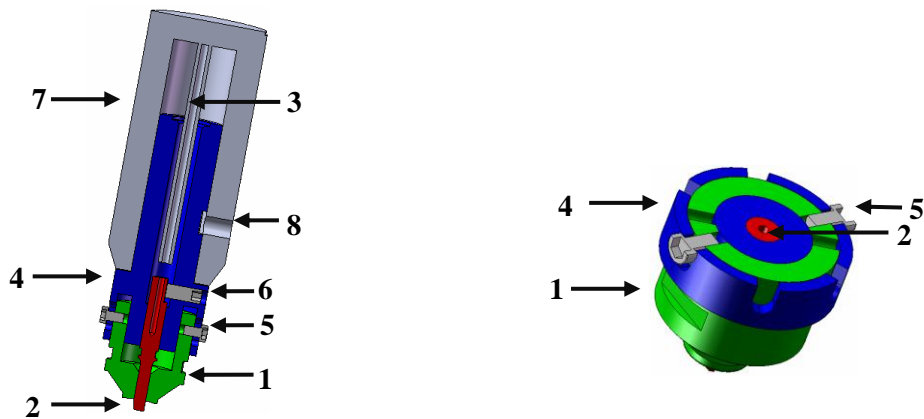
Figure 3.3 – Patented modular tool, (a) section view of the entire piece, (b) section view of the pin and shoulder [70].

The adjustment of the pin height (2) is made by screwing or unscrewing the shoulder from the tool body. The tool body material is DIN Ck45 steel, shoulder and pin are in AISI H13 tool steel. Figure 3.4 shows the FSW tool used in this investigation. The pin was easily adjustable to the required depth since the tool has a modular design.

Figure 3.4 – FSW used tool, 18 mm diameter plain shoulder with one two-lap ridge, and a 5 mm diameter threaded cylindrical pin.

The amount of force transferred to the welded material and worktable from the FSW equipment requires a suitable fixturing system. Torque generated during FSW induces high shear strength around the tool pin that, if not strongly constrained, would spin the welded plates around the tool. On the other hand, excessive aperture forces on the base plates may sometimes cause unwanted bulges, a set of plates have been designed to even the distributed the aperture pressure along the material. The clamping system, used mainly in multi lap FSW was mounted on the worktable support blocks to adjust height as presented in figure 3.5.
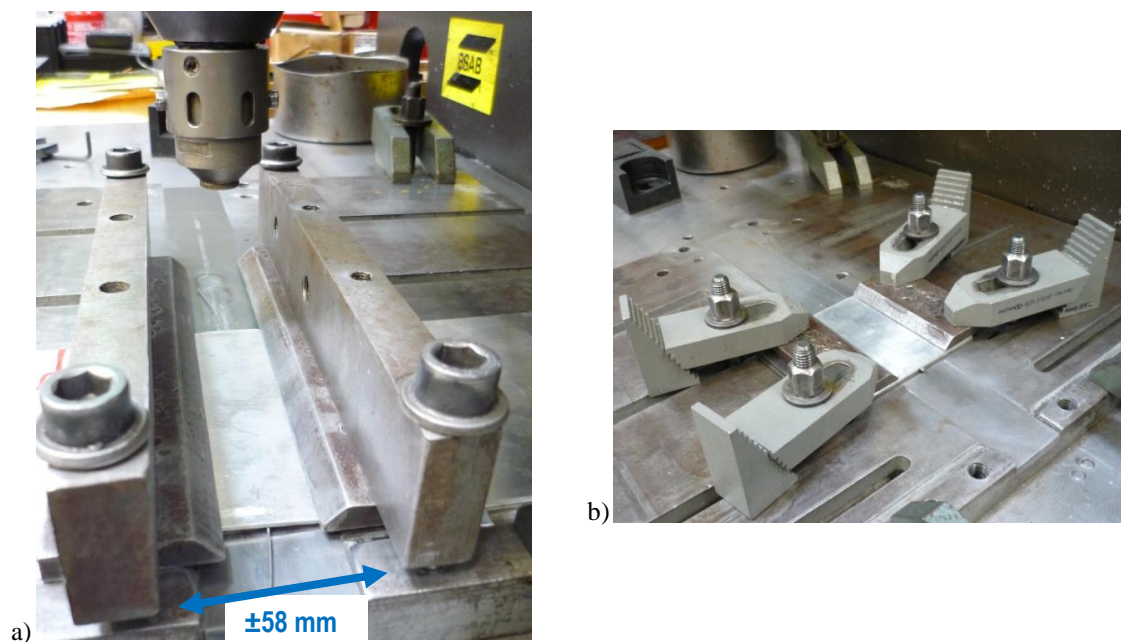
Figure 3.5 – Fixturing equipment, a) group of plates with a maximum of aperture, b) clamping system on worktable of the FSW equipment.

3.3. Working methodology

3.3.1. Sample preparation

Aluminium plates were mechanically worked for opening the groove, grinded, cleaned with alcohol and mounted in the FSW worktable. Three different methods were used for opening the groove. Figure 3.6 illustrates the groove geometries used.
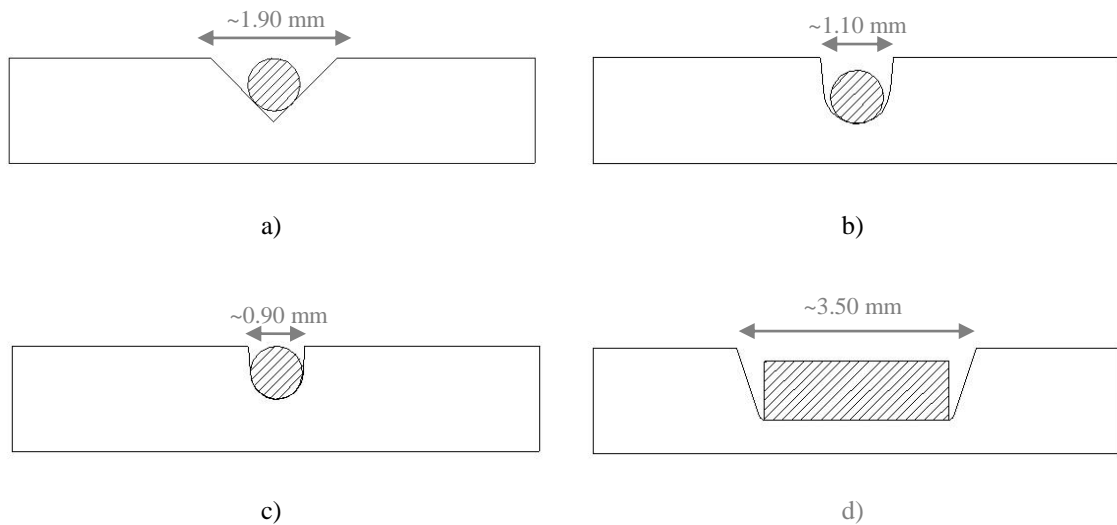
Figure 3.6 – Cross sections of base plate with metallic reinforcements before FSW. a) "V" type cross section shape groove, b) round cross section shape, opened with a 1,0 mm diameter steel wire, c) round cross section shape, opened with a 0,8 mm diameter steel wire, d) rectangular 1,1 x 3,5 mm cross section.

(a) A scriber was firmly pressed along the length of the specimen; the straightedge of the groove line was maintained with the help of a metallic set square. The groove section is defined by a "V" type geometry.

(b) The milling machined specimens resulted also in a "v" shaped geometry, as shown in figure 3.6 a). The working parameters were: 12 cm/min and 600 rev/min for traversal and rotational speeds, respectively.

(c) The last groove opening technique used was the one adopted throughout the investigation. The 100 tons hydraulic press produced fine results at 25 ton axial force; figure 3.6 b), c) and d) illustrate the type of geometries produced with this technique. Two mild steel base plates were used in the hydraulic press. Those were first rectified, grinded (with 400 SiC waterproof abrasive grinding paper) and cleaned until no particles or bulges remained. To create the round and rectangular shaped grooves, onto the AA 1100 base plates, AristoRod™

12.50 (with 0.8 and 1 mm diameter) and DIN Ck45 steel rectangular shape steel ribbons were used, respectively.

After opening the grooves Al samples were grinded with SiC paper, cleaned with alcohol and dried. NiTi were chemically etched in a solution of 0,45 ml HNO_3, 0,45 ml H_2O and 0,10 ml HF to remove surface oxides.

3.3.2. FSW of aluminium lap joints without reinforcements

In order to produce reinforced lap welded joints, a first trial was prepared to assess the metallurgical aspects of FSW. Several parameters were varied as: pitch, PH, PD, weld position and control method (force or position control); keeping all the others constant as: TA, plunge speed, dwell time, shoulder and pin geometries. Table 3.5 presents the values of the fixed parameters. Annex D summarizes the operating procedures applied in this investigation.

Table 3.5 – Fixed FSW parameters.

Tilt angle (º)	Plunge speed (mm/s)	Dwell time (s)
0.5	0.1	4.0

Tilt angle was fixed with a minimum tool tilt, to provide a good material flow in the front of tool while not too much shoulder deformation at the trailing edge. The overall effect of the TA in the joint quality is almost insignificant, whilst the surface quality is largely dependent on the tool tilt, due to flash formation (excessive shoulder penetration) and brittle crack formation (lack of shoulder penetration).

Plunge speed and dwell time are FSW initial conditions, used to achieve a proper material softening before the traversal movement of the tool. Those parameters have been studied and optimized for butt welding FSW by Nascimento [71], a preliminary trial with the imported parameters ensured a good initial material softening, and so they were kept constant throughout the investigation.

Welded width of the faying surfaces was the first condition tested. A set of tests was designed as follows: (a) fix PD and study pitch until a sound surface is produced, (b) fix pitch and increase PD to modify sound weld width. The first trial tests were analysed on site – a visual analysis was performed until a sound weld bead was produced and, from thereafter, both traverse and rotational speeds were fixed. The second test group was planned according to Table 3.6. Although PD was augmented, PH was kept constant at 1.4 mm, resulting in a depth increase between FSW passes.

Table 3.6 – GROUP A – Influence of PD in FSW of lap joints.

N°	V (mm/min)	Ω (rev/min)	PD. (mm)
1	50	800	-1.40
2	50	800	-1.50
3	50	800	-1.60

The first test group (GROUP A) related plunge depth with weld width and deformation of the surfaces. Table 3.7 resumes the optimized FSW parameters, based on the preliminary visual inspection and metallographic analysis of the weld bead surface.

Table 3.7 – Optimized process parameters for multi-pass AA 1100 lap-joints.

α (°)	V (mm/min)	Ω (rev/min)	Plunge Speed (mm/s)	Dwell Time (s)
0.5	80	800	0.1	4.0

In order to have an accurate precision of the FSW tool plunge depth, this first sequence of FSW welds was conducted using tool position control. The example on figure 3.7 illustrates the stringency required for a 1.8 mm penetration depth lap-joint, 12.5 % of thickness penetration of the base plate. After understanding the output values of the applied pressure on FSW tool Z-axis, a second group of trials was conducted with tool force control. This resulted in more homogeneous weld beads.
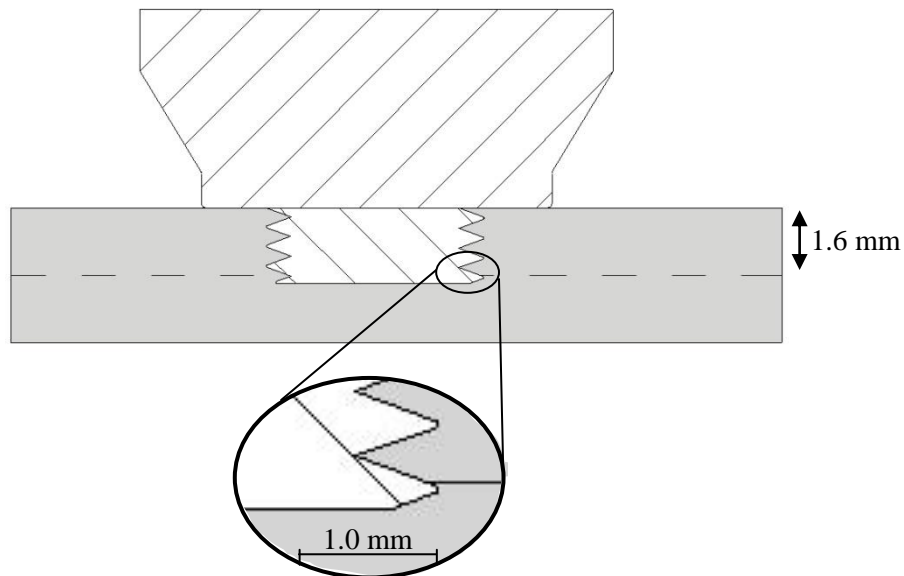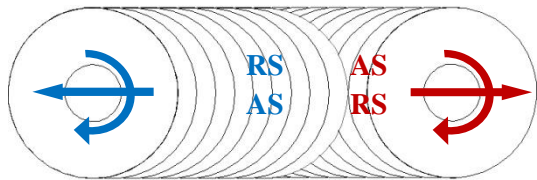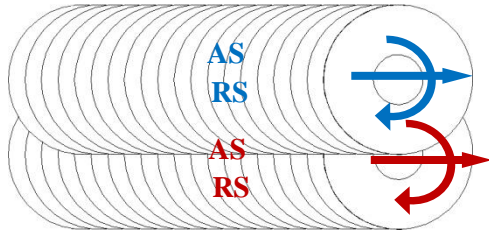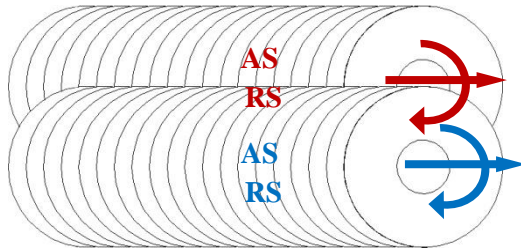
Figure 3.7 – FSW lap-joint with a threaded flat bottom 1.8 mm height pin.

The second group of tests (GROUP B) aimed to investigate different multi-pass conditions. Three overlapping methodologies were studied for weld bead surface conditions and faying surface joint defects. The asymmetric advancing and retreating sides of FSW enhance a dissimilar material structure transformation, resulting in different material properties on both AS and RS sides, table 3.8 shows the different overlapping techniques used.

Table 3.8 – GROUP B – Influence of overlapping mode in lap joint FSW.

Overlapping scheme	Description
	(1) Full overlap with inverted flow
	(2) Offset overlap by the advancing side (AS)
	(3) Offset overlap by the retreating side (RS)

Full overlap (1) fully covers previously friction stir welded bead width with a new inverted flow FSW, the AS and RS remain in opposite sides between the two passes. The offset overlap jointed materials have opposite AS and RS between passes, (2) one previously RS welded bead is superimposed by the AS of next FSW, or (3) the precedent friction stir welded AS is overlapped by the following FSW retreating side.

The offset dimension is previously calculated by the overlap ratio (OR), equation 3.1. Relating the amount of overlap between two successive passes, in multi-pass FSW/FSP [72]:

$$OR = 1 - \left[\frac{1}{d_{pin}} \right] \qquad\qquad (3.1)\ [72]$$

Where d_{pin} is the pin diameter and l is the minimum distance ratio between pin interfaces in two successive passes. Multi-pass with no gap between two consecutive pin positions represents the maximum OR value; the opposite, increasing distance between two different pin positions, decreases OR value. According to Gandra [73], a minimum OR of 50% leads to sound multi-pass welds. An OR of 80% was used.

3.3.3. FSW of aluminium lap joints with reinforcing materials

To study the feasibility of the material embedment into the aluminium sheets a similar approach to the one described in the first group of tests (GROUP A) was made. The reinforcements were deposited in the aluminium base plates facing the tool and a second aluminium sheet was placed on top. The overall set was securely fixed as discussed earlier in section 3.2. Different pitch relations were tested until a sound surface weld with a steady length of ribbon reinforcement was achieved. Table 3.7 shows the optimized values (after a visual inspection) for the reinforced lap joints.

To understand PH and PD influence on the shoulder induced flow, and the impact of this surface material flow in the quality of the surface weld bead, a surface characterization was performed and compared against a relation of PH and PD, as shown in table 3.9. Group C tests explore equal and different PH and PD parameters, later a visual characterization helped to better understand the influence of those. Since tool tilt produces a dissimilar contact at any instant along the weld bead, it was limited to a minimum possible to achieve a proper material inlet at the front of the tool.

Table 3.9 – GROUP C – Shoulder surface contact, the impact on surface weld beads.
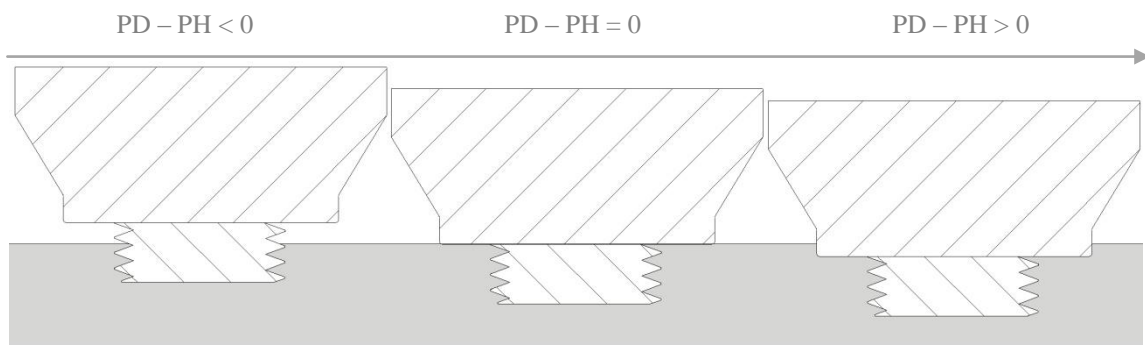
Accounting for pin distance to the faying surfaces, several pin heights and plunge depths were trialed. For pin heights close or greater than 1.6 mm, tool was offset from the center of the ribbon to a maximum distance of 1 mm, varying between trials. Table 3.10 shows schematic of the process and ribbon position relative to the FSW tool.

Table 3.10 also shows two lap joint methodologies used: one where a smaller pin height is on top of the wire reinforcement; the second image shows a tool offset from the center of the rectangular ribbons, with the pin in contact with the base plate.

Table 3.10 – GROUP D –Pin depths and offset values used in this investigation. Upper left figure illustrates a circular ribbon embedded in metal-matrix in lap-joint geometry with 1,4 mm PH FSW without offset. Downright setup with a rectangular ribbon, PH > 1,6 mm and less than 5 mm of tool pin offset.
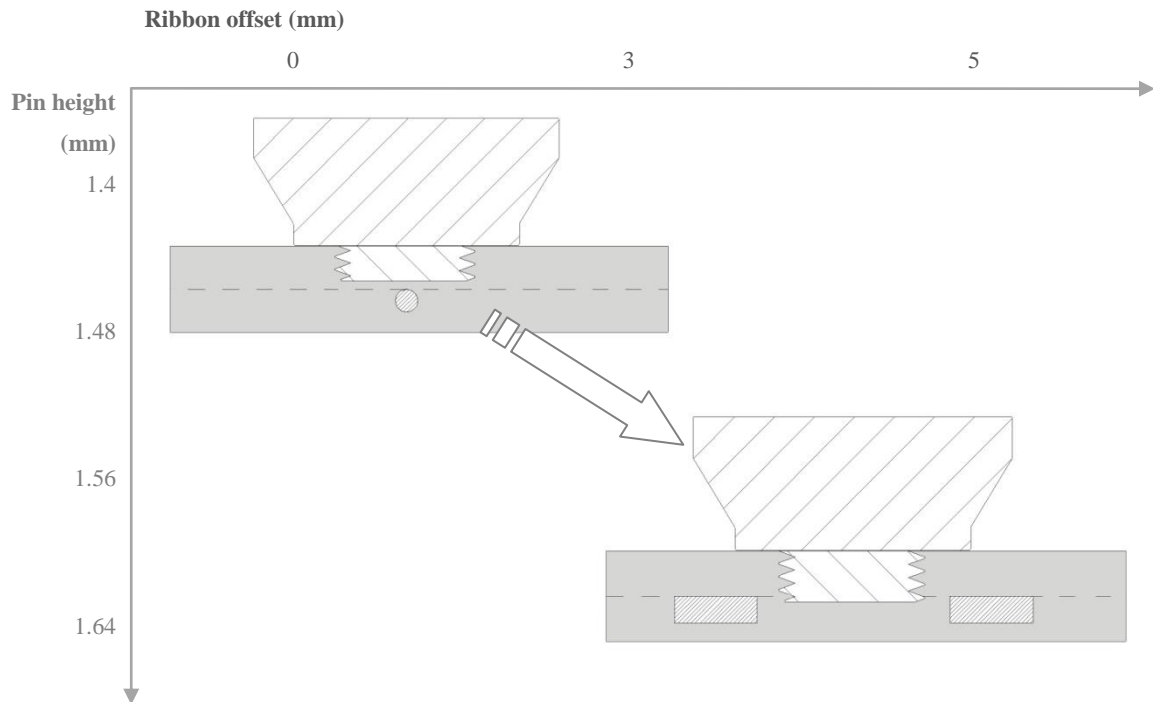
3.4.   Characterization methodology

The characterization of composites comprised:

- Visual and X-ray radiography inspection

- Metallography

- Mechanical testing

- Eddy current testing

36

3.4.1. Visual and X-ray radiography inspection

A visual analysis was implemented on site after each test to adjust processing parameters. Table 3.11 resumes some of the qualitative features used on visual analysis. To carry out morphological surface classification, specimens were photographed, X-rayed and catalogued.

Table 3.11– Qualitative features on visual inspection

Feature	Description
Excessive heating	Describes any noticeable spots of intense heating on the bottom of the FSW specimen.
Flash formation	Amount of flash generated.
Point defects	Singular defects on the welded bead with a void appearance.
Weld bead uniformity	Stability of the SZ along the traverse direction, noticeable spots of brittle crack fractures or cavities.
Reinforcement ribbon linearity	Same length of the ribbon tips before and after FSW.

The X-ray radiography analysis proved to be very effective, aluminium attenuation to X-ray is less evident then for the reinforcements, resulting in a very sharp and contrasted image where the position and the shape of reinforcements is easily depicted inside the aluminium-matrix. A Kodak 2100 X-ray radiography system equipped with a 60 kV high frequency generator was used. The exposing time varied between 0.125 and 0.500 s, from to 0.76 up to 3.05 mGy of absorbed energy.

3.4.2. Metallography

Materials metallographic analysis was performed under optical and scanning electron microscopes. Several sectioned materials from the original FSW specimens, base material, tested material (tensile and bending tests), were cold mounted with Epoxycure® epoxy resin and hardener, when necessary. Samples were grinded, polished, and etched to reveal grain boundaries and highlight different structural features. Annex E.1 describes samples preparation for metallography.

<u>Optical microscope (OM)</u>

Optical microscopy was performed using a Leica DMI 5000 M inverted optical microscope at CENIMAT/I3N. The microscope had a digital camera linked to a dedicated software. The program allowed to control the microscope and to compose images of a whole specimen, with a good resolution, compared to regular optical microscopes without composition features.

<u>Scanning electron microscope and energy dispersive X-ray spectroscopy</u>

Scanning electron microscope (SEM) equiped with energy dispersive X-ray spectroscopy (EDS) was used for surface analysis of produced and tested samples, performed at CENIMAT/I3N. The use of SEM has obvious advantages: the great depth of focus in comparison with optical microscope at comparatively low magnification; the possibility to observe complex shape and material features, such as tensile and bending test surface fractures; the use of diffracted X-rays qualitative elemental analysis [74].

SEM analysis was performed with secondary electrons (SE) and backscattering electrons (BSE).

3.4.3. Mechanical Testing

In order to assess mechanical properties, several tests were performed and these were tensile, bending and vibration.

<u>Tensile test</u>

Tensile samples were machined, from the bulk and the final reinforced material, and later rectified with a Sunlike MSSG-2550AH surface grinding machine equipped with light abrasive wheel. The grinding ensured the dimensional tolerance requirements and eliminated stress concentration points. Tensile tests were performed using an Instron 3369 electromechanical with a cell load of 50 kN with an upward vertical movement of 5 mm/min.

Aluminium base material was tested according to EN 10002-1 (2001) [75], specimens were 12.5x3x100 mm, width, thickness and length, respectively.

Aluminium-material composites were sectioned and machined from the original specimens and tensile tested to failure. Sets of three equal specimens were sectioned, machined and grinded (400 water grinding paper) to eliminate stress concentration points due to surface

roughness. Figure 3.8 illustrates the trial setup. Additional information on tensile test procedures is presented in annex E.2.

25

25

R5

100
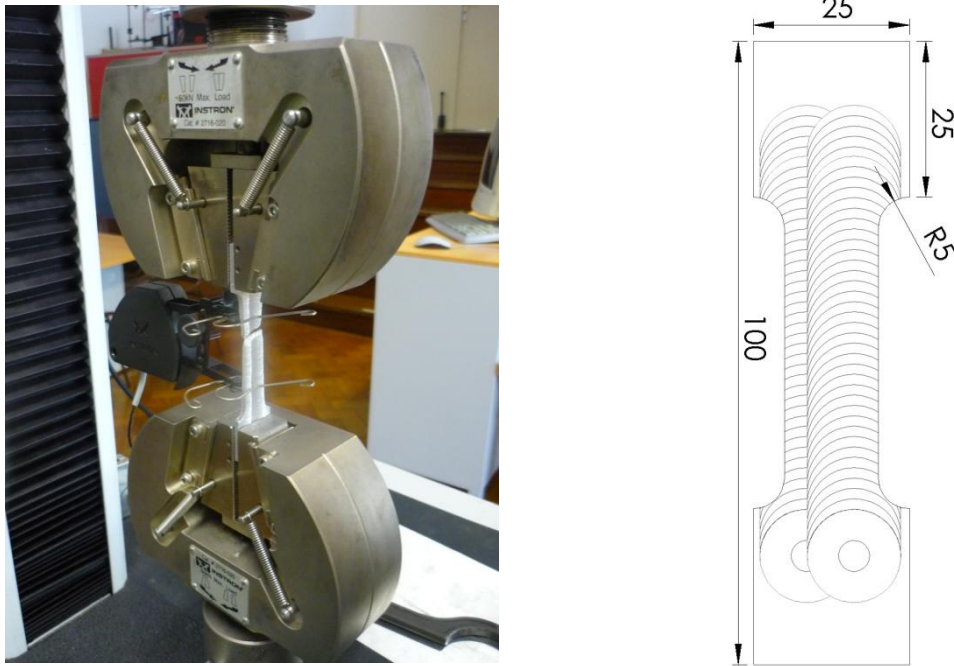
Figure 3.8 – Tensile runs set-up and composite test samples dimensions.

<u>Bending test</u>

Three-point bending tests were conducted, according to EN 910 (1996) [76], to investigate the stress-strain response of the composites. Sets of three equal specimens were sectioned, machined and grinded (400 water grinding paper) to eliminate stress concentration points due to surface roughness and 'sharp edges'. Sample dimensions and setup are presented in figure 3.9. The ribbon reinforcements were placed longitudinally, as figure 3.9 shows.

Bending tests were performed using an Instron 3369 electromechanical machine with a load cell of 50 kN with a downward vertical movement of 5 mm/min and a span of 100 mm between the two lower supporting fixtures. Additional information on bending test procedures is presented in annex E.3.
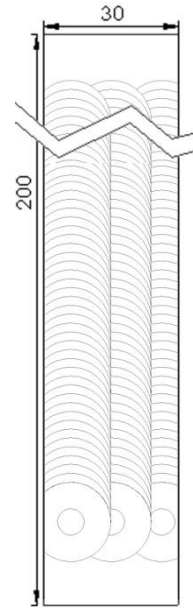
Figure 3.9 – Bending runs set-up and composite test samples dimensions.

Vibration damping test

AA 1100 with and without reinforcements were tested for induced impulse frequency response. Two types of tests were made with: natural frequency, where first natural frequency was measured; damping response, where the material was characterized against its vibration energy loss over time (damping ratio).

Composite response to fixed-free boundary conditions was tested since it reduces undesired vibrations of the coupled accelerometer wires. However this arrangement had some drawbacks: if the cantilevered beam was not sufficiently constrained, undesired vibrations may be depicted. Further, material frequency is heavily dependent on initial impulse direction vectors and position, as different flexure and torsion frequency modes may be induced if the impulse is not well targeted on the composite surface. Figure 3.10 illustrates experimental set-up for both vibration tests made.
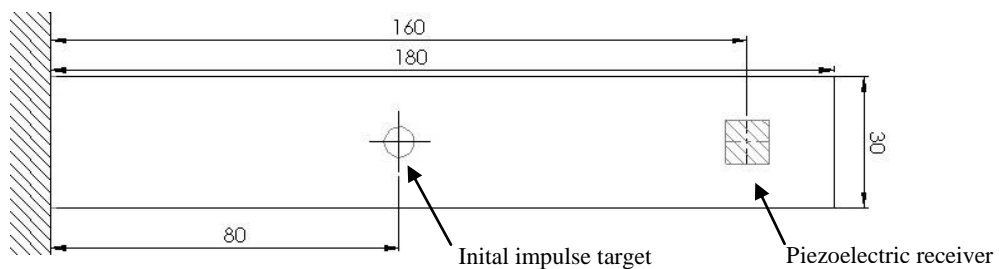
Figure 3.10 – Experimental set-up of fixed-free constrained composite beam for vibration testing.

40

Figure 3.11 shows the composite in fixed-free assemblage, a clamping fixture was used to maintain good constrain rigidity. An accelerometer equipped hammer, Dynapulse™, with a hard polymeric hammer head was connected to a data hub for data acquisition. A NI-USB6251 data hub was used to measure the vibration response.

Dedicated software developed in LabVIEW® plot vibration charts, allowing further data treatment. The hammer triggers the initial impulse, the beam response overtime is measured with one coupled piezoelectric accelerometer also connected to a data hub and LabVIEW® specially designed program. The program outputs the magnitude, imaginary and real frequency values of the coupled piezoelectric receiver; while the hammer built-in accelerometer measures amplitude of induced impulses. Additional information on vibration test procedures is presented in annex E.4.
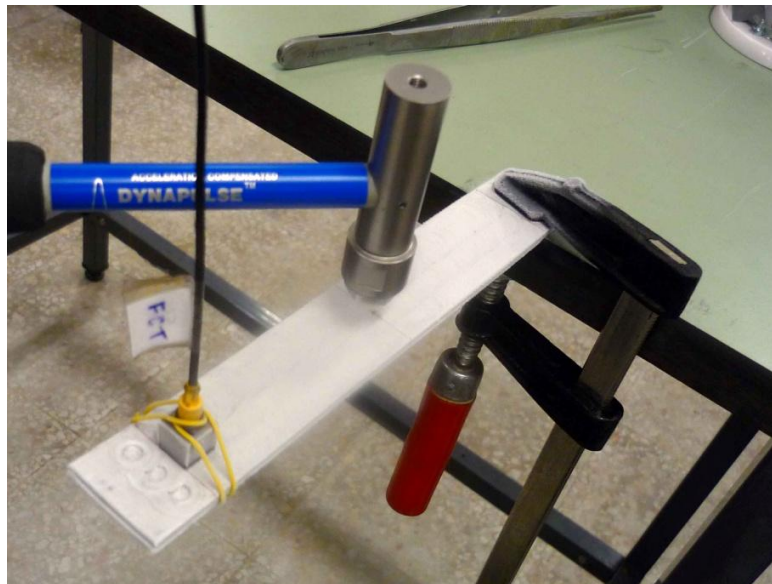
Figure 3.11 – Testing of sample D13 after being cooled for 2 minutes in liquid nitrogen.

Natural frequency tested specimens were first performed at ambient temperature. Five trials were made per sample and the average value calculated. The impulse was made 8 cm apart from the fixed position and the piezoelectric receiver was coupled at 16 cm apart from the fixed position. The composite materials were mounted with the FSW pin exit hole facing outwards. The fixture system was securely fasten to guarantee high fix rigidity response (since any undesired fixture vibrations, while testing the specimens, would scramble the measured frequencies).

3.4.4. Eddy currents testing

The electrical conductivity, σ, was measured using eddy currents inspection method. Tests were performed to investigate the electromagnetic response of the friction stir welded composites. The induced electromagnetic field relies on two major properties of the tested material: magnetic permeability and electrical conductivity. The self electromagnetic field of the material disturbs the exciting coil field, therefore being able to "sense" the material response through the same exciting coil.

Sectioned 30x200 mm, width and length, respectively, samples were milled at different thicknesses, see figure 3.12, using a two flute HSS 6 mm diameter end mill. Samples were tested in an automated X-Y device controlled by step motors [77]. A multifunction Olympus® NORTEC 500C data acquisition system was used to acquire impedance signals.

Dedicated software developed in Labview® was used to control the X–Y device, acquire data, and to control the test parameters. An Olympus™ pencil probe, with frequency range from 50KHZ to 500KHZ and 3 mm diameter was used. The probe was coaxially displaced along the weld width and measurements were taken in intervals of 200 μm, in a 20 mm displacement. Results were processed in Matlab® to plot charts of impedance along the weld width.
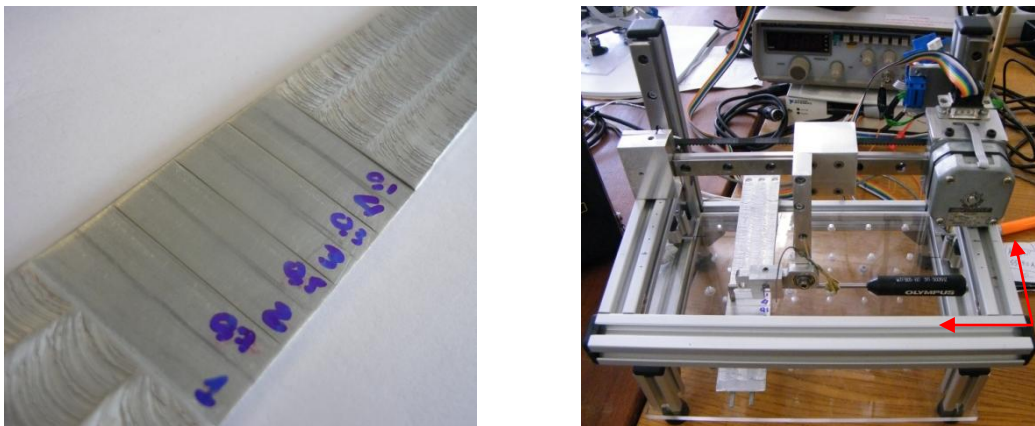
Figure 3.12 – Left– example of FSWed sample with NiTi reinforcements, after multi-pass milling at different thicknesses; (1 – 0,7 mm; 2 – 0,5 mm; 3 – 0,3 mm; 4 – 0,1 mm). Right – experimental set-up of NiTi reinforced pass no. 4 with X–Y device.

Eddy current penetration depth is directly related to the skin effect phenomena. This is characterized by the exponential distribution of the induced currents along the thickness of the material. Equation 3.2 shows the current intensity variation in thickness [78].

$$I_x = I_0 \cdot e^{-x(\pi \cdot f \cdot \mu \cdot \sigma)^{1/2}} \qquad\qquad (3.2)$$

Where I_x is current intensity at given depth, I_0 is current intensity at surface, f is the induced excitation frequency, μ is the magnetic permeability and σ the electrical conductivity. A minimum of current density of e^{-1} or 37 % relative to surface is defined as the depth if penetration, δ, equation 3.3. Preliminary tests were performed at different frequencies, from 10 to 100 KHz [78].

$$\delta = \frac{1}{\sqrt{\pi \cdot f \cdot \mu \cdot \sigma}} \qquad\qquad (3.3)$$

Where δ is penetration depth, f is the induced excitation frequency, μ is the magnetic permeability and σ the electrical conductivity. Each pass was tested at 10, 25, 50 and 100 KHZ resulting in different induced field penetration depths measured. Results were later grouped by frequency.

Electrical conductivity

Normalized electrical conductivity was performed in several composites, an Olympus SPO-887L 60KHZ pencil probe with 7mm diameter was used. A relatively straightforward test methodology compares the electromagnetic response of standard materials (with known electrical conductivity ratios, in % IACS) against the new composite's electromagnetic field, measured by the exciting coil. The same tests were be made in base material, processed bead, overlapped beads with and without reinforcements, in order to evaluate different material conductivities. Preliminary tests showed a high electrical conductivity, hence the normalized electrical conductivity was compared against copper (100 % IACS) and Olympus® conductivity standard plate setup with 58,98 % IACS. Additional information on electromagnetic induced field test procedures is presented in annex E.5.

3.5.   Conclusions

The experimental approach previously described allowed to produce sound specimens, further analyzed, in order to assess composite properties and the impact of those by changing process parameters and reinforcement strategies.

4. RESULTS AND DISCUSSION

This chapter discusses the results obtained in this study. Mechanical properties of bulk material will be compared against the new friction stir welded samples, starting with some notes on the supplied material and the expected properties outcome. Moreover, a thorough analysis of materials' behavior in FSW beads will be discussed. The expected outcome in joint features of the faying surfaces and the embedded ribbons was not entirely met, giving rise to trial group D.

4.1. Base and reinforcing material

Base material was characterized for microstructural and mechanical properties. Wrought AA 1100 aluminium alloy as-received had no specifications on its stress-strain response curve, and therefore a characterization was necessary. Figure 4.1 shows the as-received material, etched to reveal grain boundaries. The grain shape shows an anisotropic structure, originated by cold rolling operation, with the presence of few precipitates.

Figure 4.1 – As-received AA 1100 cold hardened and partially annealed, section parallel to rolling direction

The stress-strain curve, plotted in figure 4.2, is characteristic of a very ductile material, but low resistance (UTS is of about 55 MPa). Comparing this value with the one from the material specification, that is of about 90 MPa [11], it can be seen that the material may have undergone a thermal treatment that promoted diffusion and rearrangement of defects, in an annealing like treatment that softened the alloy.
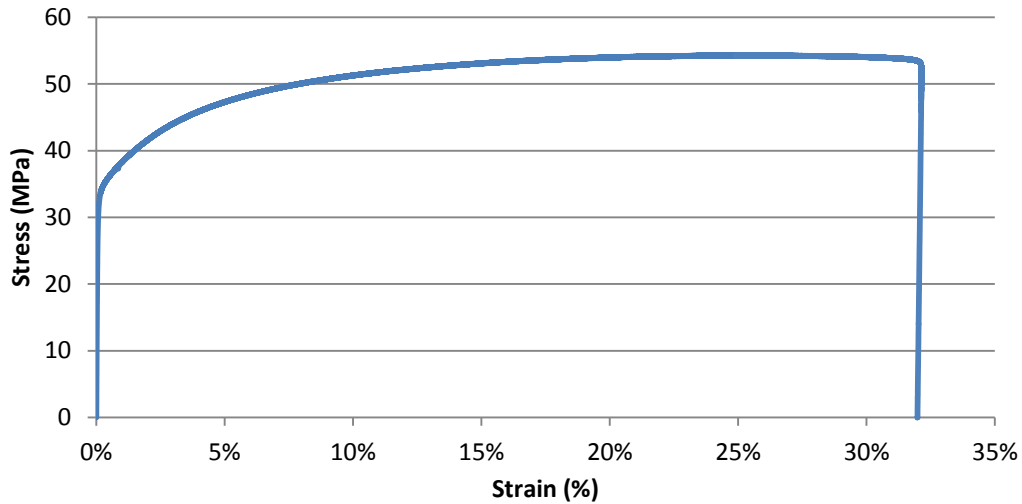
Figure 4.2 – Stress-strain curve of AA 1100 aluminium alloy.

As-received NiTi alloy presented an oxidized layer, also common in this alloys the supplied material received a cold working treatment. A tensile test was performed on the 0.9 x 2.8 mm ribbons.

Figure 4.3 shows the stress-strain response and it is clear that the hardening treatment destroyed the functional properties of NiTi. A superelastic plateau is not depicted and the stress induced martensite strain hardening slope is also absent. This alloy shows a great elastic elongation without any noticeable phase change.

On the other hand, the NiTi present great stiffness on its austenitic phase. These results suggest the possibility of austenitic finish temperature change, from the original -15 ºC alloy N.
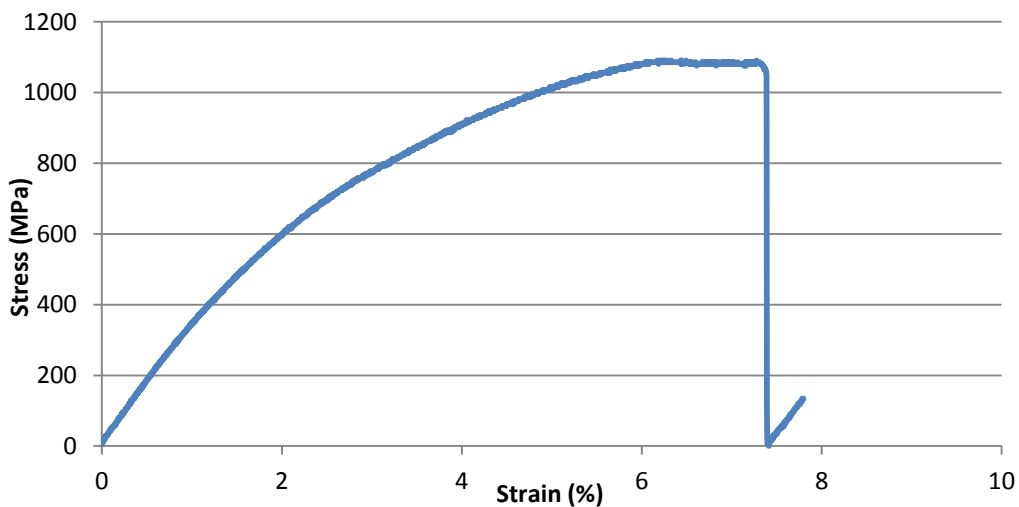
Figure 4.3 – Stress-strain curve of NiTi alloy N.

46

Later, a NiTi ribbon sample, subjected to the composite manufacturing by FSW, was removed from the composite's bulk and tensile tested. Results shown in figure 4.5, depicts a good similarity between this and the former non-processed material. Therefore, the composite manufacturing methodology used did not promote any significant mechanical property changes. However, further testing should be performed to investigate the functional properties after processing.
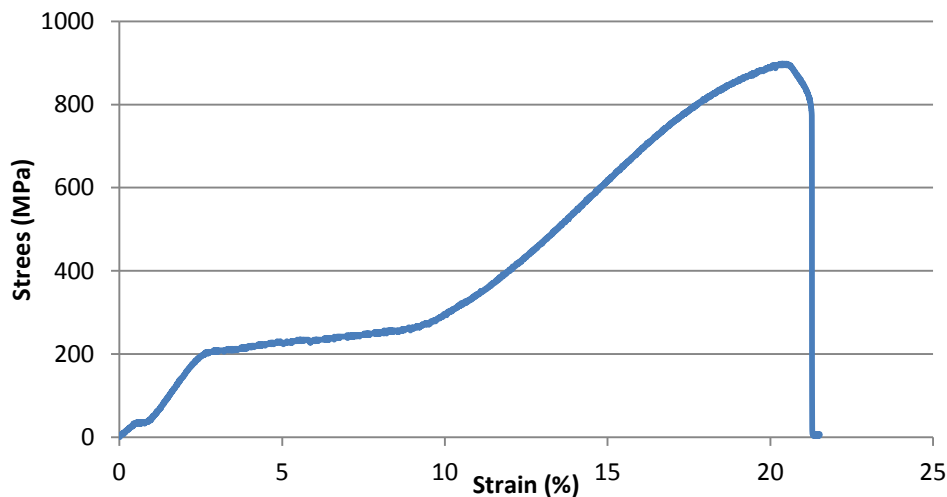
Figure 4.5 – Stress-strain curve of NiTi after heat treatment at 500 °C for 20 minutes and FSW in AA 1100 composite.

4.2. FSW lap joint of AA 1100 without reinforcements

4.2.1. The impact of tool penetration on surface weld beads

Figure 4.6 shows one of the samples produced by increasing plunge depth (trial group A) with tool position control, it is distinguishable the surface roughness and non uniformity along the weld bead. Starting with the initial (X-axis position = 0 mm) force peak of about 3000 KN due to the tool plunge; after, FSW high dwell time resulted in somewhat pronounced flash formation, excessive heat and increased material viscosplastic behavior. Chart demonstrates a relief in tool force upon starting the traversal tool movement, to a minimum value of about 1200 KN resulting in brittle crack formation of the surface until a steady value of 1900 ±150 KN produced a smoother almost crack free weld bead.
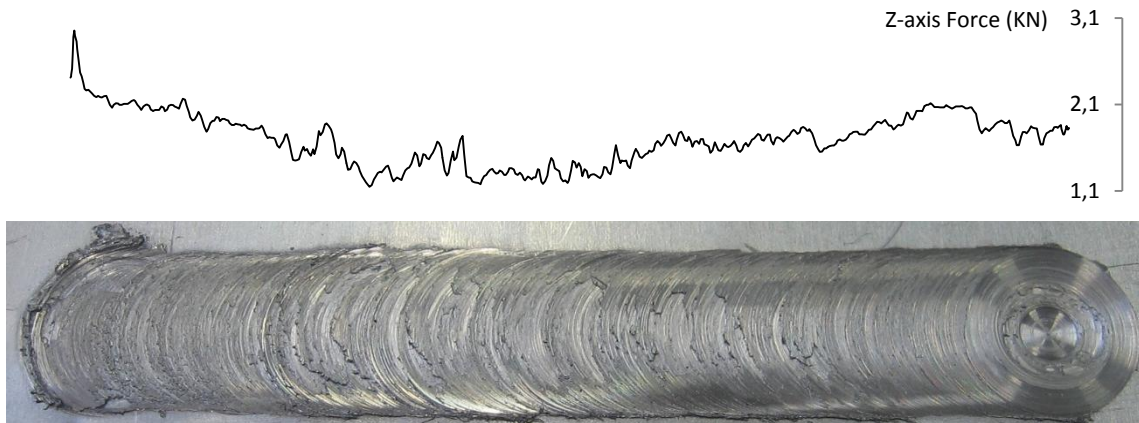
Figure 4.6 – Sample produced with -1.60 mm PD and traverse and rotational speeds of 50 mm/min and 800 rev/min, respectively.

The expected tool force regularity was not achieved along the weld bead, since FSW hydraulic control of the Z-axis could hardly cope with the initial welding parameters. Excessive softening increased the tool plunge into the material, and, in response, hydraulic tool control automatically reduced the applied force. Further on, the reestablished material viscosity along the weld pass resulted in a new increment in the tool force. Neither voids nor channel like defects were observed on the weld surfaces.

Figure 4.7 shows the micrographic characterization of the first tested AA 1100 lap joints by FSW, with PD = -1.4 mm. Pressure applied during the process resulted in a waved faying surface close to the SZ, where the interface between the two AA 1100 sheets withstands higher temperatures. Figure 4.7 b and c show the stirred zone surpassing the interface between the two sheets; notwithstanding, a distinctive oxide layer delineated between sheets suggests that a proper lap joint was not attained. In fact several lap joints failed during specimen preparation for metallography. Also, a non-homogeneous oxide accumulation along the SZ suggests that processing conditions were not sufficient to generate an effective oxide disruption along the weld width. Figure 4.7 a) and e) microscopies allow to understand the material flow in the retreating and advancing sides, respectively: The first warping oxide profile is distinctive of retreating side lower strain rate and increased material accumulation, the opposite advancing side oxide tail depicted (figure 4.7 e), is a result of the more eccentric and increased material strain and vertical material flow in this region.

This undesired non-homogenized oxide banded flow lines decrease with the increment of PD in 0.1 mm (figure 4.8). A more uniform thickness layer is attained with the increased pin penetration; threaded pin induced flow upwards to the material surface increases oxide spreading in the intensive plastic deformed zone, also, SZ height and width increased for the same working parameters: Resulting in a welded interface region packed with oxides. The conical SZ shape was not wider from the former sample, this suggests that the increased PH was

48

prominent to create a higher SZ but the widening was a consequence of similar conical shape. This is relevant to assess the amount of heat generated (a wider weld nugget suggest a 'hotter' welding process than a narrower nugget) therefore the increase in PD augmented the material flow but probably kept a 'similar' heat generation.

Figure 4.8 c) shows several oxide bands in the SZ center with two easily depicted opposite directions, from the original material upward flow, just below the flat bottomed pin. Figure 4.8 b) displays an "S" shape oxide lines typical of the highly deformed grain boundaries with elongated shapes, where plastic deformation and temperature was not enough to induce dynamic recrystallization (DR), rather creating this transition area between the highly deformed SZ and the un-welded plate thinned sheet interface of figure 4.8 a). On the opposite AS, the upward rotated unwelded interface is clearly depicted. This particular hooking defect presents an odd void on the tip that eventually caused an earlier interruption of the oxide layer break while welding.

The sample with PD of -1.6 mm (figure 4.9) shows also a very dissimilar weld cross section from the former ones with the slight increase of 0.1 mm (~3 % of the lap joint thickness) in the tool plunge. It is clear that the increased tool penetration increases the flash formation and surface roughness. Figure 4.9 d) shows a hooking on the AS of the upper plate, the increased PD resulted in a smaller hooking defect and an increase of RS plate thinning (figure 4.9 a), former studies validate the latter results [41, 60]. Most interesting result is the drastically increased SZ depth, almost full thickness SZ was achieved in the AS, whilst on the RS a proper joint was not achieved just below the shoulder's induced flow – the latter suggests that after oxide disruption of the faying interfaces the material flow, in the two sheets, perform in a very complex way. While on the AS, the shear mechanisms of the tool enhances oxide dissemination, on the RS the compacted oxide bands hinders the faying surface from joining.

The AS oxide free, highly reactive, surfaces multiplies the effect of the pin induced flow until almost full thickness of the SZ, figure 4.9 c) shows the tail of a linear oxide agglomeration, it is evident the amount of pull effect from the upward material flow on the oxide layer (figure 4.9 b). To note that first the pin broke this layer and severely stirred these oxide agglomeration, only after, shoulder forging forces leveled the oxides to this very uncommon layer linearity.
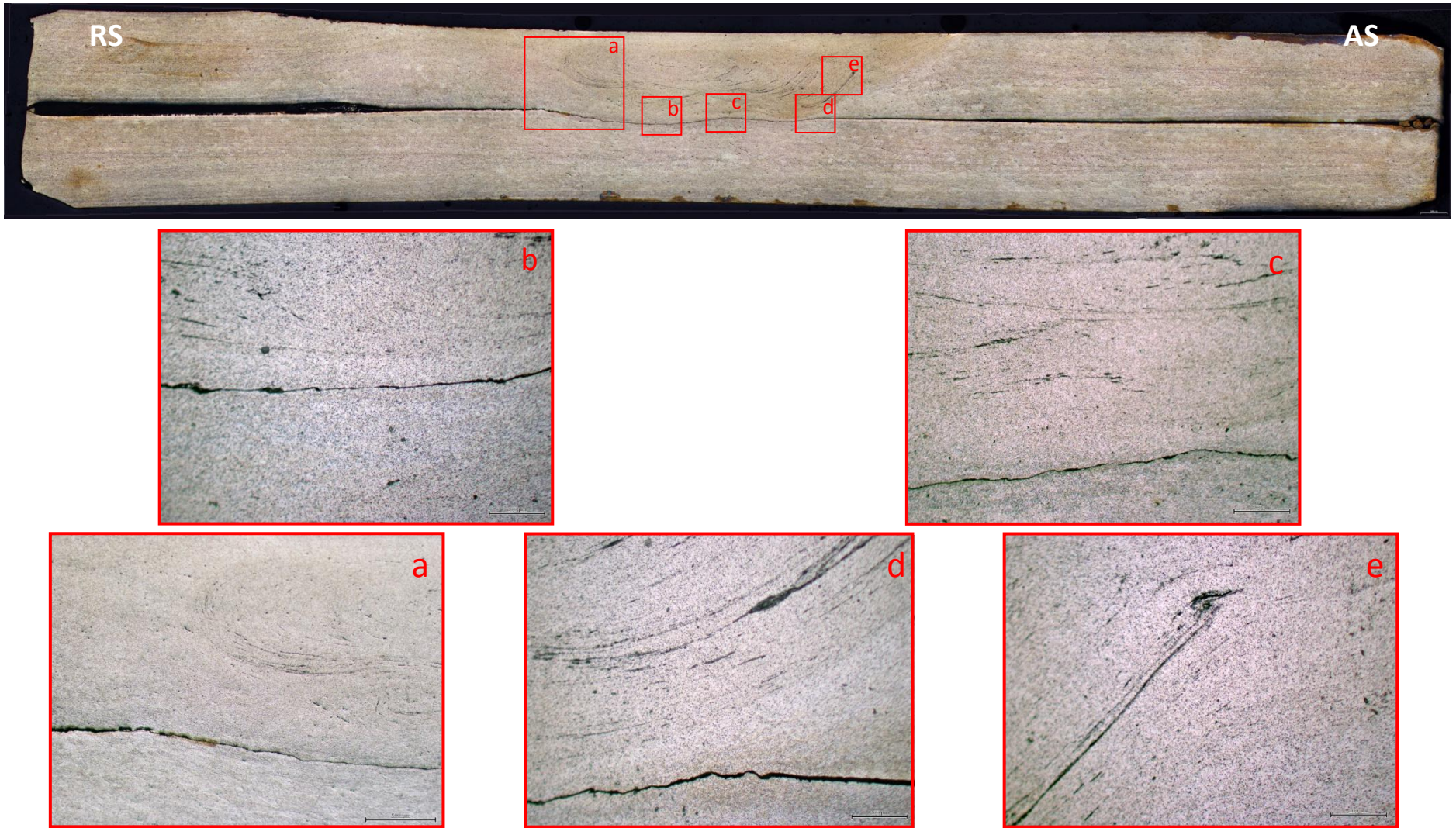
Figure 4.7 – Cross section of AA 1100 lap jointed by FSW with -1.4 mm PD.
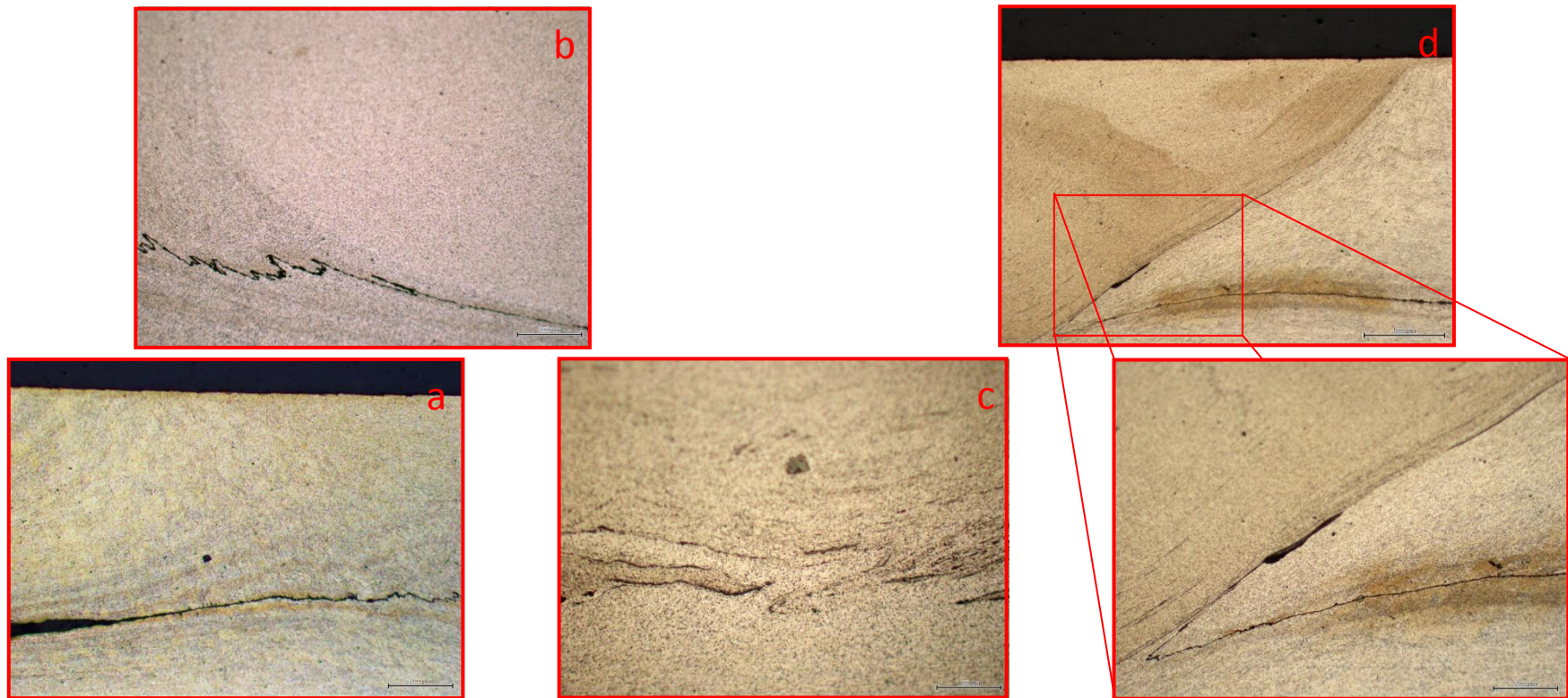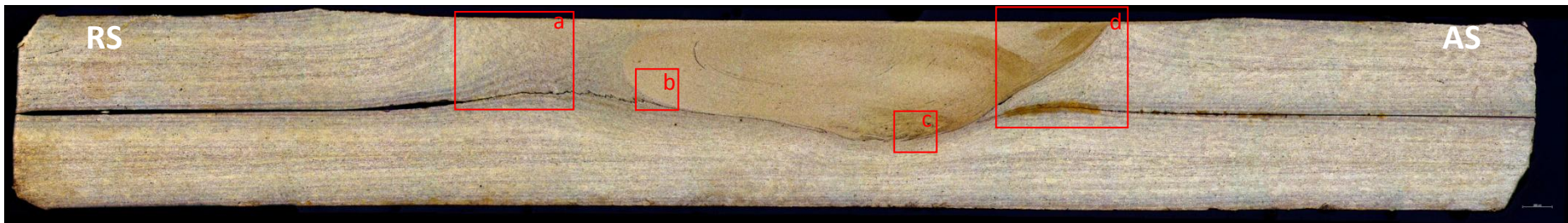
Figure 4.8 – Cross section of aluminium lap jointed by FSW with -1.5 mm PD.
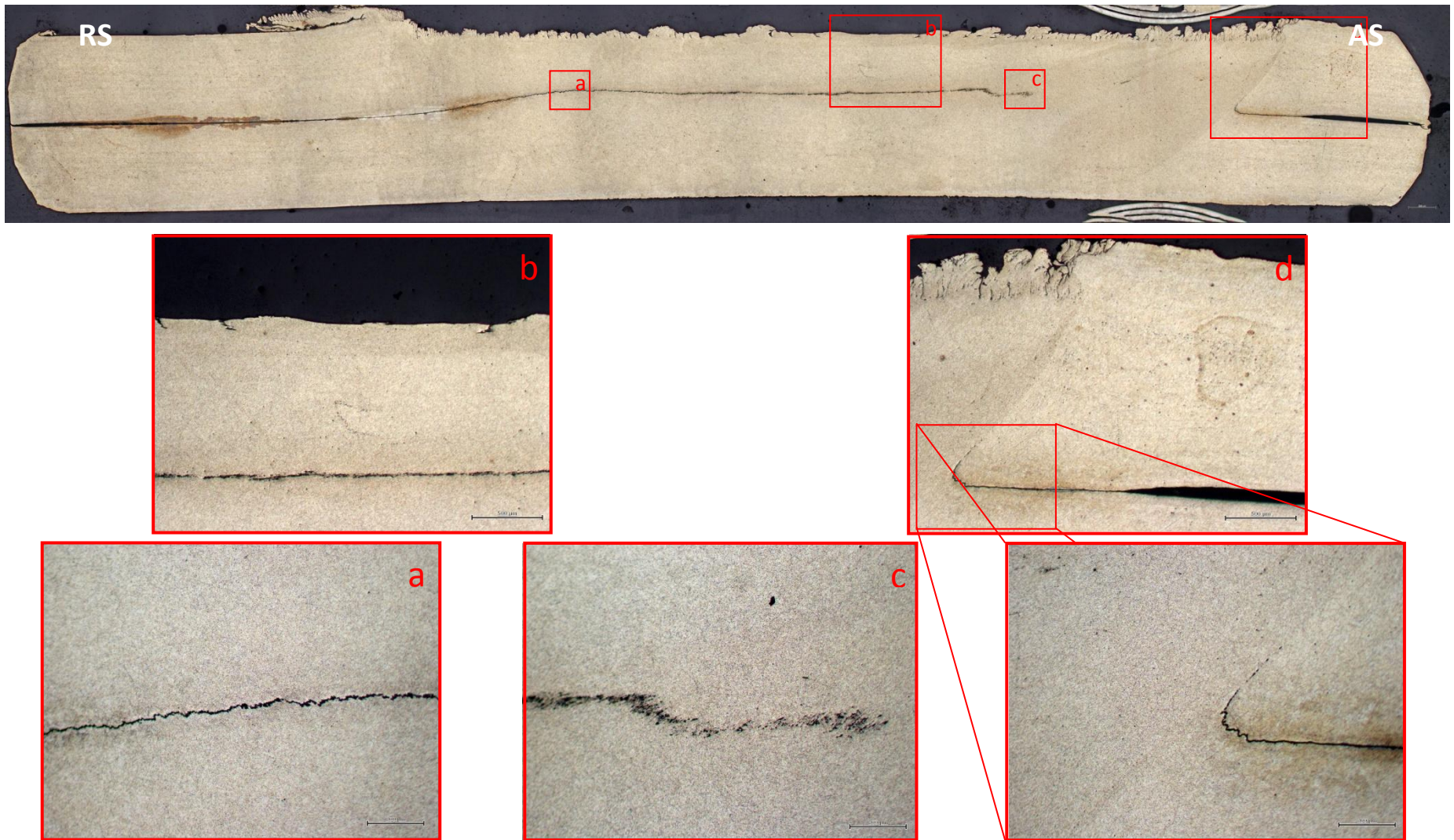
Figure 4.9 – Cross section of aluminium lap jointed by FSW with -1.6 mm PD.

4.2.2. Multi-pass in AA 1100 lap joints

Single-lap FSW lap joints failed to achieve a proper oxide layer disruption in the weld width, multi-pass welding was explored to address this issue and promote the creation of composites with larger widths. Group B trials proposed a partial overlapping changing between FSW sides and full overlapping with traversal movement inversion.

Figure 4.10 shows the impact on overlapping by the AS (a), the RS (b). It is noticeable the resulting weld bead roughness from the two different methods. While overlapping by the AS produced a sound even weld bead, the opposite overlapping by the RS produced a curly surface. Full overlapping produced sound surface weld beads, similar to single-lap pass welds, nevertheless preliminary trials easily failed on specimen preparation and did not achieve a proper interface bonding – as so, they were not further developed.

(a) overlapping by the AS

(b) overlapping by the RS
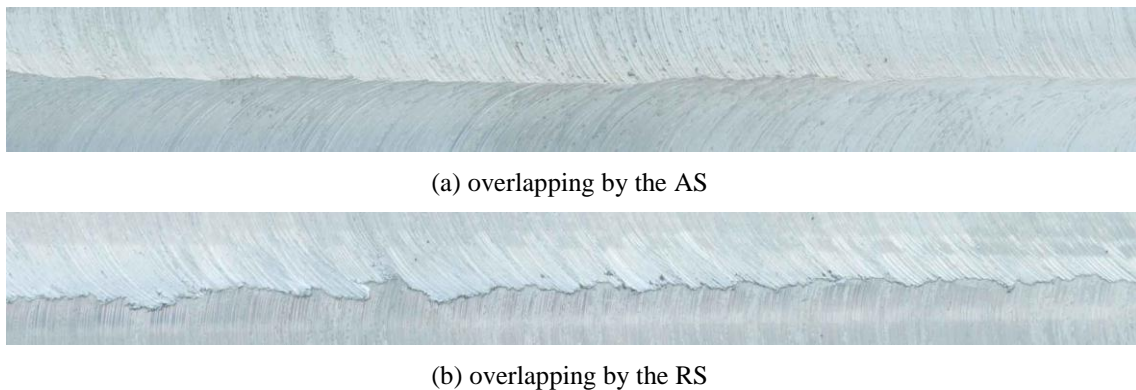
Figure 4.10 – details of surfaces weld beads overlapping by the AS (a) an by the RS (b).

Since an overlap ratio of 0.8 was used, the SZ interpenetration was assured, also, it is easy to understand that, after FSW, the affected zones present different mechanical properties due to plastic deformation and heat generated. On the dynamic recrystallized zone, a smaller and equiaxial grain formation develops a harder and stiffer stirred zone. Therefore, when overlapping by the RS there is a clash of a softer and a harder material from the previous weld pass – same as dissimilar material welding, when overlapping by a softer material. In overlapping by the RS, this newly processed material 'struggles' to shear and crack the previously processed, harder material, in the stirring zone – while creating a viscoplastic material flow around the pin – hence a shear lip of the softer overlapping material is formed around at surface.

Figure 4.11, shows the lack of shear lip binding and cavities formation of the RS overlapping the former harder AS. A lack of material binding is noticed, between the two passes, suggesting that the former processed material properties is greatly modified, resulting in a dissimilar material behavior-like.

The surface layer of figure 4.10 a) shows that the AS produces a smooth surface – the positive velocity sum of the rotating and traversal tool movements, increases the intermixture with the RS of the anterior FSW pass, imposing a stronger shearing action and successfully producing a shear lip free weld bead.
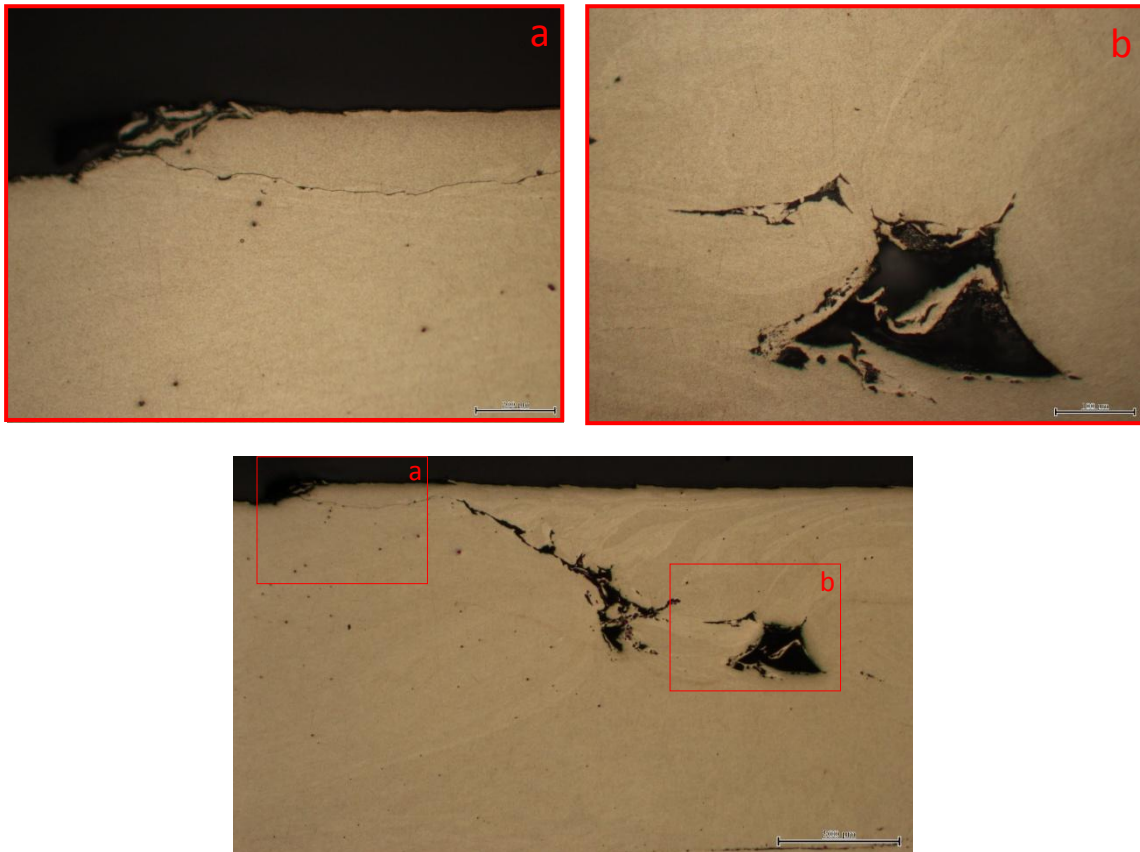
Figure 4.11 – Microscopic detail of sample B2 with overlapped weld bead by the retreating side. (a) unbounded shear lip of the latter pass, (b) cavities formation due to lack of RS material penetration and shearing of the former processed AS.

Overlapping by the AS with a ratio of 0.8 ensures volume void and channel free defects, as shown figure 4.12. Figure 4.12 a) depicts the plate thinning waved interface, with a thickness reduction of the upper sheet. On the left side of the same image, the faying surfaces present no joining; while on the opposite side, a joined surface is depicted with an oxide layer amongst them: This retreating side presents a steadier oxide layer, in the TMAZ. Diffusion bonding mechanisms were responsible for grain coalescence at interfaces between HAZ and thermo-mechanically affected zones, although, there is an oxide layer which hinders the complete coalescence of the faying surfaces, up to a point where metallurgical mechanisms, that make a dominant contribution to the bonding process, are not sufficient to trigger diffusion mechanisms.

From figure 4.12 a) plate thinning to f) interface hooking there is a complete joint of the former faying interface, no voids or channels are depicted along the width and the thickness. The more turbulent oxide spreading delimits the SZ of the different FSW passes, on the AS of each pass a more diffused oxide tail-like feature is noticeable, while on RS where the material exhibits a downward material flow, as figure 4.12 e) shows.

TMAZ and HAZ present a more uniform oxide layer, figure 4.12 d) zig-zag oxide lines clearly depicts the crystallographic evolution of this region: Although there was no dynamic recrystallization, heat generated and plastic strain resulted in grain coalescence and vertical grain elongation.
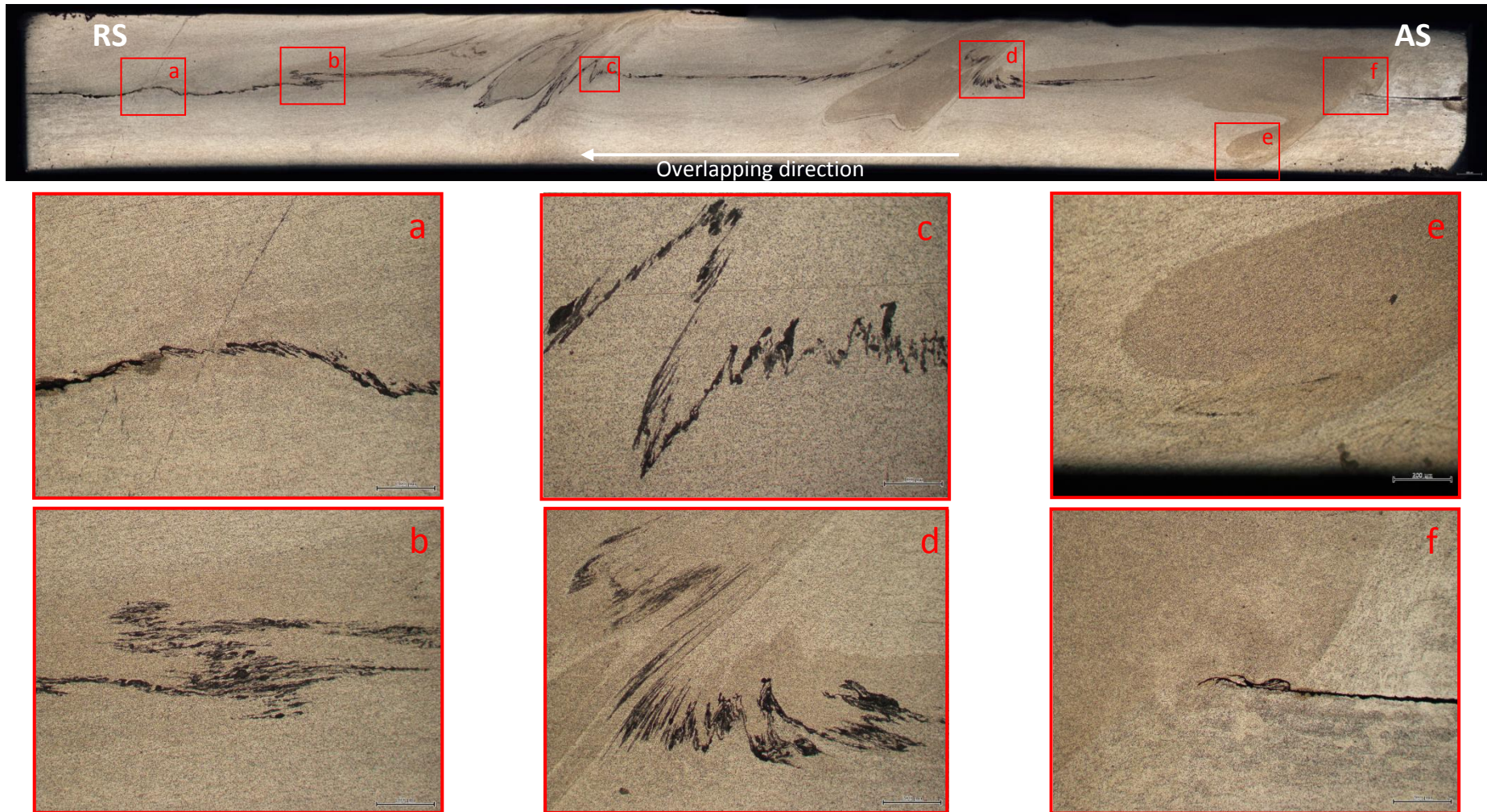
Figure 4.12 – Cross section of overlapping aluminium lap jointed by FSW. v = 80 mm/min; ω = 800 rev/min; PH = 1.64 mm; PD = -1.65 mm; Force control = 1800 KN

4.2.3. Effect of the tool lift-off

Figure 4.13 summarises data from all samples with different shoulder operating distances to the surface, calculated from the relation between PH and PD. PD higher than PH resulted in tool plunging, the opposite, PD smaller than PH resulted in reduced shoulder contact (since TA allowed somewhat tool plunging in the base material at his trail edge). Tool tilt produced a dissimilar contact at any instant along the weld bead, than it was limited to a minimum possible to achieve a proper material inlet at the front of the tool.
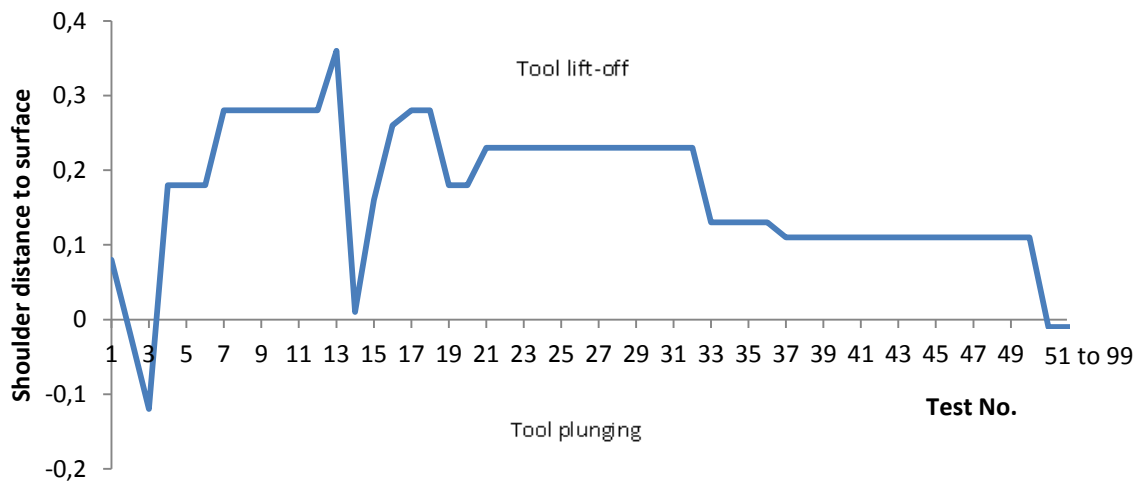
Figure 4.13 – Shoulder distance to samples surface. From 51 to 99 shoulder distance was kept the same. (see annex A for more information about in testing parameters)
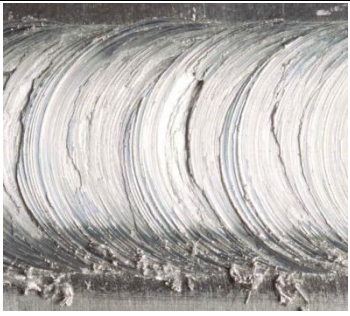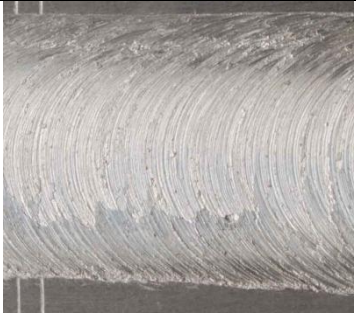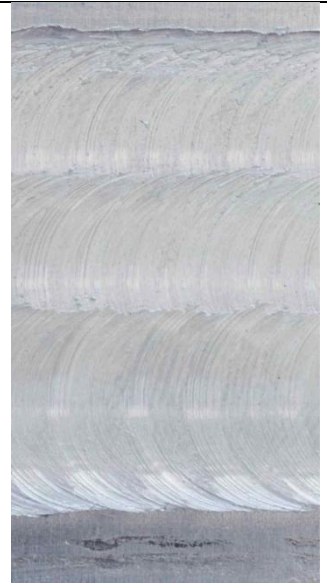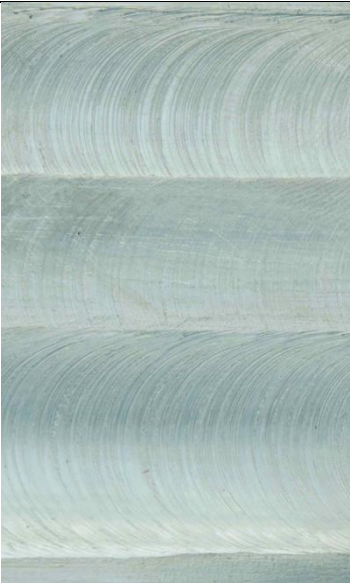
In figure 4.13, the first tests (from 1 to 21) produced very dissimilar PH and PD, since several parameters were being first-tested for lap joint configuration. From sample 21 onwards a convergence of the shoulder distance to a negative distance (tool plunging) is noticeable, with four distinct convergence tiers. A stationary sound weld condition was achieved from 51 onwards, corresponding to 2.5 % of pin penetration into the base plate and a slight shoulder penetration (less than 1%) into the upper plate. Former studies suggest a higher value of pin penetration (between 10 and 20 % of the base plate) to achieve a higher effective joint width, although the discrepancy between the former and the latter results are largely related to the aluminium alloys used in the investigations. As previously discussed, this highly formable AA 1100 aluminium alloy produces somewhat higher SWW, with reduced base plate pin penetration, compared to former studies [41, 60].

Table 4.1 shows some of the surfaces produced at different shoulder distances. Samples 5 and 12 depict several surface brittle cracks due to a faint and intermittent contact between shoulder and base material surface, resulting low heat generation was not sufficient to 'soften' the initial surface material, and so, the rotating shoulder shearing action produced non-continuous circular flow lines along the weld bead. Comparing trials 26 and 27 to trial 5, the latter has a reduced shoulder distance to surface material, 26 and 27 (or B1) have a more homogeneous surface weld bead. Therefore, shoulder distance is not the unique responsible factor to produce differently shaped surfaces. As expected, heat generation, pin induced flow and material surface conditions may also be some of the preponderant factors for resultant surface weld beads morphology.

The decreasing shoulder distance to surface increases shear lip and flash formation. Several attempts were made to reduce these undesirable effects (*e.g.* changing surface material softness, by leveling pitch and axial force). The best samples produced were with plunging tool (samples from 51 until 99 have a slight plunging of 0.01 mm), such small tolerance requires an effective plunge depth control.

It is of paramount importance to have a correct plunge depth in the weld formation because material flow under the shoulder is also governed by the amount of plunge depth, hence, force control method in FSW was found to produce more regular surface weld beads, compared to position control.

Table 4.1 – Weld bead surfaces of some of the samples produced by FSW in lap joint configuration.

N5	N12	N15

N17	B1 (26 and 27)	C3 (37 and 38)

C4 (39, 40 and 41)	D11 (66,67 and 68)

4.2.4. Tensile testing

Figure 4.14 shows the aluminium lap joints after being tensile tested to rupture and the first sample (left side) was depicted to compare the initial length of the sample.

Figure 4.14 – Aluminium lap joint tensile test samples; (a) overlapping FSW by the AS, from left to right, untested sample, 1800 KN axial force FSW tested sample, 2000 KN axial force FSW tested sample; (b) detail of 2000 KN sample, (c) detail of 1800 KN sample.

As expected, the specimens tested produced high elongation values up to failure. Figures 4.14 c) and d) details the cross section of the tested samples, complete failure comes through a three-stage structural change: First, during extensive tensile deformation, the material decreases in cross-section area (necking), as the Poisson effect suggests; secondly the necking reduces the cross section area, rapidly increasing the stress applied; as the strain increases, the heterogeneous FSW microvoids grow and coalesce; last-stage, void growth forms large dimples up rupture. Figure 4.14 c) exhibits numerous cuplike depressions that are the direct result of microvoid coalescence, figure 4.14 b) shows resultant cavities after rupture. Tensile testing curves are presented in figure 4.15.
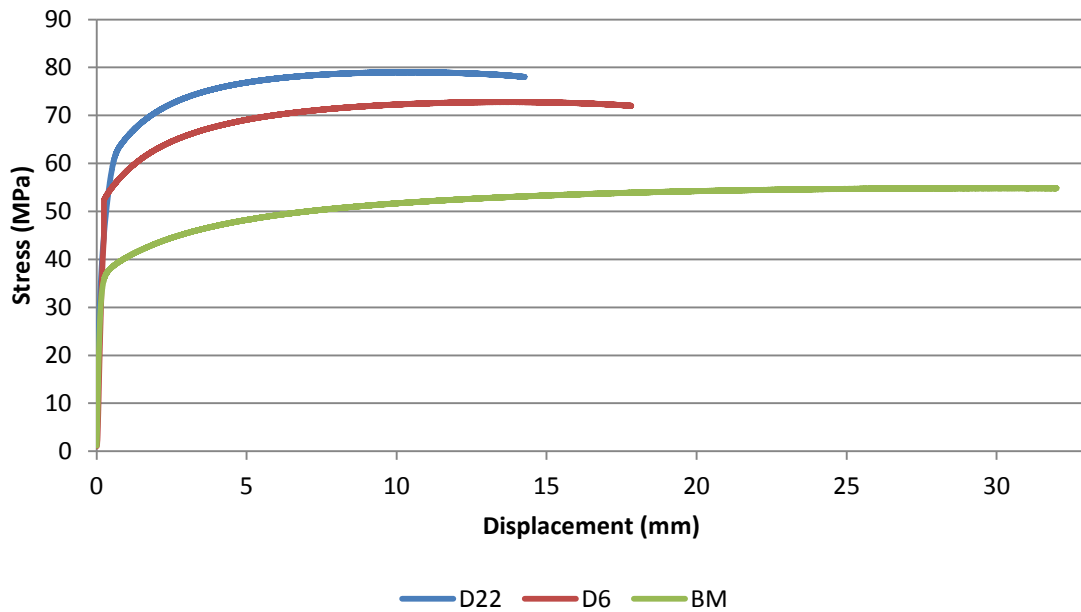
Figure 4.15 – Tensile testing stress-strain curves of D22 (at 800 rev /min, 80 mm/min and 1800 KN), D6 (at 800 rev /min, 80 mm/min and 2000 KN) and base material.

FSW aluminium lap-joints present an increase of about 50 % in UTS and greater yield stress increase of about 70%, compared to BM – both resultant of recrystallized grain structure from the FSW intensive plastic deformation, leading to a close packed fine grain microstructure with increased hardness, according to Hall-Petch equation, and stiffness.

The stress-strain chart shows test specimen D22, FSWed with 1800 KN axial force, with an increase of about 10 % in UTS, compared to D6 with 2000 KN friction stir welded sample. The latter though as an increased strain before rupture, as figure 4.14 a) also shows. It is probable the occurrence of local large voids or cavities in D6, which prompted an earlier crack propagation and rupture, since there is no evident relation between increasing axial force and decreasing UTS. More tensile testing would be required to draw further conclusions.

4.2.5.   Bending testing

Figure 4.16 shows the aluminium lap joint tested specimens. Both samples achieved maximum bent angle of 44 °, due to testing setup restrictions, without failure. Samples were tested at different solicitations; D14 was tested on tensile solicitation, the opposite, D12 on compression.

(a)

(b)

(c)
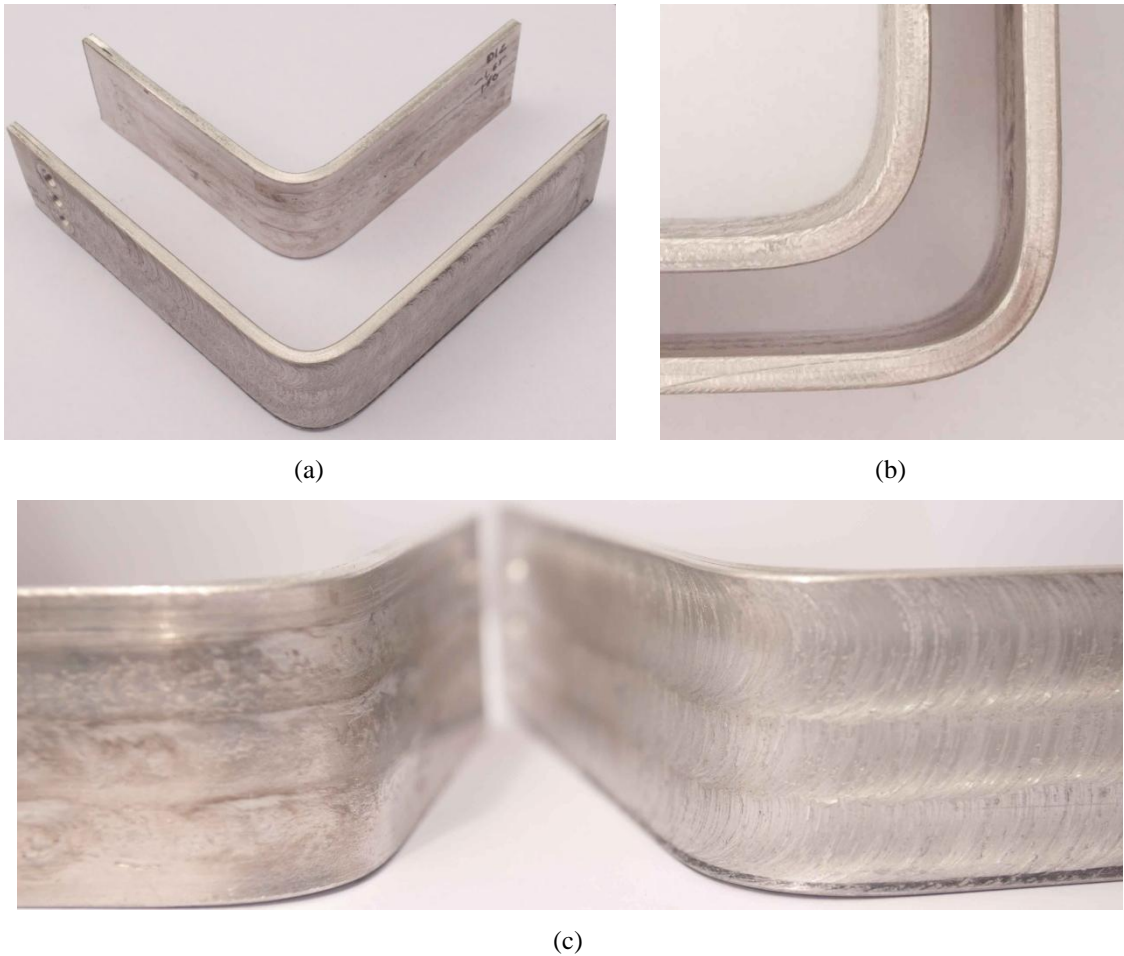
Figure 4.16 – Aluminium lap joint bending test samples; (a) general view of the bent samples at the maximum angle of 44 º, (b) detail view of deformed thickness due to compressive stresses, (c) close-up of the tensile region, no failure is depicted, left (D12) and right (D14).

A slight increase of flexture stress of D14 is depicted in the plotted flexture stress-strain curves (figure 4.17), there was no material rupture at the tensile solicited layer of the bent material (figure 4.16 c), crack propagation mechanisms were not sufficient to cope with material high ductility. Notwithstanding, sample solicited at tensile shows an increase of ~17 % in flexture strength. Figure 4.16 b) shows an increased deformation in the tensile stressed sample; again, this suggests that the recrystallized microstructure as a more uniform strain response that the previously cold worked base plate with uniaxial grain elongation. Bend testing curves are presented in figure 4.17.
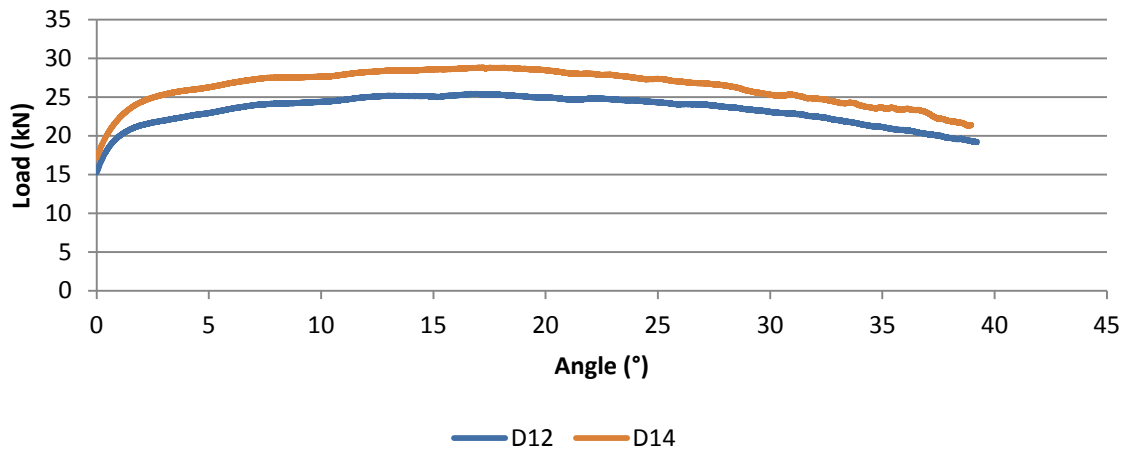
Figure 4.17 – Bent testing of samples D14 and D12, Flexture stress-strain curve.

It is, though, not possible to conclude that tensile solicitation increases flexture strength, more consistent data would be necessary to draw further conclusions.

4.2.6. Summary conclusions

- FSW (in position control) promoted an irregular weld surface and inconsistence of results in various tested samples. Tool axial force control did not cope with the initial process conditions.

- Force control method in FSW was found to produce more regular surface weld beads then position control.

- Single-lap FSW lap joints failed to achieve a proper oxide layer disruption in the weld width, slight increases of tool penetration produced very dissimilar joint features, best results were obtained with a base plate pin penetration of 2,5 % and PD less than 1 % more than PH.

- Dwell time and initial conditions were responsible for the non-stable FSW passes in tool position control. Process was considered stable after a proper pitch ratio was achieved.

- Multi-pass welding greatly increased SWW in lap joint configuration. Overlapping by the AS produced better results, in surface and volume. Tests showed that FSW increases material UTS by 50% and yield strength by 70%.

4.3.   FSW lap joints of AA 1100 with reinforcing materials

Prior to FSW reinforced MMCs with wires and ribbons, AA 1100 base plate was grooved using various techniques. As for the preparation of aluminium specimens for ribbon positioning hydraulic pressing produced the best results.

Pressing allowed a suitable groove opening technique, very acceptable formed specimens were produced with a sound, homogeneous groove in full length, the protuberances (or inter-grooves) presented a flat shape, the surface was scratch-free and without unwanted indentations (Figure 4.18). Seldom, specimens often came with an arch shape between grooves, different groove thickness along the length and other defects on the base plates.
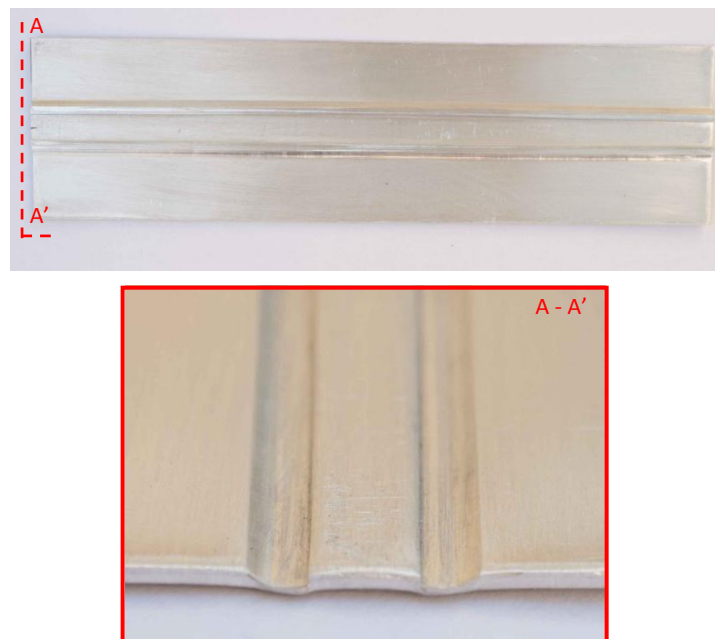
Figure 4.18 – detail of preformed groove using a hydraulic press, prior to positioning the reinforcing materials.

A preliminary visual inspection, on the first steel ribbons reinforced AA 1100 matrices, revealed a very unstable condition upon FSW with similar parameters of the first group A tests. As figure 4.20 a) shows, the steel wire undergoes a wave like twisting, during FSW it was noticeable the reinforcing wire entering into the faying surfaces, see figure 4.19.
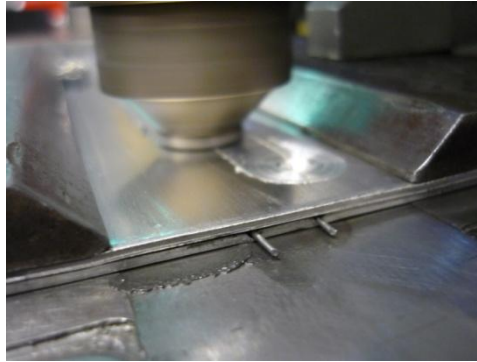
Figure 4.19 – Detail on the remnant wire after positioning the ribbons onto the material matrices.

Figure 4.20 b) and c) shows the X-ray radiography made on FSWed sample weld bead, it is easily depicted the steel wire reinforcement inside the AA 1100 matrix material. The induced matrix material flow promoted a three-dimensional ribbon dislocation, although previous studies consider that this flow undergoes a steady rotary movement within the same direction of the tool rotation. The ribbon bellow comprises almost a sinusoidal wave suggesting that a multitude of forces are applied: Ribbon tensile, through dry friction between the wire and the matrix, on the consolidated trail edge of the tool compound zone; drag through material viscosity, of the stirring pool; and shoulder applied pressure and pin induced torque.
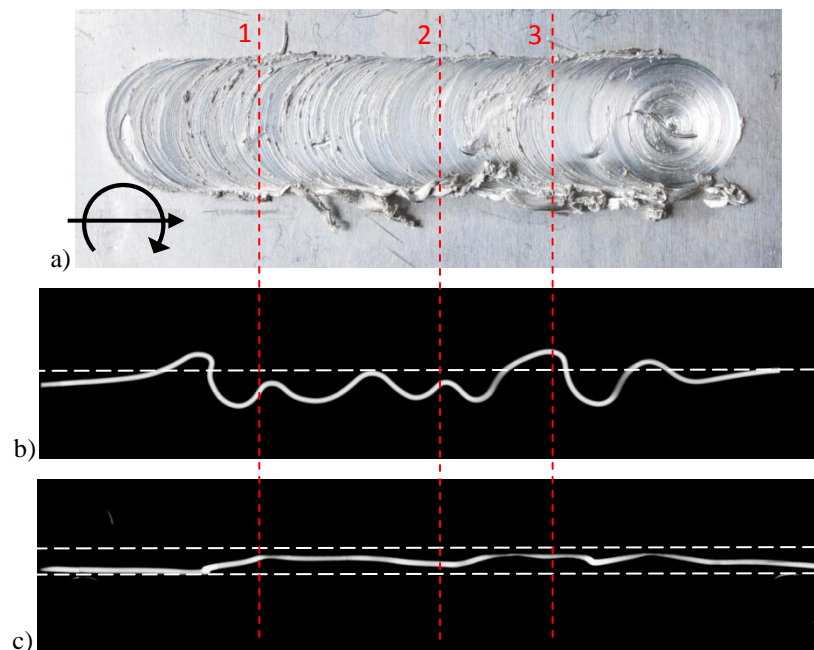
Figure 4.20 – Ribbon wave shape, a) surface wave features, b) top view of the weld bead in X-ray radiography, c) longitudional view of the volume weld in X-ray radiography.

On the other hand, figure 4.20 b) dashed center line demonstrates that the denser steel wire remains 'preferably' on the 'pressure' retreating side along the weld bead – while often entering the AS. At the beginning of the weld, tool downward force plunged the reinforcing wire into the bottom of base material, after, heat generated of the rotating movement promoted an upward viscoplastic material flow and the wire was pushed to the upper sheet, this waved movement is repeated, to a lesser extent, throughout the weld bead.

Macrographs of the dashed lines (1,2 and 3 in figure 4.20) suggest very dissimilar material flows around the reinforcing wire. The wire in figure 4.21 is positioned in the former upper matrix sheet, the overall wire embedment is good although there is no mechanical bonding and crack easily occurs. More, the wire has suffered little or no deformation, a constant widest section (diameter) of the wire can be depicted in all macrographs.
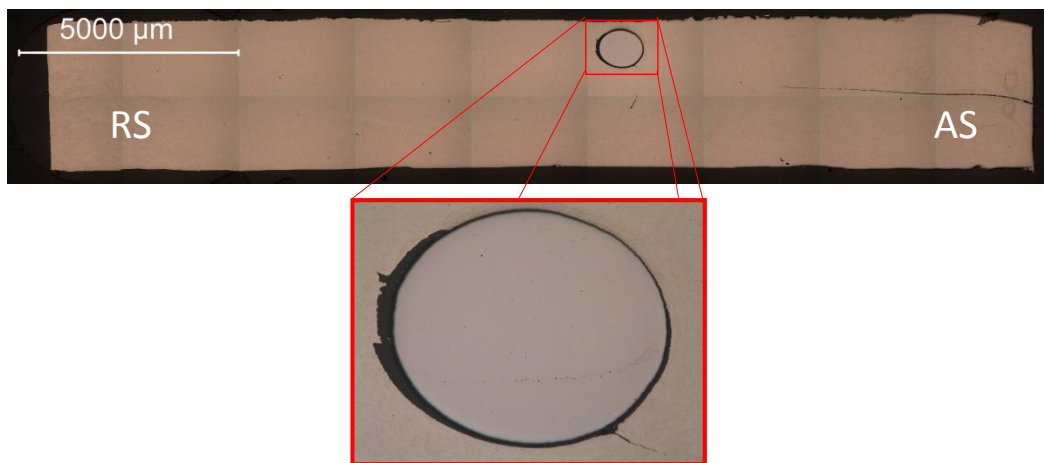
Figure 4.21 – Macrographs of cross section 1 depicted in figure 4.20.

On the other hand, when the wire is positioned in the interface between the faying sheets, there is distinct channel defect on one side of the reinforcing wire. As previously discussed, material strain decreases in depth, because the dominant shoulder induced material flow greatly reduces with distance to shoulder. Figure 4.21 depicts poor wire embedment in the matrix, especially on the retreating side of the wire; reduced plastic deformation, at this depth, and interface oxide and impurities clearly reduces material consolidation.

It is also interesting the fact that both figure 4.21 and 4.22 show a material 'shadow' in the RS (left side of the wire): This lack of filling suggests that excessive material pressure and flow, at the AS, is preponderant and may result in this distinctive 'shadow'. This issue will be addressed further in this work.
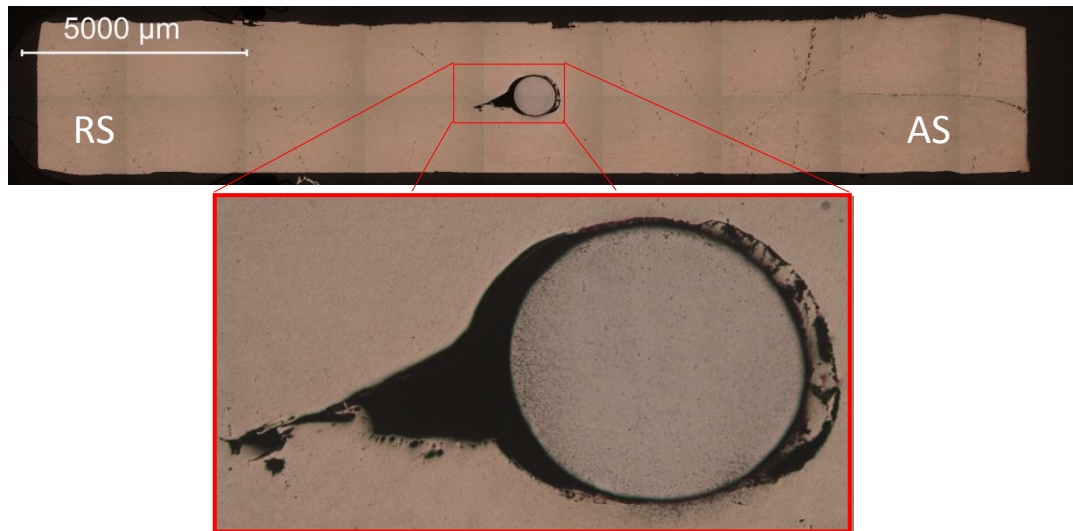
Figure 4.22 – Macrographs of cross section 2 depicted in figure 4.20.

While on the latter macrographs the matrix material shows no impurities or void defects, apart from the ones close to the reinforcements, the macrograph in figure 4.23 shows a very different composite section. Most noticeable is the wire elliptic shape, due to the cross section made from the parent material in figure 4.20.

Detailed micrograph, of the matrix material, shows the presence of material inclusions, those are original from the reinforcing wire, indicating that there was contact between the wire and the harder rotating pin – this caused local wire material shearing and instant spreading across the matrix. The denser steel inclusions, sheared from the original wire, can be found in the retreating side of the welded sample, with the exception of one close to the wire in the AS (shown in bellow micrograph of figure 4.23). On the former cross sectioned macrographs no steel inclusions can be found, suggesting the instantaneous material eccentric scattering occurs after the pin touches the steel wire. Also, voids can be depicted in figure 4.23, suggesting that former steel inclusions were loosened while preparing the sample, due to the poor bonding between the particles and material substrate.
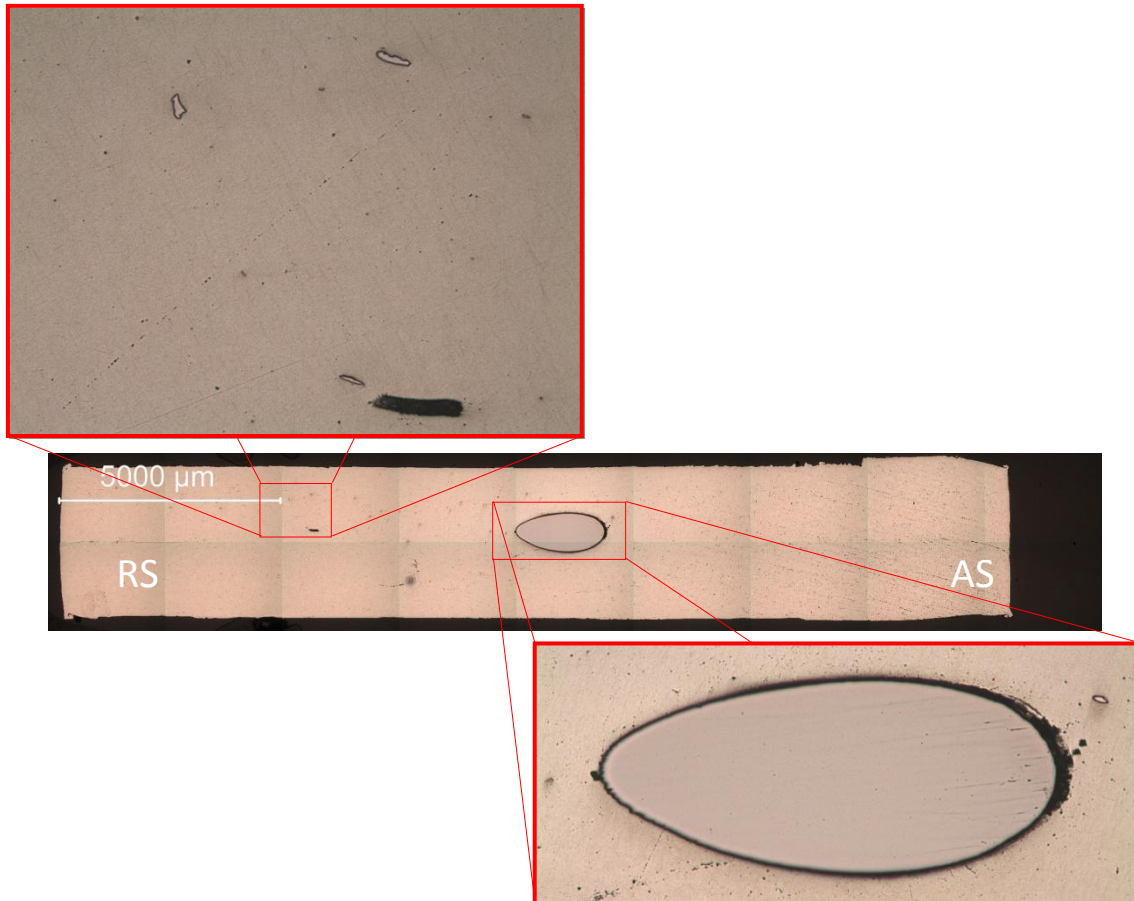
Figure 4.23 – Macrographs of cross section 3 depicted in figure 4.20.

To avoid this wire twisting unstable behavior, a series of parameters was studied. Pitch, as in the longitudinal distance traveled per revolution, is known to be a paramount relation for induced flow and heat generated; in this experiment, every trial with pitch relation bellow 0,1 mm/rot produced unstable wire twisting, although values above the latter produced both stable and unstable wire positioning. Therefore, there is a weak correlation between pitch and reinforcing wiring stability, *per se*, and axial force must be taken into account.

Axial force is not commonly addressed in FSW. This parameter is responsible for pressure applied in volume and volume defects, also, increased axial force may increase shear lip due to material extrusion from the region bellow the tool, producing common surface depressions and volume channel defects. In this case, lap joint configuration, axial force is responsible for: Increased constrain between the faying surfaces; more pressurized (material) viscoplastic flow, resulting in different material flow patterns around the reinforcing wires (this will be further addressed in this work). Also, the impact of applied pressure on wire stability along the weld bead has been studied; applied force over than 1800 KN resulted in unstable wire twisting, while lower force resulted in both stable and unstable conditions. Therefore there is no feasible correlation and only an upper limit can be established.

Opposite to the expected, PD was not a preponderant factor on the stability condition. As figure 4.24 shows, lower PD and pitch did not result in wire stability, as every depicted test presented wire twisting along the weld bead.
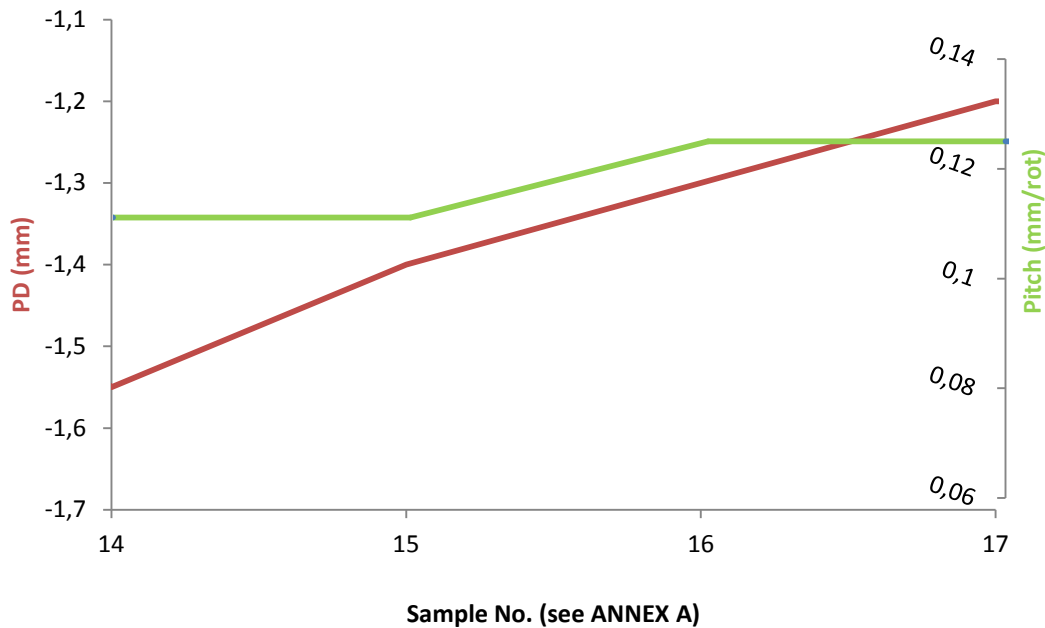
Figure 4.24 – PD and pitch values for samples no. 14, 15, 16 and 17; corresponding to samples N10, N11, N12, N13; every specimen produced unstable wire twisting.

Therefore, there is no correlation between these parameters and wire twisting, even if the formers are combined, figure 4.24. Also, both pitch and axial force, taken alone, present no great advantage if one intends to use them for devising a FSW process without unstable wire twisting. The opposite, both parameters combined present a threshold level, pitch lower than 0.1 mm/rot with axial force greater than 1800 KN, produced straight untwisted wire along the weld beads.

It is known that both increased rotating velocity and applied pressure have a great impact on tool applied torque. Therefore, a dissimilar (stiffer) material implemented on the stirred zone should have a great impact on the matrix material strain and viscoplastic flow, and consequently, on the resulting torque. As figure 4.25 presents, waved wire results in a sinusoidal torque response of the equipment, while the others, stationary wire positioning and base material without reinforcements, present a more linear torque response. To note that in the chart bellow sample D6 (without reinforcements) has the highest torque, in average, but one should not taken into account the absolute values, since every test has its own set of parameters that may lead to different torque levels, and only torque variations along X-axis (welding length) have somewhat relevance.
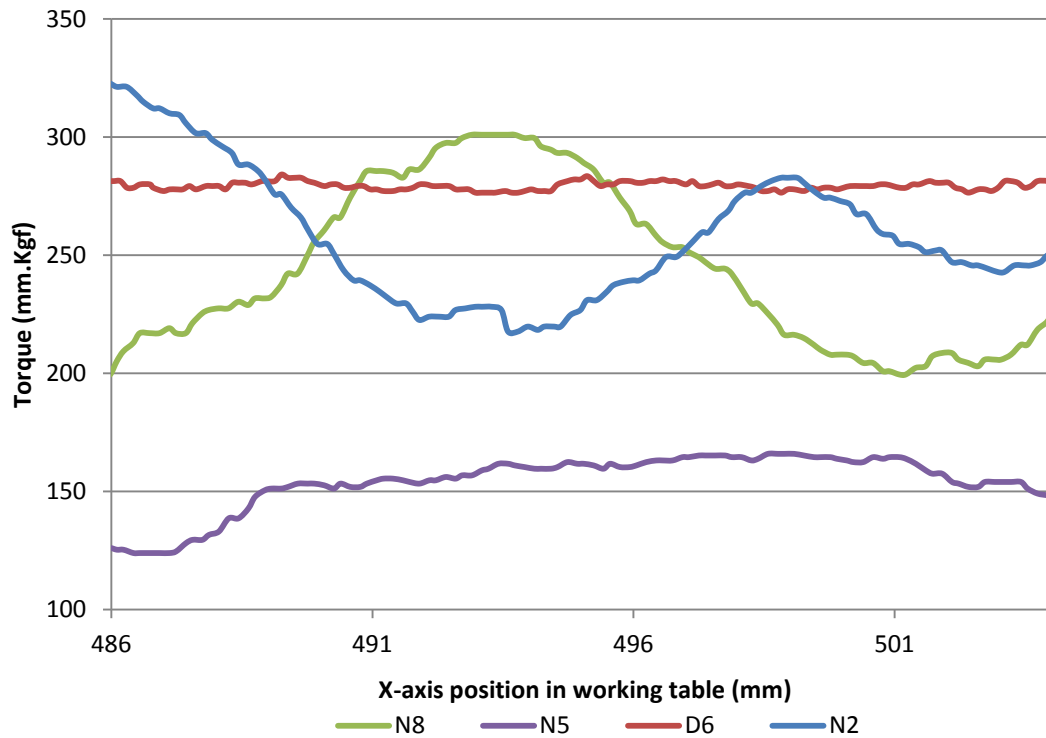
Figure 4.25 – Equipment torque applied on rotating tool during FSW of unstable wire twisting samples (N2 and N8), stable untwisted wire reinforced samples (N5) and without reinforcements (D6).

As discussed, wire twisting along the weld bead often contact with the rotating pin, which may suggest, there was some tool wear. As figure 4.26 depicts, there was slightly no wear tool after several passes; traces of base materials were easily removed from the shoulder with a scriber; at the pin tip, a common agglomeration of aluminium base material was removed, by grinding, between trials – maintaining a good tool geometry, very important for the low tolerance this investigation implies.

Figure 4.26 – Tool threads cleaning after a set of trials, AA 1100 remnant material is being removed with a scriber tool.

4.3.1. The impact of reinforcements on the material flow

Since first trials of AA 1100 lap joints produced, from PD of -1.4 mm until -1.6 mm, a jointed interface, the same conditions were retried with embedded wires into AA 1100 matrices, in lap joint configuration. Figure 4.27 plots sound weld width against tool PD of both lap joints, without reinforcements and reinforced composites.
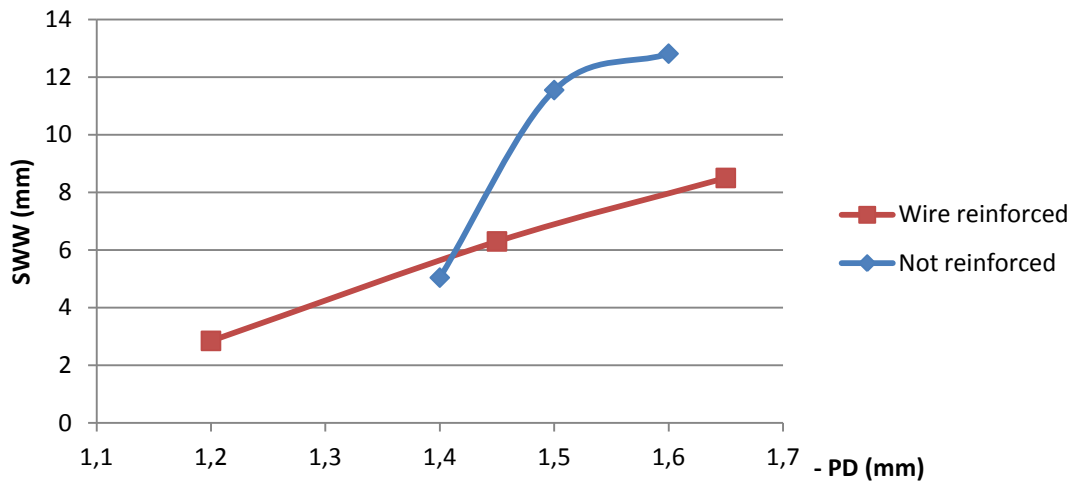
Figure 4.27 – SWW profiles of lap joint AA 1100 without reinforced materials and wire reinforced samples.

In lap joint configuration, the rapidly increasing SWW slows downs upon breaking the interface oxide layer (before -1.6 mm PD). Wire reinforced composites present a more linear SWW increasing along tool plunge depth, with an overall reduced joint welded interface, compared to lap joint without reinforcements. The two major impacts of reinforcing materials on matrix material mixing pool are: First on reducing the material flow, acting as a flow shearing agent that promotes a more turbulent and reduced plastic deformation; secondly, altering both temperature and pressure gradients, responsible for local interface joining by diffusion bonding, when SZ did not went through the materials interface.

By definition, SWW is the minimum distance between the unwelded faying interfaces, and those with reinforcements have reduced jointed interfaces, for the above reported probable causes. Also, if material flow around the wire section does not totally embed the reinforcing element (by producing undesired void and channel defects) a proper local bound is not achieved, resulting in a lower SWW.

Microscopic analysis, on weld bead cross sections with wire reinforcements, shows the impact of different parameters on void and channel defects around the added elements. Microscopic analysis, figure 4.28, shows a distinctive material flow from the right to the left

side, leaving an unbounded wake on the trail side of the wire and an almost complete wire embedment on the front side.
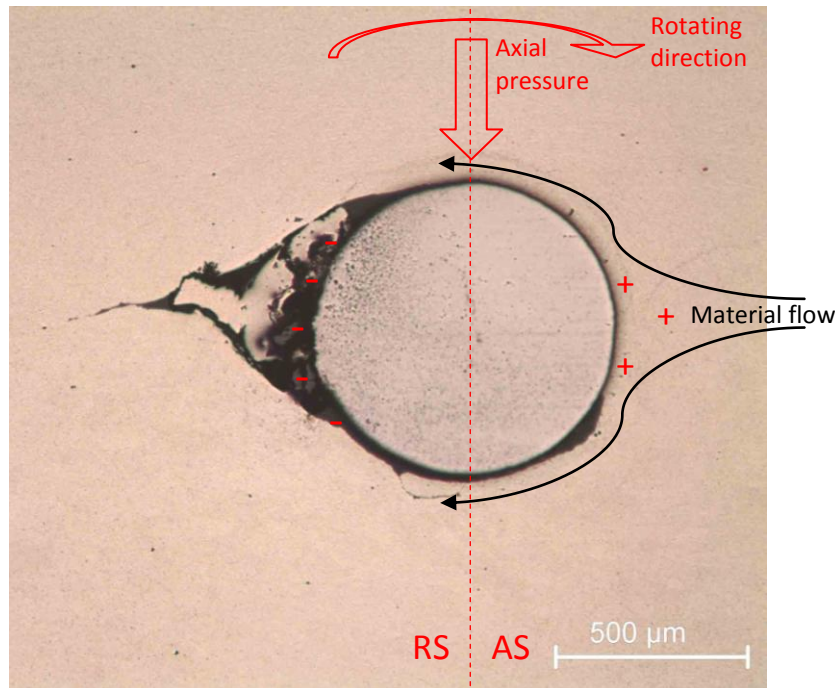
Figure 4.28 – Reinforcing wire detail of sample N3 cross section. (+) increased pressure, (-) decreased pressure, both resulting of material flow from AS to RS.

In the stirring zone, the resulting viscoplastic material flow, from the advancing to the retreating side, is illustrated in the above picture. The 'shadowed' area, depicted in RS, shows that there was a complete deformation of the pre-processed groove to the stirring pool. Those were probably caused by the shearing forces of material flux. Concurrently, the pressure differential resultant from the dissimilar advancing and retreating side (sum of velocity vectors) creates a flow direction easily depicted in figure above.

The wire's AS shows almost a complete wire embedment, the opposite, RS shows a distinctive channel defect: on the AS, the high viscoplastic pressure near the leading edge impels flow around the wire, after, near the widest section of the wire, the boundary layers separate from each side and form two shear layers, which latter bound the wake. At the trail, high pressure differential around the disturbing 'object' produced this common flow pattern, similar to Von Karman street vortices.

In order to avoid this low pressure material void, at the trail, different methodologies were suggested: The axisymmetric pin geometry resulted in somewhat homogeneous rotating flow, the impact of a differently radial shaped pin could result in a more turbulent eccentric material flow and a more dispersed pressure differential; offsetting the FSW tool could lead to a

more evenly distributed pressure; by FSW multi-pass the former low pressure differential zone could result in the latter high pressure zone, by changing pin and shoulder induced pressures from one side to the other of the wire. Due to time constrains a new tool could not be designed and only different tool positions were tested. Table 4.2 shows differently shaped flow patterns at the wire trail edge resultant from different tool offsets, multi-passes and parameters.

Table 4.2 – Material flow patterns of FSW in lap joint configuration samples with reinforcing elements. /AS on the right side of samples cross section).

Sample N12 – 'Cold' welding conditions (high pitch); produced a very irregular surface, also, pin point contacted with the wire several times along the weld bead, while operating the tool experienced excessive vibration. The process resultant flash formation suggested that void or volume defects were being created by the pin induced upward flow.
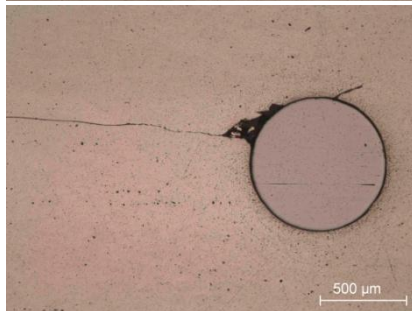
Sample N14 – Same pitch as before only with decreased PH, produced a much more regular surface and thickness weld bead, decreased pin induced flow produced almost no voids. Although there was no sufficient tool forging action to bound RS material faying surfaces.
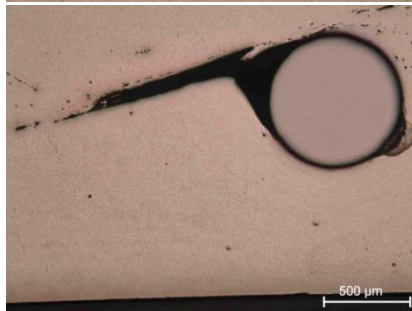
Sample N18 – First trialed sample in force control with 1200 KN; there is a similarity with the first depicted image, this was a slightly 'hotter' weld than N12, but less PH and reduced applied force in half. Most interesting, both trials produced excessive tool vibration.
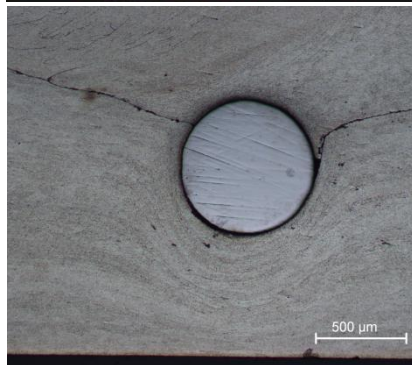
Sample C4 – Three pass overlapping FSW; the wire depicted first went through a FSW pass on the right side and after, a second pass on the left side. The RS side of the first pass produced no void defects, the second pass AS produced a slight void on the previously recrystallized material of the wire right side.

Sample D10 – Multi-pass overlapping successfully minimizes the material flow defects, around the disturbing 'object'; the unbonded region of the material at wire's right side was probably caused by a faulty Z-axis 'zero position' (see annex A), production of samples with ribbons will be further discussed.

73

Contrasted macrographs, of the reinforced materials, better acquaint the preponderant metallurgical mechanisms of processed AA 1100, with dissimilar reinforcing materials.

Figure 4.30 shows sample C4 cross section, with wire reinforcements. Here too, the recrystallized stirred zone of the three FSW passes is easily distinguishable. The more intense three darker areas are the advancing sides with reduced grain size, due to increased strain and grain recrystallization. The former faying surfaces have an almost linear oxide layer amidst them, which can only be depicted after etching the sample cross section. There is a distinguishable plate thinning on the RS of the last pass, figure 4.30 a) shows the beginning of the bounded interfaces with this faying oxide layer, which is dispersed upon entering RS stirred zone, highly deformed ring shaped viscoplastic deformation. Figures 4.30 b) and c) suggest how oxide layer is affected in the weld width, figure 4.30 c) details the beginning of the bounded interface, without almost no hooking – going into accordance with former results in this work, the reduced tool forging action and pin induced flow outputs less material mixing and upward flow, therefore reducing plate thinning upward rotation (hooking).

Figures 4.30 d), e) and f) better shows that the overall wire embedment was good, although there is a clear distinguishable physical interface between matrix and wire, suggesting that there was no diffusion triggered by heat or pressure, hence there is no chemical bonding; further mechanical testing will allow to understand the type of bonding between them.

Comparing to single lap, multi-lap presents a lack of material embedment on the opposite side of the former single laps; first the wire withstands the RS material flow action on his right side, after ,the AS of the second pass on his left side finishes the wire enclosing. The RS low plastic deformation is not sufficient to create a material flow that surpasses the widest wire section, so the material is constrained in the same side of the wire; after, the AS highly eccentric material flow that surpasses the wire section, and its viscoplastic material flux creates a pressure differential between the front side of the wire and the trail edge, which creates a small cavity downstream wire (figure 4.30 f).

Figure 4.31 shows several cross sections micrographs of NiTi ribbon reinforced AA 1100 matrix material. The overall bounding is almost total, to exception of small voids (*e.g.* figure 4.31 a) and few interfaces between ribbon and matrix. As can be observed, there is more oxide dispersion, compared to the former analysed wire reinforced composite, suggesting that the increased tool force and pin induced flow promoted more oxide breakage and scattering. The stirring zones are easily identifiable by the darker, brown colored, areas (resultant of more grain boundaries etched per unit of area, as so, smaller recrystallized grain), figure 4.31 e) and f) shows a vortex of oxide remnants in both material interfaces, with an upward flow stream,

suggesting that material flow, disturbing 'object,' counter pressure promoted these oxide alignment.

Figure 4.31 d) shows an oxide layer interface perpendicular to ribbon, this may potentiate crack propagation and sheet delamination since it is a more brittle oxide packed layer. Reinforced ribbon on the left failed maintain a horizontal linearity, this very uncommon result may be related to a faulty ribbon position or groove forming before FSW, although more commonly, multi-pass FSW with wire and ribbons presented a regular reinforcement position, as the X-ray radiography in figure 4.29 shows.

Figure 4.29 – Longitudinal X-ray radiography of sample C4.
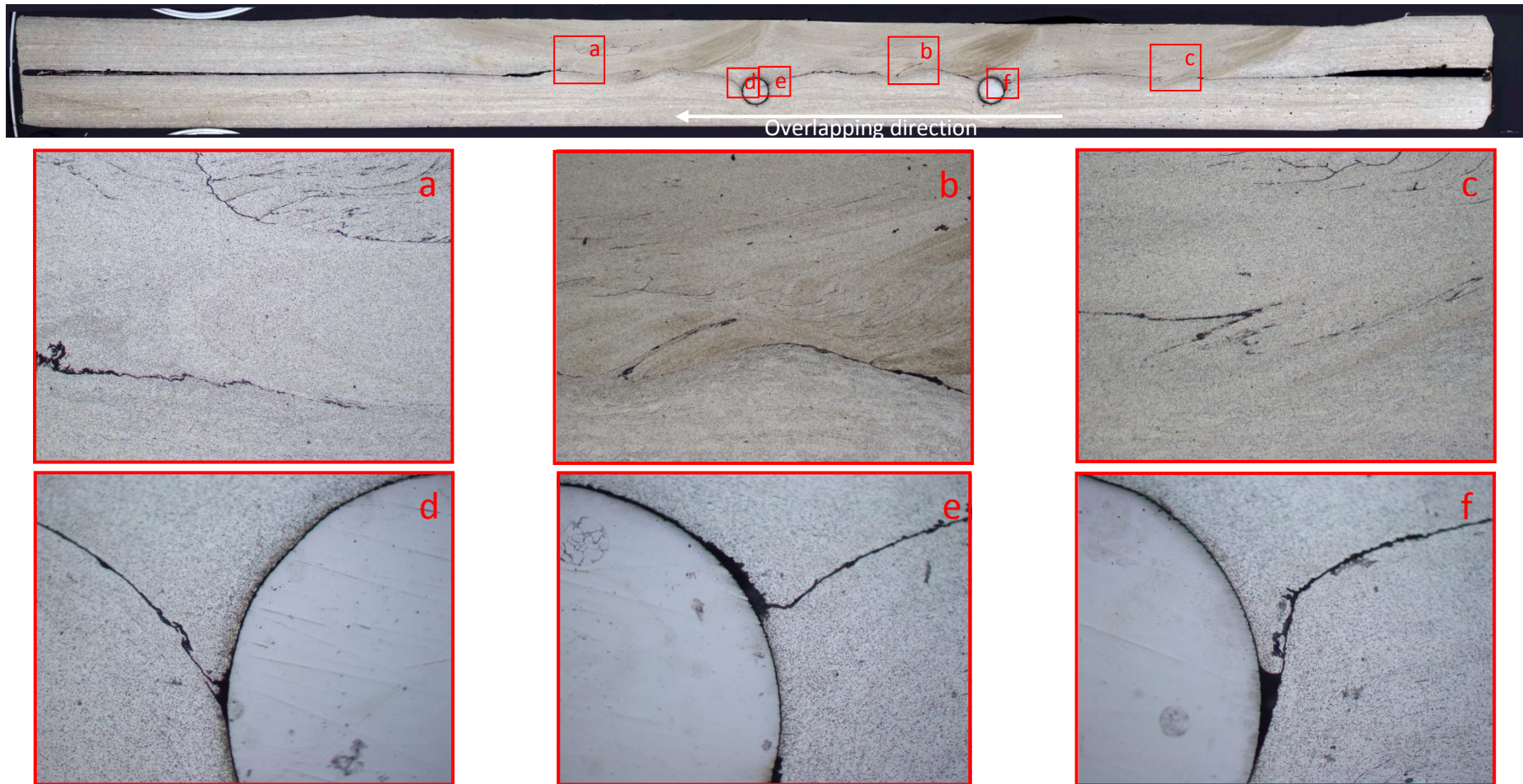
Figure 4.30 – Cross section of overlapping aluminium lap jointed by FSW. Sample C4 v = 80 mm/min; ω = 800 rev/min; PH = 1.56 mm; PD = -1.45 mm; Force control = 1400 KN
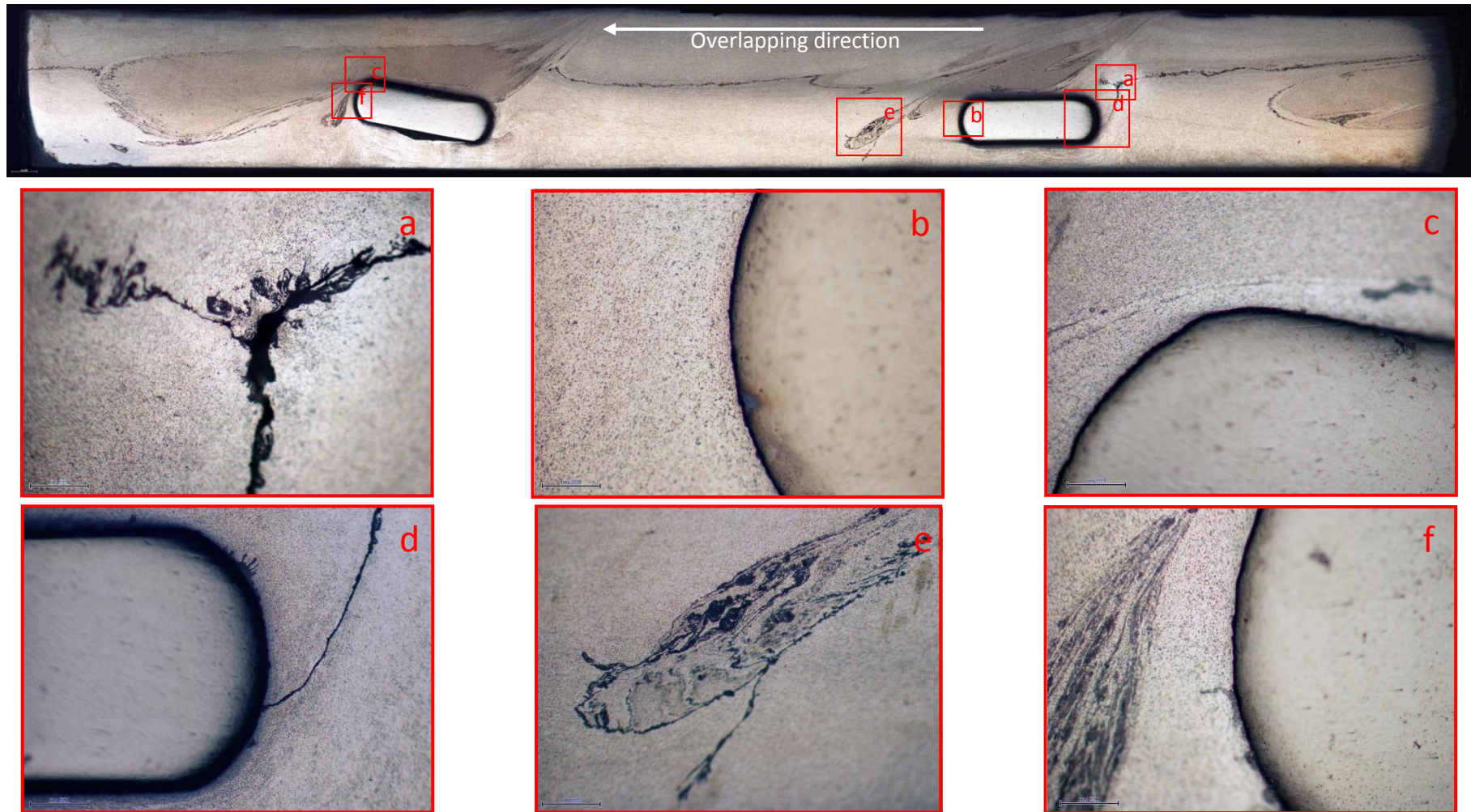
Figure 4.31 – Cross section of overlapping aluminium lap jointed by FSW. Sample D10 v = 80 mm/min; ω = 800 rev/min; PH = 1.64 mm; PD = -1.65 mm; Force control = 1800 KN.

4.3.2. Scanning electron microscope and energy dispersive X-ray spectroscopy

To study the interface between matrix and reinforcing materials, scanning electron microscope (SEM) was performed in composite cross sections. Figure 4.32 shows sample D10 detailed interface between NiTi and AA 1100 matrix.
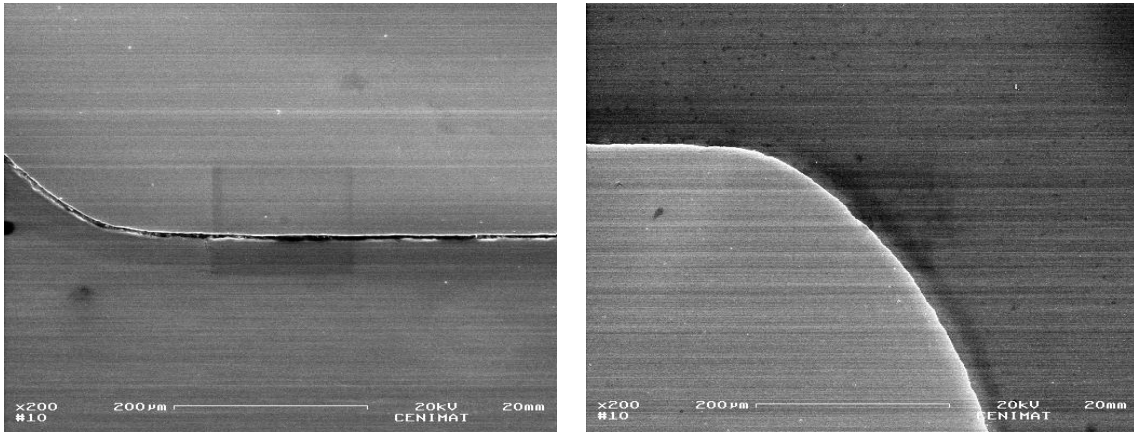
Figure 4.32 – Left – metallic faying interfaces; Right – interface cohesion with clearly defined physical boundary between materials. Both images from NiTi reinforced sample D10, taken with secondary electrons SEM detector.

Although image resolution was affected by electron beam continuous discharges (due to the low conductivity oxide layers formed in the pre polished materials), figure 4.32 on the left clearly shows an unwelded region of the NiTi reinforcement on the bottom part of the composite. As previously suggested, some areas of the reinforcements suffered different material pressures, while processing. The gap depicted in the above figure, on the left, shows white areas in the interface, suggesting the presence of inorganic and non conductive particles within the interface gap. This bottom part of the reinforcement allows understanding the impact of such pressure differentials, same ribbon is showed on figure 4.32, right ribbon.

On the other hand, figure 4.33 shows a good embedment of the reinforcing material. The NiTi rough waved shape has been totally covered by the intensively deformed matrix materials. Contrarily to the former observation, this interface was subjected to high compressive forces, resulting from the stirred material flow of the FSW and the disturbing 'object' counter pressure.
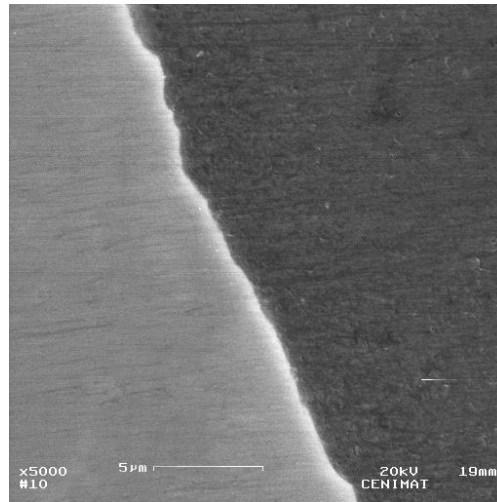
Figure 4.33 – Detailed view of AA 1100 matrix material with reinforcing NiTi ribbons. Taken with secondary electron SEM detector.

Figure 4.33 shows in more detail the NiTi ribbon interface. The whiter area in the interface is a depression resultant from the intensive surface polishing of two very dissimilar materials, promoting a convex edge at the faying interface. The image high range allows observing that the interface present no voids or cavities, whereas most common liquid state joining techniques would rather present more irregular microstructures at this range. The overall material embedment is good, although there is clear physical interface suggesting that there is no interdiffusion between materials.

Figure 4.34 shows the backscattering imaging of the same NiTi interface regions, although in this configuration it is not possible to observe surface topography, the clear images reveal the interface with increased image sharpness.
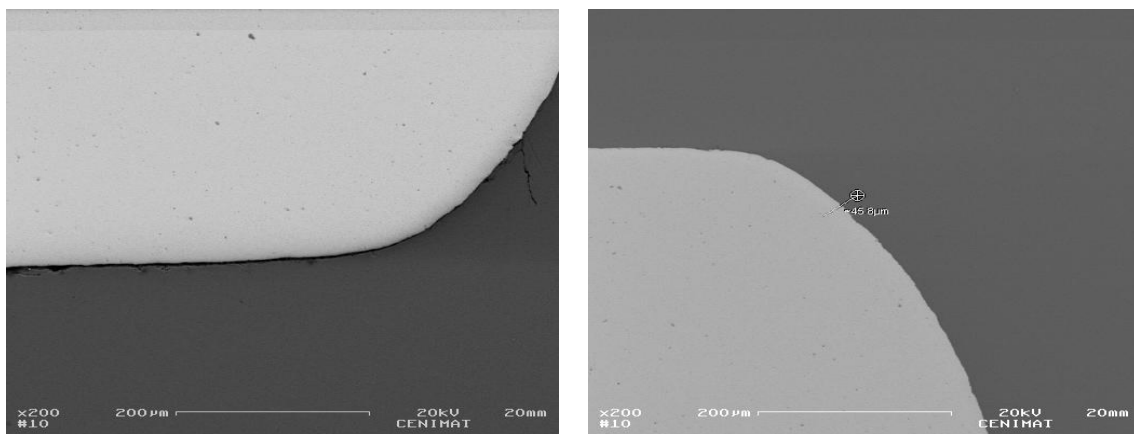
Figure 4.34 – Left – Unwelded region of NiTi reinforcing interface; Right – Welded interface between NiTi ribbon and AA 1100 matrix material. Both images from NiTi reinforced sample D10, taken with backscattering electron SEM detector.

The whiter regions are the heavier (atomic weight) NiTi reinforcements, the greyer areas depict the lighter aluminium alloy AA 1100 substrate and the black remnants (on the left backscattering image) represent lighter oxides or voids. The image on the left reveals the unwelded faying surfaces, and the occurrence of a crack in the rounded edge of the NiTi ribbon interface. On the right image it is possible to conclude that there are no voids greater than 2 μm (due to image maximum resolution) while it is not conclusive the presence of smaller voids; also, the substrate has completely embedded the NiTi interface.

An energy dispersive X-ray spectroscopy (EDS) was made on backscattered images of figure 4.34. The left unwelded matrix EDS analysis shows the expected high Al element concentration, due to the high Al grade (up to 99 % wt.) of the greyer region, see figure 4.35. Also, Ni and Ti elements were found, from the NiTi ribbon. On the other hand, no alloying elements of the AA 1100 were depicted, in part for its very low chemical composition ratio, and also to the maximum equipment EDS resolution.
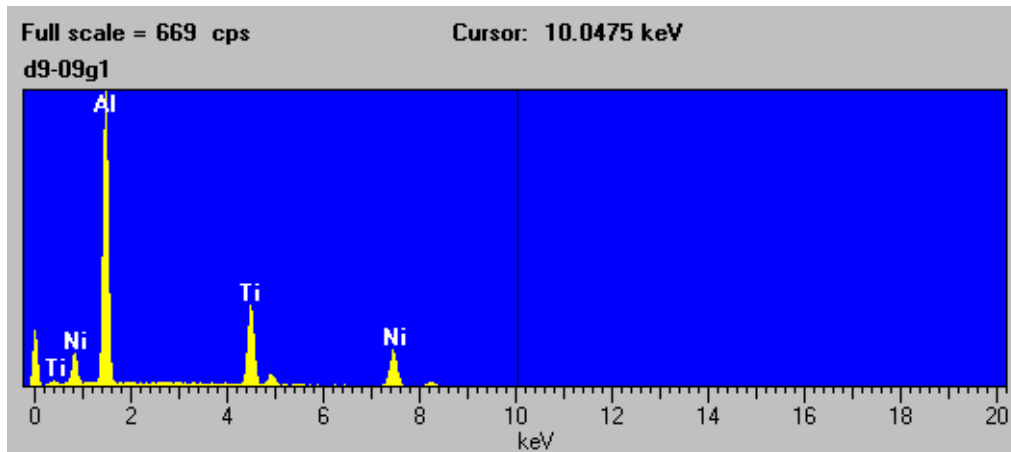
Figure 4.35 – EDS of NiTi reinforced AA 1100 matrix, of figure ZZ, left.

Due to the latter results, a linear scanning EDS analysis was made on the interface region. Figure 4.31 indicates the scanning line with about 45.8 μm length. Figure 4.36 shows the measured units (the results are depicted in the sum of appearances of each analysed element, from the total spectroscopic sweeps made in the predefined scanning line). Considering the starting point as the crossed line point, the charts bellow should be read from that point (in the substrate) to the final point (in the reinforcement).
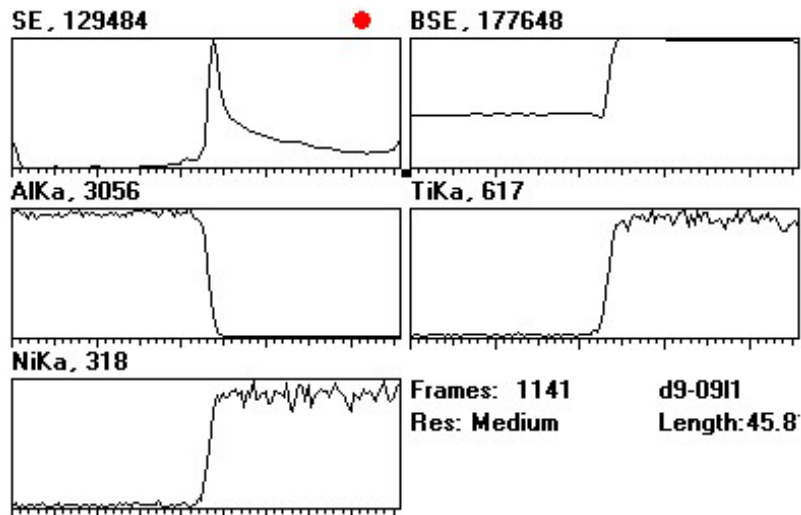
Figure 4.36 – EDS line scanning (of line illustrated in figure 4.34, right).

The secondary electrons (SE) chart shows a pronounced bulge, due to the depression resultant from the surface polishing. The backscattered energy chart indicates a change of the more electron absorber (lighter aluminium alloy) to the more shielded (heavier NiTi alloy), with an increased electron appearance awhile surpassing its interface. Moreover, it is possible to see that the diffusion area is no greater than about 3,5 μm in length, therefore being around the equipment spatial resolution. The Al, Ti and Ni distribution present the expected profiles for the interface without any diffusion triggered.

It is not possible to conclude about the interface chemical bonding; while mechanical bonding is evident in the observed SEM analysis, further analysis on the interface region after tensile testing evaluate the bonding mechanisms between NiTi reinforcing and matrix material.

The red region illustrates the interface region analysed in SEM, see figure 4.37. Figure 4.38 shows the deformed matrix material that was in contact with the NiTi ribbon during tensile testing.
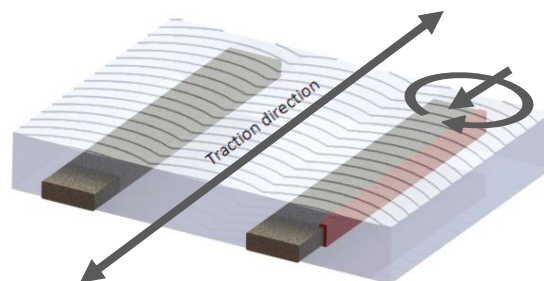
Figure 4.37 – Illustration of NiTi interface (red area) analysed in SEM, after tensile testing.

The uneven interface suggests that the mechanical bonding was promoted by simple mechanical locking, between the matrix and the interfaces, resulting from compressive forces of the faying surfaces. The fractography of the detailed retreating loop shows several characteristics: Smooth and faceted features (a) of the former contact made between the faying surfaces; flat reflecting surfaces of cleavage fractures in area (b); and, surface dimples of ductile fracture in (c). Concurrently, surface topography shows that (a) is the shallower area, followed by (b) and (c) – therefore, the deepest area (c) has the most ductile behavior, the opposite area (a) shows the most flattened brittle-like behavior.
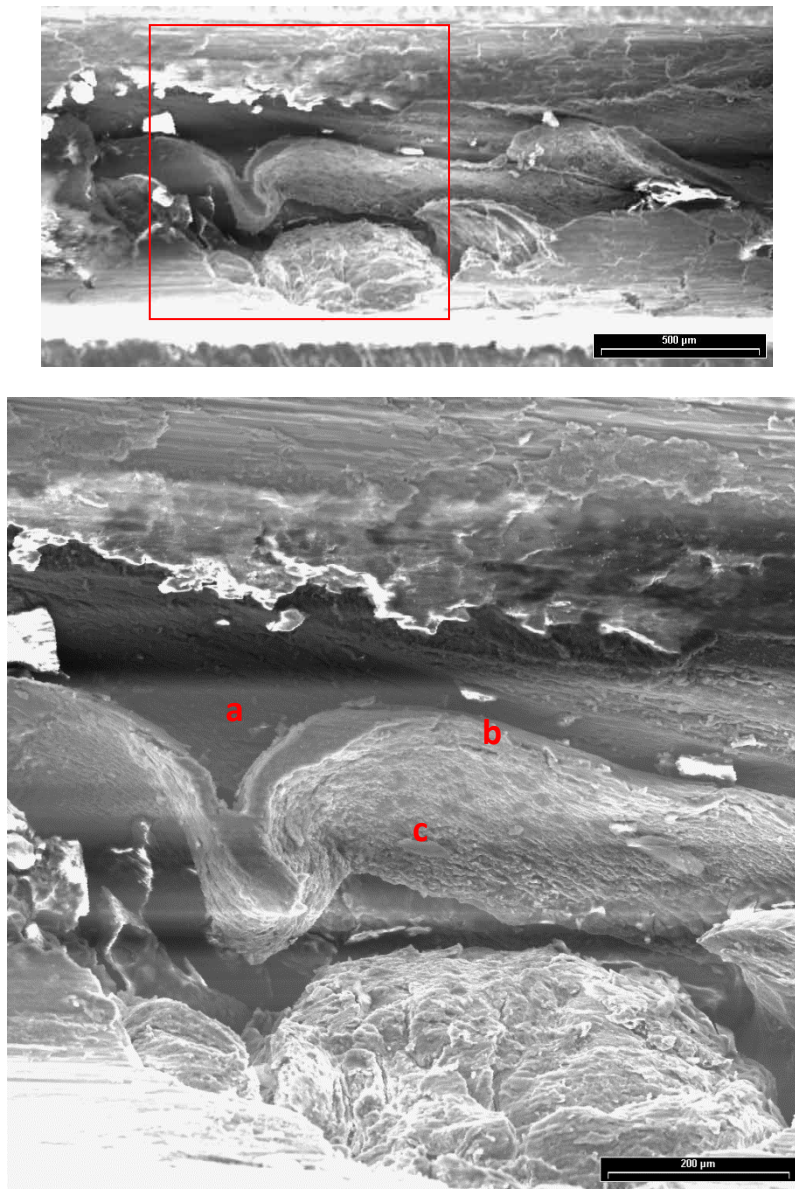
Figure 4.38 – General view and detail of the previous SEM image of a fracture surface in a longitudinal section of AA 1100 reinforced with NiTi ribbon.

SEM analysis of this fracture surface reveal different characteristics as material pullout, dimples and striation effects, as depicted in figure 4.39.

(1)	(2)
(3)	(4)
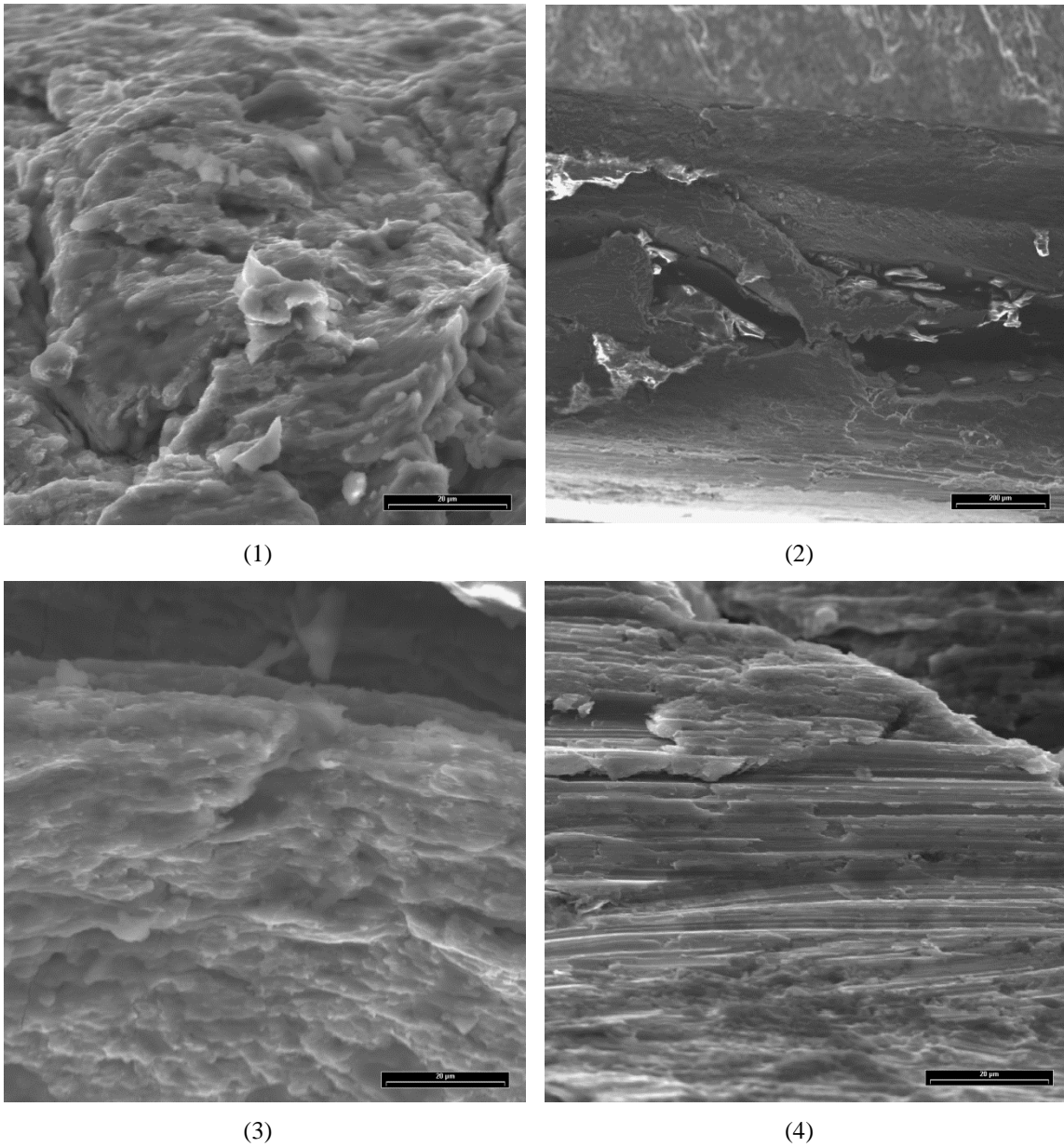
Figure 4.39 – SEM image of fractured surface, showing different features. 1) Cleavage fractures, from local load transfers; 2) Evidence of three-dimensional material flux in faying interfaces, pull effect reveals several brittle (mechanical locking) failures; 3) Characteristic dimples at the surface; 4) Striation marks of slipping between reinforcement and substrate surfaces.

Figure 4.40, shows a scanning linear EDS analysis made to one particle depicted in figure 4.36 (2). The linear scan shows mostly Al and a few traces of Ni, while Ti was not detected.

| Linear scan (Al) | Linear scan (Ni) | Linear scan (Ti) |
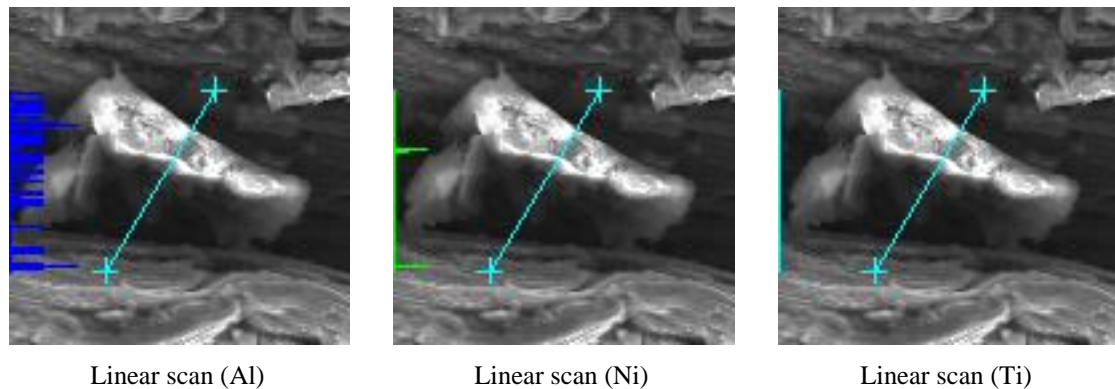
Figure 4.40 – EDS line scanning of particle depicted in figure 4.36 (2).

The latter results suggest that there is NiTi reinforcing remnants on the interface region, that can be related to two different agents: By pin shearing or intermetallic formations; by material friction, in tensile testing, between reinforcement and matrix, which ultimately led to particle detachment.

4.3.3.   Tensile testing

Figure 4.41 shows the aluminium lap joints after being tensile tested to rupture and the first sample (left side) was depicted to compare the initial length of the sample.

Specimens with reinforcing ribbons are grouped in figure 4.41 a), reinforced samples produced less elongation up to failure, compared to lap joints without reinforcing wires. Although there was reduced necking, the matrix aluminium material presented a typical ductile behavior, as figures 4.41 b) and c) show. NiTi ribbons presented no deformation and oxide free, as before FSW. With exception of the detailed sample in figures 4.41 b) and c), the remaining tensile tested samples initiated fracture on the overlapped side, with a 45 ° downward crack propagation direction, suggesting that the surface circular flow line depressions were responsible for crack propagation. Therefore, a machined surface would eliminate these crack propagation depressions and promote a different mechanical failure of the samples.

Figure 4.41 – Reinforced composites with NiTi ribbons; (a) overview of tested samples with NiTi reinforcements; (b) Top view of tensile failure (sample D3), (c) Back view of tensile failure (sample D3).

Sample geometry was adopted from the conventional prismatic samples used in standards, since there is no applicable specification for this type of materials. Thus, comparison between processed composites with added NiTi and bulk substrate aluminium alloy was difficult to perform.

Produced composites with NiTi reinforcements presented an increase of about 20 % in UTS, compared to non-reinforced FSW lap joints, and an increase of 70 % in UTS compared to base material in its as-received condition. Although there is a slight variation of stress tensile results, from 84 to 90 MPa, every sample produced with reinforcing material failed after the UTS of AA 1100 without reinforcement. Figure 4.42 shows the tensile tested curves.
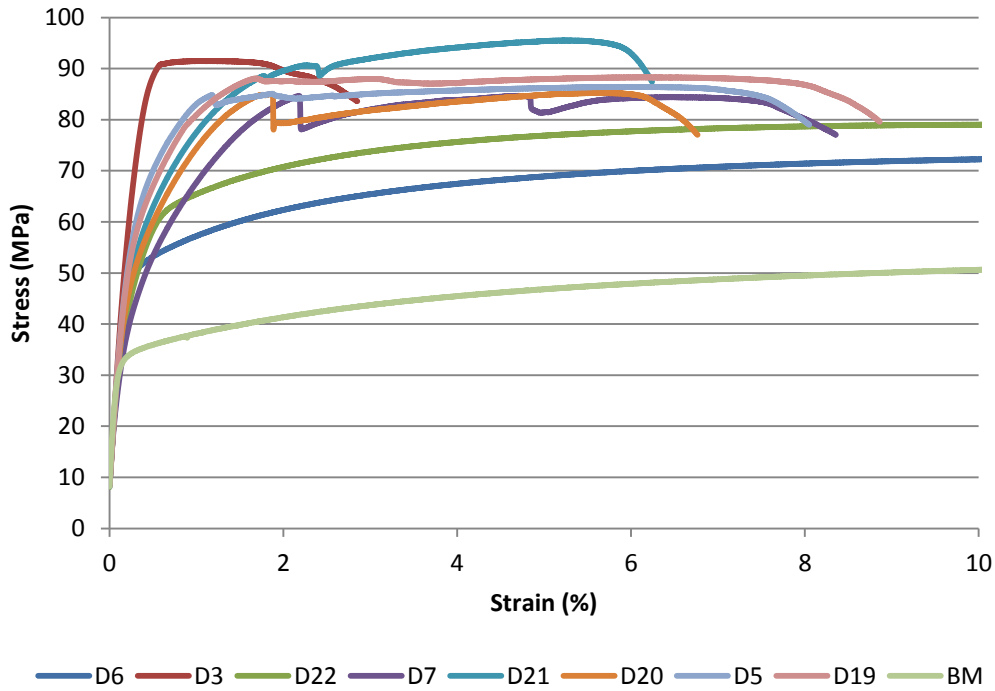
Figure 4.42 – Tensile testing stress-strain curves. D22 and D6, samples without reinforcements; BM –as-received base material; D3, D5, D7, D19, D20 and D21, samples with NiTi reinforcements.
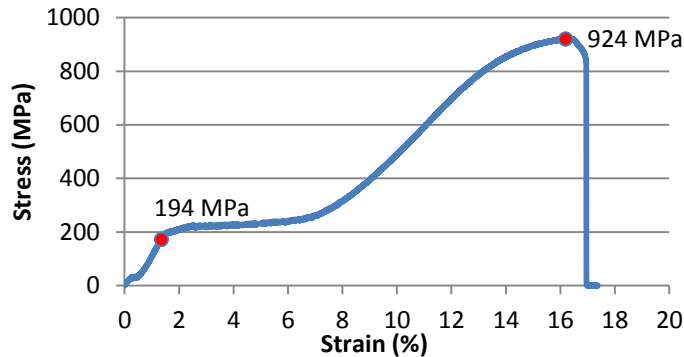
Figure 4.43 – NiTi stress-strain curve.

Sample D3 shows an increased elastic slope together with lower elongation to critical failure, compared to other samples. On the other hand, the remaining samples present a somewhat similar behavior: there are some distinguishable threshold levels (*e.g.* 2% strain for samples D7 and D20) suggesting that bellow 84 MPa of applied stress, the elastic strain of NiTi and the matrix was the same. Comparing figure 4.42 with the NiTi stress strain in figure 4.43 it can be seen that yielding of the composite is below the yield stress of NiTi in the martensitic reorientation plateau. However, a significant increase of the load is seen in the overall composite compared to the Al matrix.

4.3.4. Bending testing

Figure 4.44 shows the composite tested specimens. Both samples achieved maximum bent angle of 44 ° (figure 4.44 a), due to testing machine restrictions, without failure.

(a)

(b)

(c)
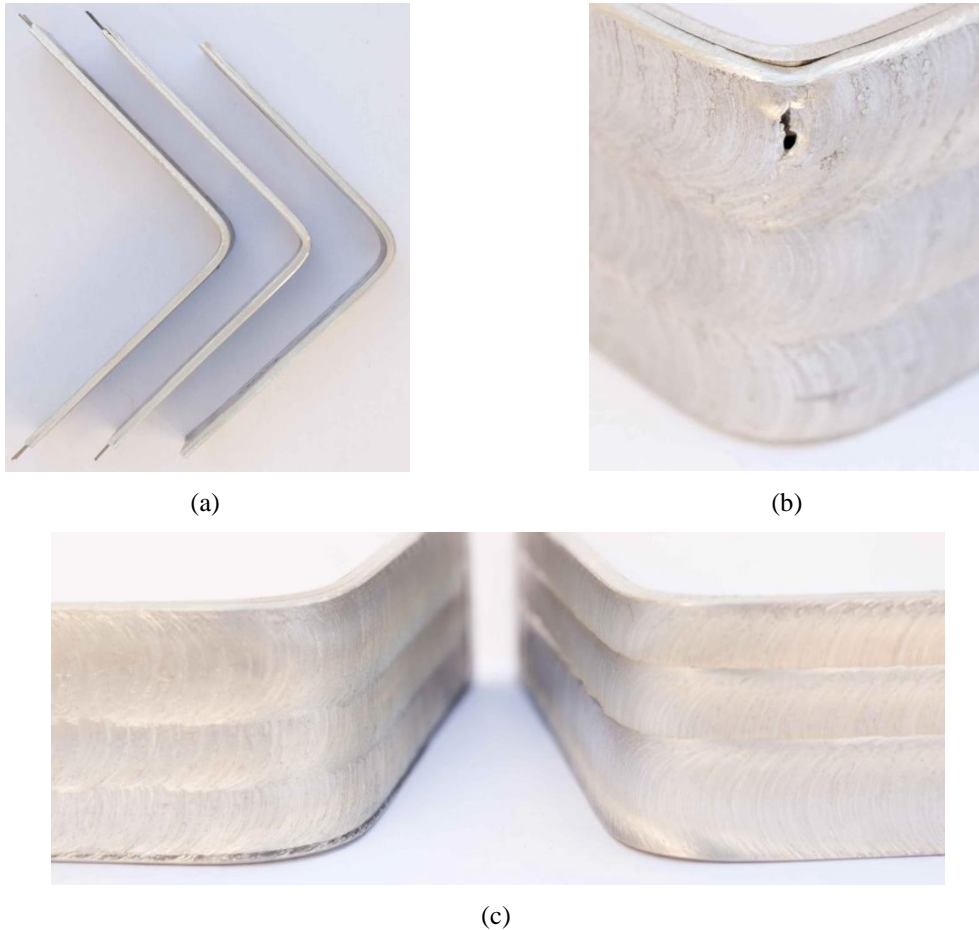
Figure 4.44 – Composites bending test samples; (a) general view of the bent samples at the maximum angle of 44 °, (b) detail view of sample D1 with a minor crack initiation, (c) close-up of the tensile solicited faces without rupture.

Bent samples reported no rupture, except a crack initiated in sample D1. That is, the matrix material has an excellent formability and elongation at a maximum allowable angle of 44 °. Further testing up to 90 ° of bending angle also did not produce any superficial material rupture.

Different behaviors are observed in each type of composite. Samples with NiTi reinforcing ribbons show a 5 to 40 % increase of load supporting (figure 4.45). While wire reinforced composites depict almost no force increment, it was studied a volume fraction ratio of 2.1 % in wire steel reinforced samples and 5.25 % in NiTi ribbon reinforced samples,

therefore, the greater NiTi volume fraction promoted increased stiffness, on the final composites.

NiTi reinforced overall increased stiffness suggests that interface bonding between matrix and reinforcement can cope with shear stress, resulting from flexure load. NiTi ribbons presented no slipping after bending tests.
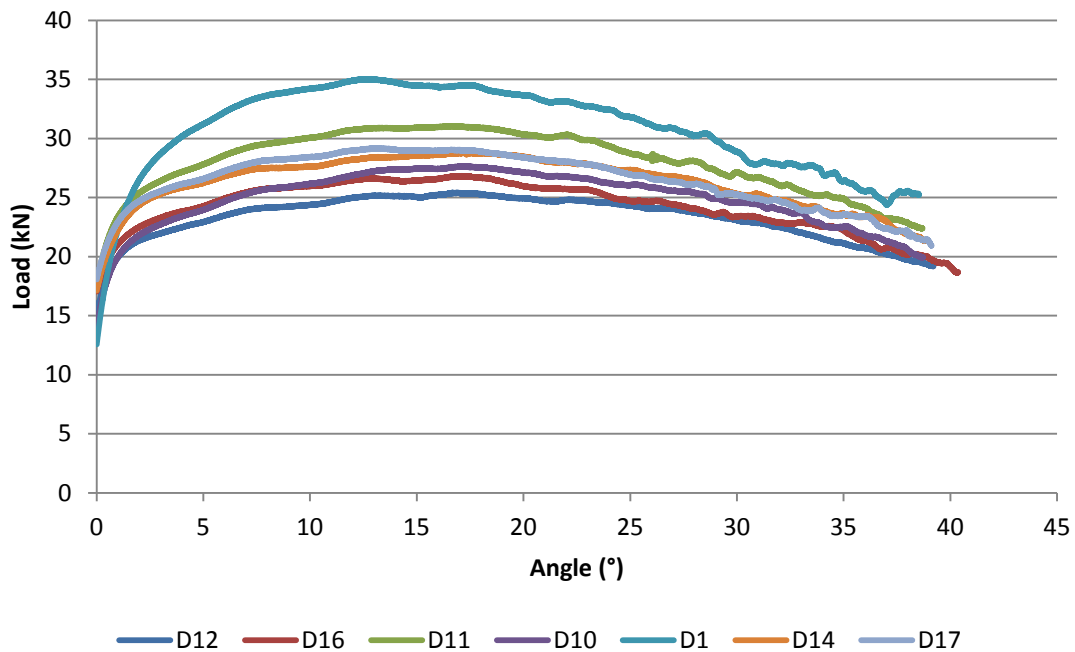
Figure 4.45 – Resulting load-angle curves for bending tested samples. D14 and D12 without reinforcements; D17 and D16 with steel wire; D1, D11 and D10 with NiTi reinforcements.

4.3.5. Vibration testing

Several samples were tested for two different vibration modes, natural frequency and logarithmic decrement. The former, uses the first natural frequency response measured with a piezoelectric accelerometer and compares to different samples. In the second, the frequency energy absorption is plotted as a function of time and the reduction factor is determined to characterize material damping properties and determine its damping ratio.

Annex B gathers measured amplitudes of samples natural frequencies, although only first natural frequency values were considered in this investigation. Natural frequency variation is a major factor for system resonance in forced vibration systems (equation 4.1) the capability to actively avoid resonance was studied by changing composite's natural frequency. When

system forced vibrations equals its natural frequency (equation 4.2) a destructive resonance phenomena is achieved, which, without any damping, may lead to service failure [79].

$$\omega_n = \sqrt{\frac{k}{m}} \tag{4.1}$$

$$\frac{\omega_f}{\omega_n} = 1 \tag{4.2}$$

Where ω_n is material natural frequency (rad/s), ω_f is system forced frequency (rad/s), k is stiffness (GPa) and m is mass (kg). Table 4.3 presents the calculated average of first natural frequencies measured, at different conditions. There was no frequency change between NiTi reinforced composite (D9) and non-reinforced sample (D13) at ambient temperature, although there is a mass increase; therefore, overall composite stiffness have also changed, due to equal natural frequencies.

After liquid nitrogen cooling, the average first natural frequencies of NiTi reinforced AA 11000 have increased by 8% while samples without reinforcement remained constant. After reheated, the NiTi reinforced composite first natural frequencies returned to its former values.

Table 4.3 – Natural frequency of samples tested at four different external conditions.

Sample	Ambient temperature (rad/s)	Cooled with liquid nitrogen (1min) (rad/s)	Cooled with liquid nitrogen (5min) (rad/s)	Reheated (rad/s)	Weight mass (kg)
D9	53	57	57	53	0.54
D13	53	54	53	–	0.51
D15	49	–	–	–	0.53

The latter results led to conclude that the same composite can alter its natural frequency, triggered by external conditions (such as temperature), therefore avoiding resonance modes by changing its natural frequency, the latter intrinsic to the composite stiffness.

Although the probable causes of composite stiffness changing are not thoroughly known, it must be noticed that both materials (reinforcing and matrix) used in this investigation have very dissimilar thermo-physical properties, such as coefficient of thermal expansion. On the other hand, none of the tested materials present a temperature transition curve. Therefore, it can be concluded that mismatching of thermal expansion coefficients was responsible for this composite stiffness changing – as different material thermal responses (induced by liquid nitrogen cooling) would modify bonding stresses between matrix and reinforcements, therefore changing the overall composite response to induced applied stresses (or induced vibrations).

Material damping response was also studied and table 4.4 presents damping curves and logarithmic decrements of composites D9, D13 and D15.

Table 4.4 – Material vibration response to initial impulse, a) D9; b) D13 and c) D15

a)
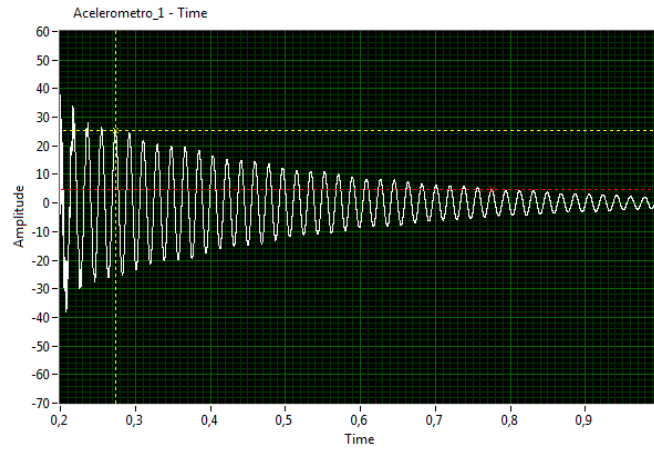
b)
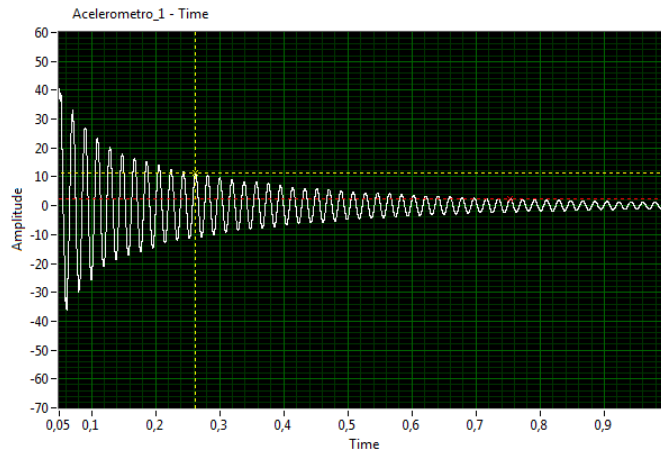
c)
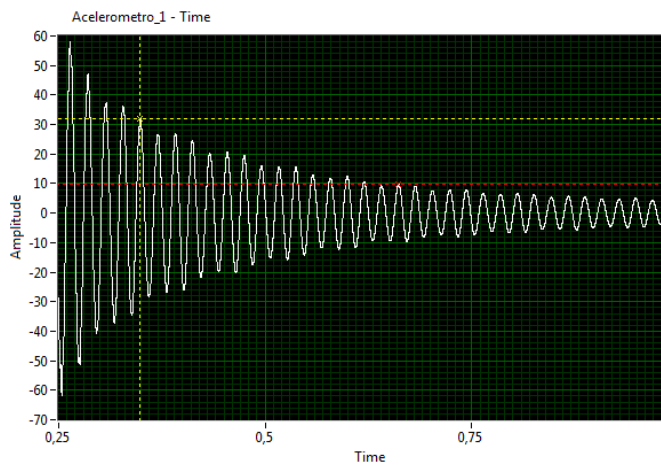
Logarithmic decrement, δ in equation 4.3, represents the rate at which the amplitude of a free damped vibration decreases. It is defined as the natural logarithm of the quotient between any two successive amplitudes x_i and x_{i+m}, where m is the number of cycles apart from amplitudes. Damping ratio, ζ in equation 4.4, is used to characterize and compare damping capacity of a material, in high damping systems this value exceeds the unit, in low damping systems it changes from zero to one, undamped systems have zero damping ratio [79].

$$\delta = \frac{1}{m} \cdot \ln\left(\frac{x_i}{x_{m+i}}\right) \tag{4.3}$$

$$\zeta = \frac{\delta}{\sqrt{(2\pi)^2 + \delta^2}} \tag{4.4}$$

As table 4.5 shows, samples with reinforcements (NiTi ribbons – D9 and steel wires – D15) have higher damping ratio than without reinforcements. This internal damping is provided by NiTi ribbons and the interface with the matrix since Al has no evident damping capacity.

Table 4.5 – Logarithmic decrement and damping ratio.

Sample	cycles	x	x_{i+m}	δ	ζ
D9	27	25.4738	4.7171	0.6246	0.0099
D13	26	11.3018	2.3853	0.5983	0.0095
D15	15	31.9983	9.8288	0.7869	0.0125

The increased internal friction increases material dampness and recover rates from induced vibrations. Several crystallographic structures are responsible for promoting internal material friction: Dislocations, precipitates, incongruous crystal structures, are the most common friction-inducing mechanisms – the increased material stress, due to the latter crystallographic properties, converts vibratory mechanical energy into frictional heat and metal thermal conductivity dissipates it outwards.

The presence of very dissimilar materials and material interfaces inside enhance its mechanical friction, therefore reducing its vibratory response. Stiffer NiTi alloy, in hardened austenitic phase, has lower internal friction mechanisms than the more ductile AA 1100 matrix material. On the other hand, the presence of a physical interface between them increases composite's internal friction and damping ratio. Steel wire reinforced composites outputted the highest damping ratio, although results between composites cannot be compared.

Measured damping ratios enables to characterize the composites as underdamped systems. It would be interesting to study the impact of a HIDAMET material, such as

superelastic NiTi alloys, with higher volume fraction ratios, to understand the composites mechanical response and dampness from induced vibrations.

4.3.6. Eddy currents testing

Eddy currents inspection was made on several samples with and without reinforcements. Two different characterizations were made: first, the impact of overlapping regions and reinforcing materials; secondly, to measure composite electrical conductivity, after FSW.

Results from preliminary tests, of normalized electrical impedance, in samples with and without reinforcements, are depicted in figure 4.46.

The results, above presented, refer to the absolute component of electrical impedance and were normalized for comparison purposes.

Samples D9 and D15, of figure 4.46, enables to identify two different zones: one, where processed aluminium alloy matrices high conductivity presents an almost zero normalized value, therefore no major field disturbances; the other, where protuberances in the above charts depict the impact of the dissimilar materials. The disturbed electromagnetic field can be detected at 10 KHz testing frequency, indicating the presence of the reinforcements by least at 0.82 mm, according to penetration depth (equation 3.2).

NiTi ribbons and austenitic steel wires output the same results, with few differences amongst them. Both are non ferromagnetic materials, therefore with a magnetic permeability comparable to air. Such a low magnetic permeability does not create a magnetic induced field; concurrently, the low electrical conductivity allows distinguishing between eddy current fields of matrix AA 1100 material and reinforcing materials.

Sample D9 absolute impedance increment is greater than the increased impedance in steel, suggesting that different cross section areas – NiTi ribbons have an area five times of the steel wires – and electrical conductivities, of the reinforcing materials, promote different eddy current induced fields.
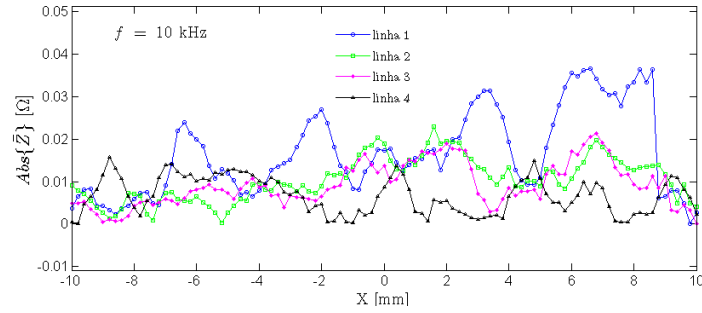
Sample D13 without reinforcements
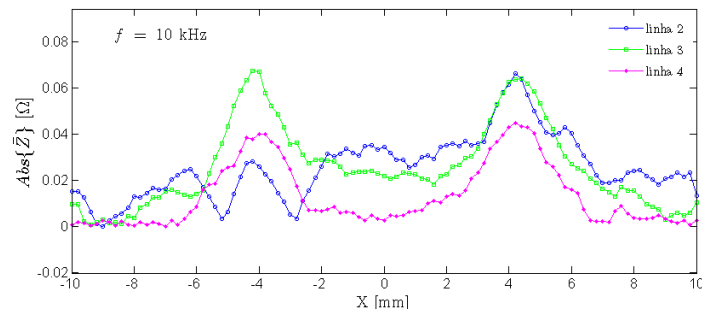
Sample D15 with steel reinforcements
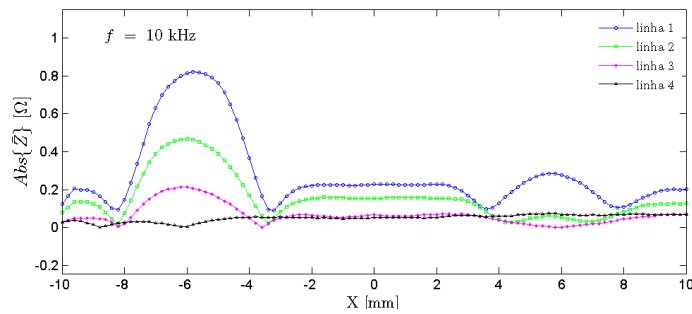
Sample D9 with NiTi reinforcements

Figure 4.46 – Eddy current inspection of samples D13, D15 and D9 at 10 KHz.

Dissimilarity between matrix and reinforcing materials is such that the latter overshadows the former material properties (*e.g.* material characteristic HAZ, TMAZ and SZ). Material electrical and thermal conductivity depends on the electronic mobility, on the crystalline structure of existing phase, and crystal defect content. In order to perform an eddy current analysis solely on the weld bead, the effect of dissimilar reinforcements can be avoided by reducing induced current penetration depth, according to equation 3.2.

As preliminary tests suggested, the increasing frequency increased material skin effect, up to a point where no reinforcing material was detected on the impedance charts. The aluminium alloy high conductivity largely reduces the penetration depth within the part − as

equation 3.2 suggests. Figure 4.47 shows the normalized impedance charts plotted at different frequencies; line 4 (of sample D9) suggests that at 100 KHz the electromagnetic increased skin effect was sufficient to avoid the NiTi ribbons, deeper lines (1,2 and 3) can detect the reinforcements at any given frequency, up to 100 KHz. It is also noticeable the non symmetry of the plotted values, two factors may influence this: The fact that there is no parallelism between the milled smooth surfaces and the NiTi ribbons; the NiTi ribbons in fact changed position (or height in this case) during the composite processing.
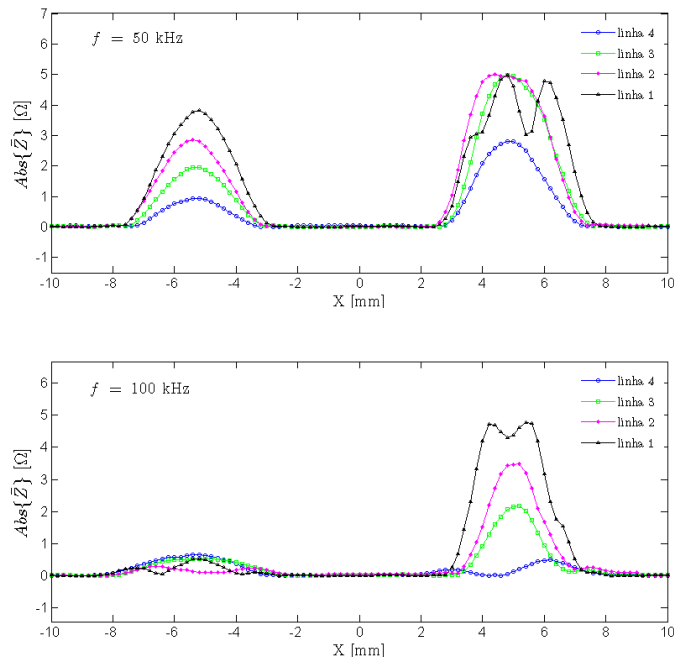
Figure 4.47 – Normalized absolute impedance values of sample D9 electromagnetic tested at 50 KHz and 100 KHz.

Annex C gathers further information, in normalized absolute impedance charts, at different steps and frequencies.

Electrical conductivity

In sample D9, electrical conductivity measurements were made on differently affected areas, at four given depths. The starting measurements were obtained on the tested samples BM and as-received material samples; table 4.6 gathers electrical conductivity measurements in IACS.

Table 4.6 – Electrical conductivity measured values in IACS (%).

	Outside	Above Reinforcement 1	Middle	Above Reinforcement 2	BM
Test 1	63.19	62.85	62.59	62.59	65.00
Test 2	63.10	61.99	62.67	62.59	64.93
Test 3	62.47	61.82	62.67	63.28	64.78
Test 4	62.42	62.42	62.94	62.85	65.20
Average	**62.80**	**62.27**	**62.72**	**62.84**	**64.98**

Table 4.6 shows no significant alteration in electrical conductivity, between different positions above the weld beads. On the other hand, there is about 4 % IACS electrical conductivity reduction between BM and the processed regions. Since material electrical conductivity is also related by the total length of grain boundaries per unit area, it is expectable that the heat exposure of the high purity Al alloy instigated grain coalescence. The latter conclusions should be addressed in further investigation.

The resulting relative electrical conductivity shows that even after severe plastic deformation, the overall composite's electrical properties are very good, with an average of 65 % IACS, which is the same standard value given for the AA 1100 bulk material.

4.3.7. Summary conclusions

- FSW technology is viable for the production of composites with very dissimilar embedded materials (the overall strength increased is not sufficient for structural applications).

- Very formable matrix material produced a bonding with better mechanical properties than the base material, thus, for a functional material (*e.g.* NiTi alloys) this may be a particular interesting condition.

- The final bonding strength is heavily related to the interface roughness of the material, this interface may be mechanically strengthened by joining a very rough hard material into a very formable matrix.

- The active response of material was tested in temperature change. Results reflected a change in material vibration response, although additional investigation is required. It can be concluded that reinforced composites produced different vibration responses, compared to non-reinforced composites. The former response changes could be related to thermal expansion material mismatch, since the processed matrix aluminium alloy

without reinforcements produced no change after several testing at liquid nitrogen temperature.

- Friction stir welded AA 1100 has shown great electrical conductivity, although heat treated base material presented higher conductivity. After FSW the lap-jointed AA 1100 shows a electrical conductivity reduction bellow 3 % IACS.

- The depicted results show that the electrical conductivity measurement can accurately identify a local variation corresponding to the reinforcing material. The signal intensity is proportional to the cross-section area under inspection and allows distinguishing between high and low conductivity materials.

5. CONCLUSIONS AND SUGGESTIONS FOR FUTURE WORK

This investigation aimed at producing and characterizing composites consisting of two very distinctive materials, by friction stir welding. The materials used were AA 1100, a soft, formable and light alloy with excellent electrical conductivity, and NiTi shape memory alloy, with excellent functional properties. From this study, the following can be concluded:

- FSW proved to be viable to produce Al/NiTi composites in a lap joint configuration where the NiTi ribbons were mechanically bonded to the Al matrix.

- A good embedment of the NiTi was achieved by the intensively deformed matrix aluminium. This interface was subjected to high compressive forces, resulting from the stirred material flow of the FSW process.

- NiTi reinforced composites showed an increase of about 20 % in ultimate tensile strength, compared to the non-reinforced FSW lap joints, and an increase of 70 % in UTS compared to Al alloy base material in as-received condition.

- Under tensile loads, the composite failed at the bonding interfaces at higher yielding stresses than the lap joints in AA 1100 without reinforcements, which is significant if the functionality, of the composite, is to be assessed.

- Samples with NiTi reinforcing showed an increase of up to 40 % of bending load, compared to Al base material.

- Characterization in terms of material frequency vibration resulted in an increase of 8% by changing the material stiffness upon cooling. The composite can alter its natural frequency, triggered by external conditions (such as temperature), therefore being capable to avoid resonance modes.

- NiTi was not seen to affect the electrical conductivity under the conditions tested, bulk AA 1100 has shown great electrical conductivity, although heat treated base material presented higher conductivity. After friction stir welding the lap-jointed AA 1100 showed an electrical conductivity reduction bellow 3 % IACS.

This was a pioneer work of using friction stir welding to manufacture such a composite and further research is required to fully exploit the technology and assess potential industrial applications of the material.

Suggestions for future work are:

- Different pre-processing groove opening techniques should be studied; the last used forming technique produced very homogeneous and repeatable grooves, although the final composites have shown some unparallel ribbon reinforcements.

- Concerning the AA 1100 lap-joint sound weld width, a further investigation should address different tool geometries; the study of tool influenced material flow into lap joint configuration is yet to be explored; also, an optimization matrix should be designed to study the parameter relation to the jointed faying surfaces – the latter was already started in this investigation.

- Different reinforcing geometries and parameters produced very different and characteristic material flows around them, that lacks of more research. Three-dimensional material flow, in the presence of obstructing shearing objects, and the wake formation purported very interesting results, although more investigation is required to extrapolate any viable conclusions.

- This investigation focused solely on AA 1xxx very formable series; notwithstanding, the prospect of creating structural smart composites with different aluminium alloys (structural aluminiums such as 2xxx series) is reasonable. Base material selection is also an important factor considering final composite desired properties.

- As far as damping capacity of the composite is concerned results are not conclusive and further work is required in this field, namely, testing different volume fraction ratios of NiTi shape memory alloys.

6. REFERENCES

[1] K. K. Chawla, *Composite Materials - Science and Engineering*, (1987), Springer-Verlag, New York.

[2] D. D. L. Chung, *Composite materials: functional materials for modern technologies*, (2003), Springer-Verlag, London.

[3] D. Gay, *Matériaux composites*, (1997), Hermès, Paris.

[4] T. A. Grandline, "Surface modeling for composite materials" in *SIAG GD* (2012), The Boeing Company, Seattle.

[5] M. M. Schwartz, *Joining of composite-matrix materials*, (1994), ASM International, Ohio.

[6] C. A. Frysz, X. P. Shui, and D. D. L. Chung, "Use of carbon filaments in place of carbon black as the current collector of a lithium cell with a thionyl chloride bromine chloride catholyte" *Journal of Power Sources*, (1996), 58, 111-123.

[7] George E. Dieter, *Vol 20 - Materials Selection and Design*, (1997), ASM International, USA.

[8] F. Bordeaux and R. Yavari, "Multiple necking and deformation-behavior of multilayer composites prepared by cold-rolling", *Zeitschrift Fur Metallkunde*, (1990), 81, 130-135.

[9] C. Schoene and E. Scala, "Multiple necking phenomena in metal composites", *Metallurgical Transactions*, (1970), 1, 3466-3470.

[10] R. M. Vennett, S. M. Wolf, and A. P. Levitt, "Multiple necking of tungsten fibers in a brass-tungsten composite", *Metallurgical Transactions*, (1970), 1, 6, 1569-1576.

[11] Rafael Nunes, *Vol 2 - Properties and Selection Nonferrous Alloys and Special- Purpose Materials*, (1990), ASM International, USA.

[12] M. Dixit, J. W. Newkirk, and R. S. Mishra, "Properties of friction stir-processed Al1100-NiTi composite", *Scripta Materialia*, (2007), 56, 541-544.

[13] J. W. D. Callister, *Materials Science and engineering - an introduction, 5th edition*, (1999), John Wiley & Sons, Inc., USA.

[14] A. S. Paula, K. K. Mahesh, C. M. L. dos Santos, J. P. H. G. Canejo, and F. M. B. Fernandes, "One- and two-step phase transformation in Ti-rich NiTi shape memory alloy", *International Journal of Applied Electromagnetics and Mechanics*, (2006), 23, 25-32.

[15] H. Tobushi, E. A. Pieczyska, W. K. Nowacki, T. Sakuragi, and Y. Sugimoto, "Torsional deformation and rotary driving characteristics of SMA thin strip", *Archives of Mechanics*, (2009), 61, 241-257.

[16] Hugh Baker, *Vol3 - Alloy phase diagrams*, (1992), ASM International, USA.

[17] K. M., *Shape memory microactuators*, (2004), Springer-Verlag, Germany.

[18] I. G. Ritchie and Z. L. Pan, "High-damping metals and alloys", *Metallurgical Transactions a-Physical Metallurgy and Materials Science*, (1991), 22, 607-616.

[19] H. C. Lin, S. K. Wu, and M. T. Yeh, "Damping characteristics of TiNi shape-memory alloys", *Metallurgical Transactions a-Physical Metallurgy and Materials Science*, (1993), 24, 2189-2194.

[20] K. Otsuka, *Shape memory materials*, (1999), Cambridge University press, United-Kingdom.

[21] F. Gandhi and G. Chapuis, "Passive damping augmentation of a vibrating beam using pseudoelastic shape memory alloy wires", *Journal of Sound and Vibration*, (2002), 250, 519-539.

[22] B. F. Keats, R. R. Mansour, and R. B. Gorbet, "Shape memory alloy temperature compensation for resonators", *Ieee Mtt-S International Microwave Symposium Digest*, (2003), 1, 3, 1259-1262.

[23] K. Nagaya, S. Takeda, Y. Tsukui, and T. Kumaido, "Active control method for passing through critical speeds of rotating shafts by changing stiffnesses of the supports with use of memory metals", *Journal of Sound and Vibration*, (1987), 113, 307-315.

[24] B. London, J. Fino, A. Pelton, C. Fuller, and M. Mahoney, "Friction stir processing of nitinol" *Friction Stir Welding Processing III*, (2005), 1, 67-74.

[25] R. M. Miranda, M. F. Braz Fernandes, C. M. Cracieunescu, L. Quintino, and L. Alberty Vieira, "Shape memory alloys: existing and emerging applications", *Advances in materials science research*, (2011), 6, 243-265.

[26] Memory Metalle GmbH, *www.memory-metalle.de/html/03_knowhow/03_faq_list.as*, (2012).

[27] J. M. Chiou and D. D. L. Chung, "Improvement of the temperature resistance of aluminium-matrix composites using an acid phosphate binder", *Journal of Materials Science,* (1993), 28, 1471-1487.

[28] J. A. Cornie, Y. M. Chiang, D. R. Uhlmann, A. Mortensen, and J. M. Collins, "Processing of metal and ceramic matrix composites", *American Ceramic Society Bulletin,* (1986), 65, 2, 293-304.

[29] M. G. Nicholas and R. M. Crispin, "diffusion bonding stainless-steel to alumina using aluminium interlayers", *Journal of Materials Science,* (1982), 17, 3347-3360.

[30] I. A. Ibrahim, F. A. Mohamed, and E. J. Lavernia, "Particulate reinforced metal matrix composites – a review", *Journal of Materials Science,* (1991), 26, 1137-1156.

[31] E. J. Young, E. Mateeva, J. J. Moore, B. Mishra, and M. Loch, "Low pressure plasma spray coatings", *Thin Solid Films,*(2000), 377, 788-792.

[32] C. J. Dawes and W. M. Thomas, "Friction stir process welds aluminum alloys", *Welding Journal,* (1996), 75, 41-45.

[33] T. WM, UK Patent PCT/GB92/02203, (1991).

[34] R. S. Mishra and Z. Y. Ma, "Friction stir welding and processing", *Materials Science & Engineering R-Reports,*(2005), 50, 1-78.

[35] L. Fratini and V. Corona, "Friction stir welding lap joint resistance optimization through gradient techniques", *Journal of Manufacturing Science and Engineering-Transactions of the Asme,* (2007), 129, 6, 985-990.

[36] P. Asadi, G. Faraji, A. Masoumi, and M. K. B. Givi, "Experimental Investigation of Magnesium-Base Nanocomposite Produced by Friction Stir Processing: Effects of Particle Types and Number of Friction Stir Processing Passes", *Metallurgical and Materials Transactions a-Physical Metallurgy and Materials Science,* (2011), 42A, 2820-2832.

[37] A. P. Reynolds, "Visualisation of material flow in autogenous friction stir welds", *Science and Technology of Welding and Joining,* (2000), 5, 120-124.

[38] R. Leal and A. Loureiro, "Defects formation in friction stir welding of aluminium alloys", *Advanced Materials Forum Ii,* (2004), 455-456, 299-302.

[39] P. Asadi, G. Faraji, and M. K. Besharati, "Producing of AZ91/SiC composite by friction stir processing (FSP)", *International Journal of Advanced Manufacturing Technology,* (2010), 51, 247-260.

[40] K. Kimapong and T. Watanabe, "Effect of welding process parameters on mechanical property of FSW lap joint between aluminum alloy and steel", *Materials Transactions,* (2005), 46, 2211-2217.

[41] M. K. Yadava, R. S. Mishra, Y. L. Chen, B. Carlson, and G. J. Grant, "Study of friction stir joining of thin aluminium sheets in lap joint configuration", *Science and Technology of Welding and Joining,* (2010), 15, 70-75.

[42] R. Rai, A. De, H. Bhadeshia, and T. DebRoy, "Review: friction stir welding tools", *Science and Technology of Welding and Joining,* (2011), 16, 325-342.

[43] R. Nandan, T. DebRoy, and H. Bhadeshia, "Recent advances in friction-stir welding - Process, weldment structure and properties", *Progress in Materials Science,* (2008), 53, 980-1023.

[44] S. Hirasawa, H. Badarinarayan, K. Okamoto, T. Tomimura, and T. Kawanami, "Analysis of effect of tool geometry on plastic flow during friction stir spot welding using particle method", *Journal of Materials Processing Technology,* (2010), 210, 11, 1455-1463.

[45] S. M. Chowdhury, D. L. Chen, S. D. Bhole, and X. Cao, "Tensile properties of a friction stir welded magnesium alloy: Effect of pin tool thread orientation and weld pitch", *Materials Science and Engineering a-Structural Materials Properties Microstructure and Processing,* (2010), 527, 21, 6064-6075.

[46] H. Fujii, L. Cui, M. Maeda, and K. Nogi, "Effect of tool shape on mechanical properties and microstructure of friction stir welded aluminum alloys", *Materials Science and Engineering a-Structural Materials Properties Microstructure and Processing,* (2006), 419, 25-31.

[47] Y. H. Zhao, S. B. Lin, L. Wu, and F. X. Qu, "The, influence of pin geometry on bonding and mechanical properties in friction stir weld 2014 Al alloy", *Materials Letters,* (2005), 59, 2948-2952.

[48] M. Whitakker, "Record Copper Prices Prompt Switch to Aluminum", *The Wall Street Journal*, (2012), Mar. 17.

[49] J. Q. Su, T. W. Nelson, R. Mishra, and M. Mahoney, "Microstructural investigation friction stir welded 7050-T651 aluminium", *Acta Materialia,*(2003), 51, 713-729.

100

[50]   R. S. Mishra, Z. Y. Ma, and I. Charit, "Friction stir processing: a novel technique for fabrication of surface composite", *Materials Science and Engineering a-Structural Materials Properties Microstructure and Processing,* (2003), 341, 307-310.

[51]   P. L. Threadgill, A. J. Leonard, H. R. Shercliff, and P. J. Withers, "Friction stir welding of aluminium alloys", *International Materials Reviews,* (2009), 54, 49-93.

[52]   F. Nascimento, T. Santos, P. Vilaca, R. M. Miranda, and L. Quintino, "Microstructural modification and ductility enhancement of surfaces modified by FSP in aluminium alloys", *Materials Science and Engineering a-Structural Materials Properties Microstructure and Processing,* (2009), 506, 16-22.

[53]   A. Kurt, I. Uygur, and E. Cete, "Surface modification of aluminium by friction stir processing", *Journal of Materials Processing Technology,* (2011), 211, 313-317.

[54]   A. Elrefaey, M. Gouda, M. Takahashi, and K. Ikeuchi, "Characterization of aluminum/steel lap joint by friction stir welding", *Journal of Materials Engineering and Performance,* (2005), 14, 10-17.

[55]   S. W. Stratton, *Circular of the bureau of strandards - copper wire table*, (1914), Washington government printing office, Washington.

[56]   S. Yazdanian and Z. W. Chen, "Effect of friction stir lap welding conditions on joint strength of aluminium alloy 6060", in *Conference on Processing, Microstructure and Performance of Materials*, (2009), 012021, Auckland, New Zealand.

[57]   V. Soundararajan, E. Yarrapareddy, and R. Kovacevic, "Investigation of the friction stir lap welding of aluminum alloys AA 5182 and AA 6022", *Journal of Materials Engineering and Performance,* (2007), 16, 477-484.

[58]   G. Buffa, G. Campanile, L. Fratini, and A. Prisco, "Friction stir welding of lap joints: Influence of process parameters on the metallurgical and mechanical properties", *Materials Science and Engineering a-Structural Materials Properties Microstructure and Processing,* (2009), 519, 19-26.

[59]   Y.-h. Chen, Q. Ni, and L.-m. Ke, "Interface characteristic of friction stir welding lap joints of Ti/Al dissimilar alloys", *Transactions of Nonferrous Metals Society of China,* (2012), 22,   299-304.

[60]   L. Cederqvist and A. R. Reynolds, "Factors affecting the properties of friction stir welded aluminum lap joints", *Welding Journal,* (2001), 80, 12, 281-287.

[61]   M. Ericsson and R. Sandstrom, "Fatigue crack propagation in friction stir welded and parent AA6082", *Steel Research International,* (2006), 77, 450-455.

[62]   M. Ericsson, L. Z. Jin, and R. Sandstrom, "Fatigue properties of friction stir overlap welds", *International Journal of Fatigue,* (2007), 29, 57-68.

[63]   M. K. Kulekci, A. Sik, and E. Kaluc, "Effects of tool rotation and pin diameter on fatigue properties of friction stir welded lap joints", *International Journal of Advanced Manufacturing Technology,* (2008), 36, 877-882.

[64]   D. Fersini and A. Pirondi, "Fatigue behaviour of Al2024-T3 friction stir welded lap joints", *Engineering Fracture Mechanics,* (2007), 74, 468-480.

[65]   R. Leal and A. Loureiro, "Defects formation in friction stir welding of aluminium alloys", *Advanced Materials Forum Ii,* (2004), 455-456, 299-302.

[66]   Matweb, *matweb.com/search/DataSheet.aspx?MatGUID=db0307742df14c8f817bd8d62207368e*, (2012).

[67]   ESAB, *http://products.esab.com/Templates/T041.asp?id=114404*, (2012).

[68]   ESAB, *LEGIO FSW 3U friction stir welding machine - technical description manual*, (2005), ESAB, United-Kingdom.

[69]   P. Vilaça, T. Santos, PT Patent PT104072, (2008).

[70]   T. Santos, *Ferramenta modular ajustável e refrigerada para soldadura e processamento por fricção linear*, (2008), Universidade Técnica de Lisboa, Lisbon.

[71]   F. M. Nascimento, "Processamento por fricção linear - caracterização e análise de ligas de alumínio processadas", (2007), Universidade Técnica de Lisboa, Lisbon.

[72]   P. Vilaça, *Fundamentos do Processo de Soldadura por Friccção linear: Análise experimental e modelação analítica*, (2003), Universidade Técnica de Lisboa, Lisbon.

[73]   J. P. M. Gandra, *Preliminary study on the production of functionally graded materials by friction stir processing*, (2010), Universidade Nova de Lisboa, Lisbon.

[74]   J. W. S. Hearle, *The use of the scanning electron microscope*, (1972), Pergamon Press Ltd, United-Kingdom.

[75]   CEN, *EN 10002-1 Metallic materials - Tensile testing*, (2001), CEN, Brussels.

[76]   CEN, *EN 910 - Destructive tests on weld in metallic materials - Bend tests*, (1996), CEN, Brussels.

[77]   J. G. F. Gonzalez, *Desenvolvimento e aplicação de sondas inovadoras de correntes induzidas para ensaios não destrutivos*, (2011), Universidade Nova de Lisboa, Lisbon.

[78]   Santos T, *Ensaios não destrutivos por correntes induzidas: Desenvolvimento e aplicação à soldadura por fricção linear*, (2009), Universidade Técnica de Lisboa, Lisbon

[79]   S. S. Rao, *Mechanical Vibrations – 3rd edition*, (1995), Addison-Wesley, Massachusetts.

[80]   George F. V. Voort, *Vol 09 – Metallography and Microstructures*, (2004), ASM International, USA.

ANNEXES

ANNEX A – OPERATING PARAMETERS, EQUIPMENT AND NOTES

Table T1 – list of fixed parameters throughout the experiment

Tilt angle (°)	Plunge speed (mm/s)	Dwell time (s)
0.5	0.1	4.0

Table T2 – list of variable parameters, reinforcements materials used and tool dimensions throughout the experiment

No.	Code	Groove geometry	Reinforcing material	Pitch (mm /rot)	(rev/min)	V (mm/min)	PD (mm)	PH (mm)	Force (KN)	Control Mode	Comments
1	1.4	No groove	N/A	0.0625	800	50	- 1.40	1.48	2400	PC	
2	1.5	No groove	N/A	0.0625	800	50	- 1.50	1.48	2400	PC	
3	1.6	No groove	N/A	0.0625	800	50	- 1.60	1.48	2400	PC	Excessive flash formation
4	N1	Circular 0.8	Wire 0.8	0.0625	800	50	- 1.30	1.48	2400	PC	U
5	N2	Circular 0.8	Wire 0.8	0.1250	800	100	- 1.30	1.48	2400	PC	U
6	N2 VID	Circular 0.8	Wire 0.8	0.1250	800	100	- 1.30	1.48	2400	PC	U
7	N3	Circular 0.8	Wire 0.8	0.1250	800	100	- 1.20	1.48	2400	PC	V decreased to 70 mm/min from middle onwards
8	N4	Circular 0.8	Wire 0.8	0.0625	800	50	- 1.20	1.48	2400	PC	U
9	N5	Circular 0.8	Wire 0.8	0.1111	900	100	- 1.20	1.48	2400	PC	
10	N6	Circular 0.8	Wire 0.8	0.1000	1000	100	- 1.20	1.48	2400	PC	U
11	N7	Circular 0.8	Wire 0.8	0.0875	800	70	- 1.20	1.48	2400	PC	U
12	N8	Circular 0.8	Wire 0.8	0.1111	900	100	- 1.20	1.48	2400	PC	U

13	N9	Circular 0.8	Wire 0.8	0.1111	900	100	- 1.20	1.56	2400	PC	PD increased to -1.3, -1.4 and -1.5 mm
14	N10	Circular 0.8	Wire 0.8	0.1111	900	100	- 1.55	1.56	2400	PC	Excessive deformation and flash, U
15	N11	Circular 0.8	Wire 0.8	0.1111	900	100	- 1.40	1.56	2400	PC	Excessive deformation, U
16	N12	Circular 0.8	Wire 0.8	0.1250	800	100	- 1.30	1.56	2400	PC	Pin point contacted with wire, waved surface due to excess vibration, U
17	N13	Circular 0.8	Wire 0.8	0.1250	800	100	- 1.20	1.48	2400	PC	Wrong initial conditions, U
18	N14	Circular 0.8	Wire 0.8	0.1250	800	100	- 1.20	1.48	2400	PC	PH reduced, overall good weld stability
19	N15	Circular 0.8	Wire 0.8	0.1250	800	100	- 1.30	1.48	2400	PC	Joint failed while handling
20	N16	Circular 0.8	Wire 0.8	0.0875	800	70	- 1.30	1.48	2400	PC	U
21	N17	Circular 0.8	Wire 0.8	0.1000	800	80	- 1.25	1.48	2400	PC	Started with shear lip formation, PD increased to -1.15 mm than back to 1.25 mm
22	N18	Circular 1.0	Wire 0.8	0.1000	800	80	- 1.25	1.48	1200	FC	Excess vibration, good position control, force increased to 1300 KN from middle onwards
23	N19	Circular 1.0	Wire 0.8	0.1000	800	80	- 1.25	1.48	1200	FC	Multi-pass OR=0.8, excess vibration, insufficient fixturing
24	N20	No groove	N/A	0.1000	800	80	- 1.25	1.48	1200	FC	Force increased to 1300, 1400 and 1500 KN along the weld
25	N21	No groove	N/A	0.1000	800	80	- 1.25	1.48	1400	FC	Good surface quality, overlapping by the AS
26	B1.1	Circular 1.0	Wire 0.8	0.1000	800	80	- 1.25	1.48	1300	FC	Full overlapping with opposite V velocities
27	B1.2	Circular 1.0	Wire 0.8	0.1000	800	80	- 1.25	1.48	1300	FC	
28	B2.1	Circular 1.0	Wire 0.8	0.1000	800	80	- 1.25	1.48	1300	FC	Increase force from middle onwards weld due to lack of penetration, featuring dissimilar welding characteristics
29	B2.2	Circular 1.0	Wire 0.8	0.1000	800	80	- 1.25	1.48	1300	FC	O-RS
30	B3.1	No groove	N/A	0.1000	800	80	- 1.25	1.48	1300	FC	
31	B3.2	No groove	N/A	0.1000	800	80	- 1.25	1.48	1300	FC	O-RS

IV

32	B4	Circular 1.0	Wire 0.8	0.1000	800	80	- 1.25	1.48	1300	FC	Typical front edge flash reentering pool defect
33	C1.1	Circular 1.0	Wire 0.8	0.1000	800	80	- 1.35	1.48	1300	FC	Forced increased to 1500 KN at the end
34	C1.2	Circular 1.0	Wire 0.8	0.1000	800	80	- 1.35	1.48	1400	FC	O-AS, Same defect as the pass before, probably due to base material
35	C2.1	Circular 1.0	Wire 0.8	0.1000	800	80	- 1.35	1.48	1400	FC	Bade positioned steel wire originated a depression of the upper plate
36	C2.2	Circular 1.0	Wire 0.8	0.1000	800	80	- 1.35	1.48	1400	FC	O-RS, more shear lip on the passes interface
37	C3.1	Circular 1.0	Wire 0.8	0.1000	800	80	- 1.45	1.56	1400	FC	Operating without liquid cooling, excessive fixturing force deformed the upper plate to a convex shape
38	C3.2	Circular 1.0	Wire 0.8	0.1000	800	80	- 1.45	1.56	1400	FC	O-AS
39	C4.1	Circular 1.0	Wire 0.8	0.1000	800	80	- 1.45	1.56	1400	FC	
40	C4.2	Circular 1.0	Wire 0.8	0.1000	800	80	- 1.45	1.56	1400	FC	O-AS
41	C4.3	Circular 1.0	Wire 0.8	0.1000	800	80	- 1.45	1.56	1400	FC	O-AS
42	D1.1	Rect. 3x1	NiTi 2.8x0.9	0.1000	800	80	- 1.45	1.56	1400	FC	Lack of fixturing
43	D1.2	Rect. 3x1	NiTi 2.8x0.9	0.1000	800	80	- 1.45	1.56	1400	FC	O-AS, relocated the weld pass for the new pass
44	D1.3	Rect. 3x1	NiTi 2.8x0.9	0.1000	800	80	- 1.45	1.56	1400	FC	O-AS, best results for this trial
45	D2.1	Rect. 3x1	NiTi 2.8x0.9	0.1000	800	80	- 1.45	1.56	1400	FC	
46	D2.2	Rect. 3x1	NiTi 2.8x0.9	0.1000	800	80	- 1.45	1.56	1400	FC	O-AS
47	D3.1	Rect. 3x1	NiTi 2.8x0.9	0.1000	800	80	- 1.45	1.56	1400	FC	Compressed air (CA) used to blow flash formation away from the front edge of the tool (surface material intake)
48	D3.2	Rect. 3x1	NiTi 2.8x0.9	0.1000	800	80	- 1.45	1.56	1400	FC	O-AS, CA

				0.1000	800	80	- 1.45	1.56	1400	FC	CA
49	D4.1	No groove	N/A								
50	D4.2	No groove	N/A	0.1000	800	80	- 1.45	1.56	1400	FC	O-AS, CA
51	D5.1	Rect. 3x1	NiTi 2.8x0.9	0.1000	800	80	- 1.65	1.64	1400	FC	CA, Higher PH reduces tool vibration and produces a smoother surface
52	D5.2	Rect. 3x1	NiTi 2.8x0.9	0.1000	800	80	- 1.65	1.64	1400	PC	O-AS, CA
53	D6.1	No groove	N/A	0.1000	800	80	- 1.65	1.64	2400	PC	CA, Machine operated on default parameters, excessive heat and shear lip
54	D6.2	No groove	N/A	0.1000	800	80	- 1.65	1.64	2000	FC	O-AS, CA
55	D7.1	Rect. 3x1	NiTi 2.8x0.9	0.1000	800	80	- 1.65	1.64	1800	FC	CA
56	D7.2	Rect. 3x1	NiTi 2.8x0.9	0.1000	800	80	- 1.65	1.64	1800	FC	O-AS, CA
57	D8.1	No groove	N/A	0.1000	800	80	- 1.65	1.64	1800	FC	CA
58	D8.2	No groove	N/A	0.1000	800	80	- 1.65	1.64	1800	FC	O-AS, CA
59	D9.1	Rect. 3x1	NiTi 2.8x0.9	0.1000	800	80	- 1.65	1.64	1800	FC	CA
60	D9.2	Rect. 3x1	NiTi 2.8x0.9	0.1000	800	80	- 1.65	1.64	1800	FC	O-AS, CA
61	D9.3	Rect. 3x1	NiTi 2.8x0.9	0.1000	800	80	- 1.65	1.64	1800	FC	O-AS, CA
62	D10.1	Rect. 3x1	NiTi 2.8x0.9	0.1000	800	80	- 1.65	1.64	1800	FC	CA, No water cooling, faulty 'zero position', good surface finishing
63	D10.2	Rect. 3x1	NiTi 2.8x0.9	0.1000	800	80	- 1.65	1.64	1800	FC	O-AS, CA, force reduced from the middle onwards
64	D10.3	Rect. 3x1	NiTi 2.8x0.9	0.1000	800	80	- 1.65	1.64	1800	FC	O-AS, CA, excessive shear lip and defects
65	D10.4	Rect. 3x1	NiTi 2.8x0.9	0.1000	800	80	- 1.65	1.64	1800	FC	O-AS, CA

VI

66	D11.1	Rect. 3x1	NiTi 2.8x0.9	0.1000	800	80	- 1.65	1.64	1800	FC	CA
67	D11.2	Rect. 3x1	NiTi 2.8x0.9	0.1000	800	80	- 1.65	1.64	1800	FC	O-AS, CA, force recalibrate to cope with initial shear lip
68	D11.3	Rect. 3x1	NiTi 2.8x0.9	0.1000	800	80	- 1.65	1.64	1800	FC	O-AS, CA, force recalibrate to cope with initial shear lip
69	D12.1	No groove	N/A	0.1000	800	80	- 1.65	1.64	1800	FC	CA, due to upper plate warp produced wider weld beads due to tool increased plunged
70	D12.2	No groove	N/A	0.1000	800	80	- 1.65	1.64	1800	FC	O-AS, CA
71	D12.3	No groove	N/A	0.1000	800	80	- 1.65	1.64	1800	FC	O-AS, CA
72	D13.1	No groove	N/A	0.1000	800	80	- 1.65	1.64	1800	FC	CA
73	D13.2	No groove	N/A	0.1000	800	80	- 1.65	1.64	1800	FC	O-AS, CA
74	D13.3	No groove	N/A	0.1000	800	80	- 1.65	1.64	1800	FC	O-AS, CA
75	D14.1	No groove	N/A	0.1000	800	80	- 1.65	1.64	1800	FC	CA
76	D14.2	No groove	N/A	0.1000	800	80	- 1.65	1.64	1800	FC	O-AS, CA
77	D14.3	No groove	N/A	0.1000	800	80	- 1.65	1.64	1800	FC	O-AS, CA
78	D15.1	Circular 1.0	Wire 0.8	0.1000	800	80	- 1.65	1.64	1800	FC	CA
79	D15.2	Circular 1.0	Wire 0.8	0.1000	800	80	- 1.65	1.64	1800	FC	O-AS, CA
80	D15.3	Circular 1.0	Wire 0.8	0.1000	800	80	- 1.65	1.64	1800	FC	O-AS, CA
81	D16.1 VID	Circular 1.0	Wire 0.8	0.1000	800	80	- 1.65	1.64	1800	FC	CA
82	D16.2 VID	Circular 1.0	Wire 0.8	0.1000	800	80	- 1.65	1.64	1800	FC	O-AS, CA
83	D16.3 VID	Circular 1.0	Wire 0.8	0.1000	800	80	- 1.65	1.64	1800	FC	O-AS, CA
84	D17.1	Circular 1.0	Wire 0.8	0.1000	800	80	- 1.65	1.64	1800	FC	CA
85	D17.2	Circular 1.0	Wire 0.8	0.1000	800	80	- 1.65	1.64	1800	FC	O-AS, CA

86	D17.3	Circular 1.0	Wire 0.8	0.1000	800	80	- 1.65	1.64	1800	FC	O-AS, CA
87	D18.1	Circular 1.0	Wire 0.8	0.1000	800	80	- 1.65	1.64	1800	FC	CA
88	D18.2	Circular 1.0	Wire 0.8	0.1000	800	80	- 1.65	1.64	1800	FC	O-AS, CA, Increased force from middle onwards
89	D18.3	Circular 1.0	Wire 0.8	0.1000	800	80	- 1.65	1.64	1800	FC	O-AS, CA
90	D19.1	Rect. 3x1	NiTi 2.8x0.9	0.1000	800	80	- 1.65	1.64	1800	FC	CA
91	D19.2	Rect. 3x1	NiTi 2.8x0.9	0.1000	800	80	- 1.65	1.64	1800	FC	O-AS, CA
92	D19.3	Rect. 3x1	NiTi 2.8x0.9	0.1000	800	80	- 1.65	1.64	1800	FC	O-AS, CA
93	D19.4	Rect. 3x1	NiTi 2.8x0.9	0.1000	800	80	- 1.65	1.64	1800	FC	O-AS, CA
94	D20.1	Rect. 3x1	NiTi 2.8x0.9	0.1000	800	80	- 1.65	1.64	1800	FC	CA
95	D20.2	Rect. 3x1	NiTi 2.8x0.9	0.1000	800	80	- 1.65	1.64	1800	FC	O-AS, CA
96	D21.1	Rect. 3x1	NiTi 2.8x0.9	0.1000	800	80	- 1.65	1.64	1800	FC	CA
97	D21.2	Rect. 3x1	NiTi 2.8x0.9	0.1000	800	80	- 1.65	1.64	1800	FC	O-AS, CA
98	D22.1	No groove	N/A	0.1000	800	80	- 1.65	1.64	1800	FC	CA
99	D22.2	No groove	N/A	0.1000	800	80	- 1.65	1.64	1800	FC	O-AS, CA

Annotations: O-AS – Overlapping by the advancing side; O-RS – overlapping by the retreating side; CA – compressed air; PC – position control; FC – force control; Circular 0.8 – circular section with 0.8 diameter; Circular 1.0 – circular section with 0.8 diameter; Rect. 3x1 – rectangular cross section with 3.0 x 1.0 (width x thickness in mm); Wire 0.8 – steel wire with 0.8 mm diameter; NiTi 2.8x0.9 – NiTi stripe with 2.9 x 0.9 (width x thickness in mm); U – Unstable wire twisting

VIII

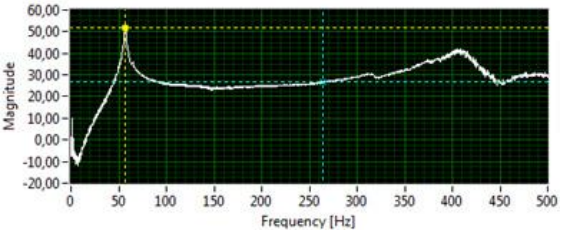# ANNEX B – Natural frequency response charts
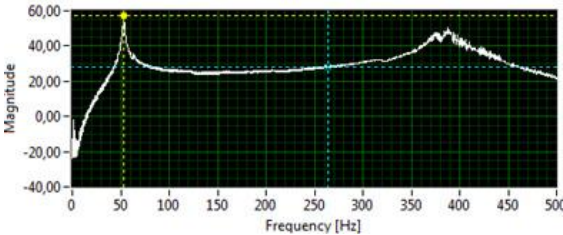
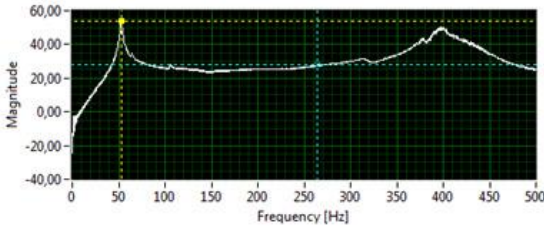Sample D9 at ambient temperature
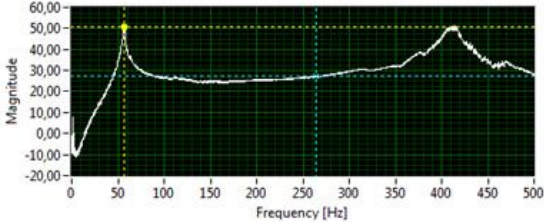
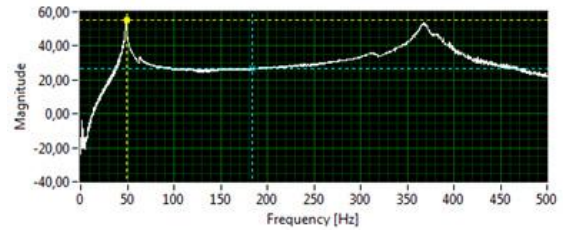Sample D9 after 1 minute in liquid nitrogen
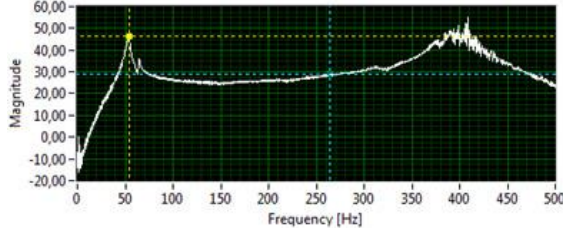
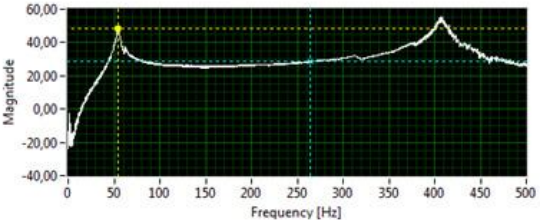Sample D13 after 1 minute in liquid nitrogen

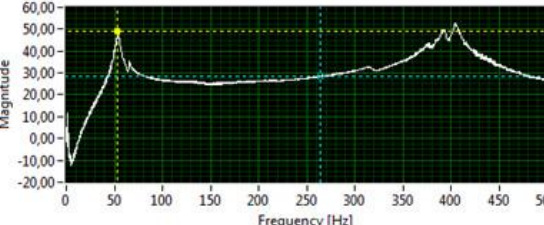Sample D9 after 5 minutes in liquid nitrogen

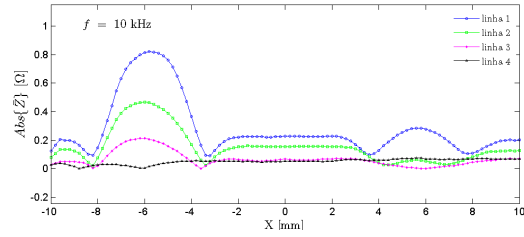Sample D9 after reheating

Sample D15 at ambient temperature
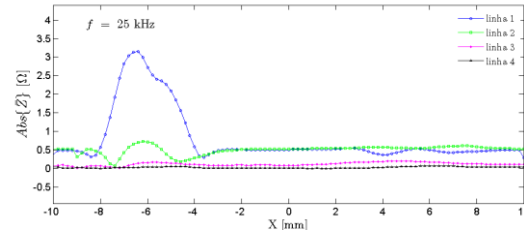

Sample D13 at ambient temperature
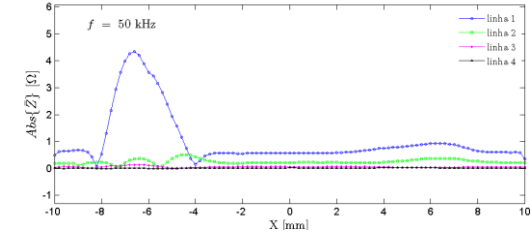

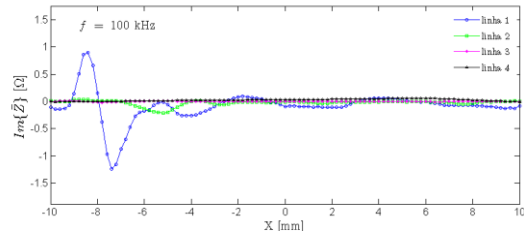Sample D13 after 5 minutes in liquid nitrogen

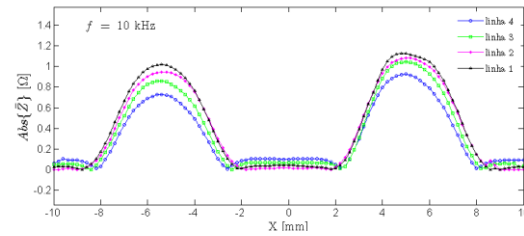# ANNEX C – Eddy currents charts

Surface of sample D9 tested with10 KHz

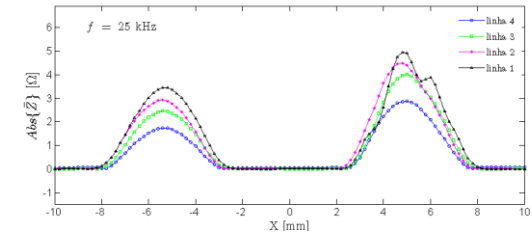Surface of sample D9 tested with 25 KHz

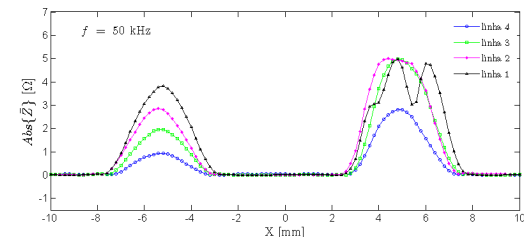Surface of sample D9 tested with 50 KHz

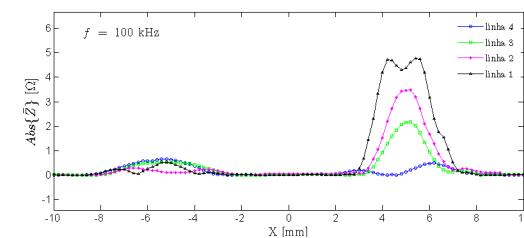Surface of sample D9 tested with 100 KHz
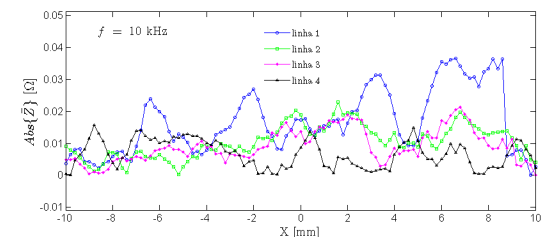

Bottom of sample D9 tested with 10 KHz

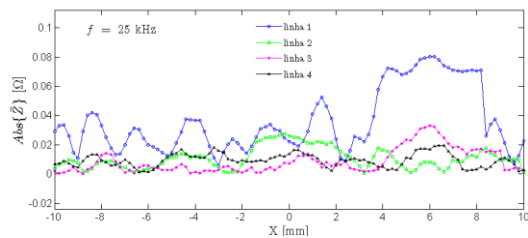Bottom of sample D9 tested with 25 KHz

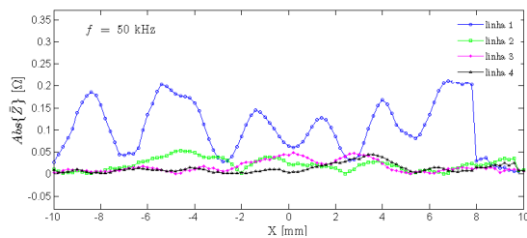Bottom of sample D9 tested with 50 KHz

Bottom of sample D9 tested with 100 KHz

Surface of sample D13 tested with 10 KHz

X

Surface of sample D13 tested with 25 KHz

Surface of sample D13 tested with 50 KHz

Surface of sample D13 tested with 100 KHz

Surface of sample D15 tested with 10 KHz

Surface of sample D15 tested with 10 KHz (without
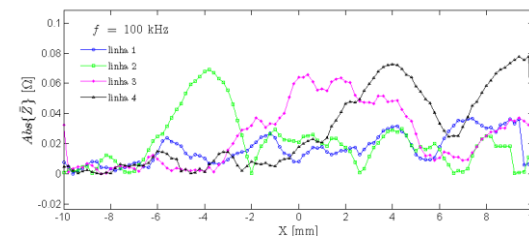
step 1)

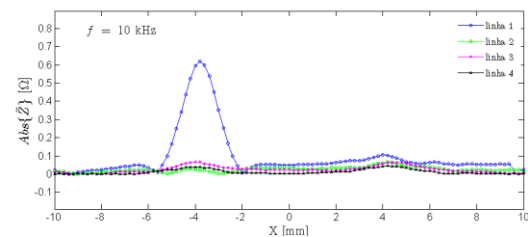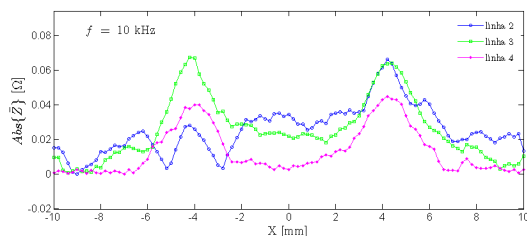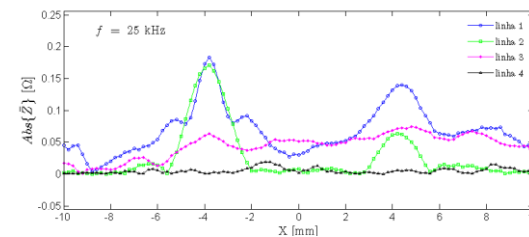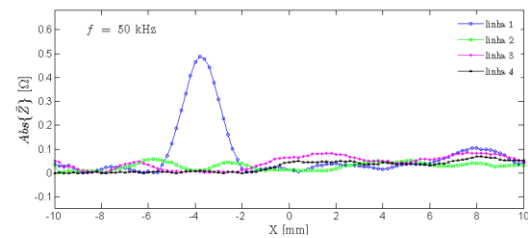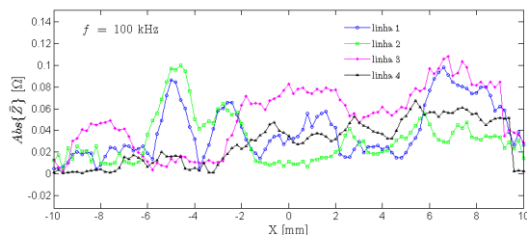Surface of sample D15 tested with 25 KHz

Surface of sample D15 tested with 50 KHz

Surface of sample D15 tested with 100KHz

ANNEX D – Operating procedures of FSW

Generally, solid state FSW is known to be a technology with ease of production and replication. Previous to work welding, a set of preparatory tasks should be achieved:

   i.   Acquire the working material.

   ii.   Cut and machine sheet or plates to pre-defined dimensions and tolerances, guarantying a good perpendicularity.

   iii.   Grinding and alcohol cleaning until no flash or grease is depicted.

   iv.   Mount the material and restrain on the fixturing system of the FSW worktable. The most suitable fixturing should be used according to material and weld dimensions

After, Friction stir welding procedures adopted should be:

1. Check cooling water level, clean and mount the FSW tool into the machines spindle shaft, cover all threads with Teflon.
2. Turn on cooling system and verify if the water flow is correct.
3. Set-up welding parameters into the HMI console.
4. Set-up 'zero position' at the Z-axis.
5. Readjust the material longitudinal axis with the pin point along the X-axis.
6. Fasten the fixturing system firmly to guarantee enough material restrain without deforming the upper plate.
7. Set-up start and end X and Y positions.
8. Press 'start' welding once to initiate the tool rotating movement.
9. Press 'start' again to initiate the welding process
10. Upon finishing the welding process wait for the tool achieve its final position
11. Unfasten the welded material
12. Mark the welded material
13. If the user wants to repeat the process, go back to task no 1.

ANNEX E – Material characterization procedures

E.1 – Metallography analysis

A macro/micro visual analysis requires a sample preparation to reveal a clean scratch free cross section of the welded material. The following procedure is established to mount the sectioned samples on cold epoxy resin small circular cups, with the following tasks:

1. From the welded sample section transversal 20x20 (mm) specimens.
2. Check the edges for flash or others residues and clean them.
3. Mount the samples pre-mixed Epoxy resin and epoxy hardener at given quantities (check the supplier technical specifications).
4. Wait 1 to 2 days for the epoxy solution to harden.
5. Remove the mounted samples from the cups.
6. Grind the specimens with grinder-polishing rotating machine with water supply.
7. Use silicon carbide water grinding discs starting with P400, P600, P1200 and P2500 grit in this order, until a scratch free surface is depicted in microscopy.
8. Proceed with polishing using a polishing cloth with alumina suspension solution of 1 μm.
9. Wash with running water and blow dry.
10. Check for polishing surface in microscopy, redo step 8 and 9 until the desired surface finishing.
11. Photograph and identify.
12. Etch the mounted sample with Keller reagent (for aluminium alloys [80]), to reveal grain boundaries and second phase particles, use Keller composition according to table T 3. Dip the samples for 30 seconds intervals until SZ is visible.
13. Clean the etched surface with running water to eliminate any etching solution remaining, and blow dry.
14. Perform macro and micrograph analysis and catalogue.
15. Keep the mounted polished and etched samples in a dust and humidity free recipient.

Table T3 – Keller reagent chemical composition

Solution	Quantity
HNO_3	2.5 mL
HCl	1.5 mL
HF	1.0 mL
H_2O	95 mL

E.2 – Tensile test procedures

After machined to desired geometry, according to the European tensile standards EN 10002-1 (2001) [75]. The tensile procedures followed these tasks:

1. Calculate the reduce area of sample cross section; measure width and thickness in three different points of the utile length to calculate an average.
2. Measure reduced area utile length.
3. Set-up the sample and securely fasten the machine grippers (sample width must be inferior to the grip width).
4. Assemble the extensometer in the utile area of the sample with an initial aperture of 25 mm.
5. Set-up the geometrical parameters and upward velocity into the machine's software program.
6. Initialize the tensile test.
7. Stop after sample failure.
8. Save data, measure final length and catalogue.
9. Repeat from task no 1 for further samples.

E.3 – Bending test procedures

After machined to desired geometry, according to the three point flexture bending European tensile standards EN 910 (1996) [76]. The tensile procedures followed these tasks:

1. Set the span distance between rollers.
2. Check for parallelism between the transversal supporting point rollers and the upper roller.
3. Calculate area of sample cross section; measure width and thickness in three different points of the utile length to calculate an average.
4. Place the sample on the rollers (sample width must be inferior to roller width).
5. Align the sample's bead center with the roller's center.
6. Set-up the geometrical parameters and upward velocity into the machine's software program.
7. Initialize the tensile test.
8. Stop after sample collapse or angle restrictions (when the upper gripper is about to contact the bent sample).
9. Save data, measure final length and catalogue.
10. Repeat from task no 3 for further samples.

E.4 – Vibration test procedures

Vibration testing was made on a cantilever configuration, with a composite beam, a piezoelectric receiver, a hammer equipped with an accelerometer and a clamp for tightening testing samples to the worktable.

For cooled specimens: (Careful: work with heat resistant gloves and tweezers)

1. Open the liquid nitrogen container
2. Sink the sample carefully to avoid any liquid spill
3. Wait until the wanted cooling is achieved (2 to 5 minutes in this investigation)
4. Remove samples with a pair of tweezers
5. Mount the specimen on the working table following further steps.

Experimental set-up:

1. Mount the composite beam on a fixed-free condition
2. Check for perpendicularity between sample and worktable
3. Securely fasten the fixture system to guarantee a vibration free clamping
4. Tightly couple the piezoelectric receiver into the sample's welded surface
5. Start the program at Lab View
6. Hammer the previously drawn beam target, wait 2s
7. Repeat the last step 5 times
8. Stop the program
9. Calculate average and output graphics

For reheated samples, a blow drier can be used to heat the composites until a dry surface is depicted, after the testing should be repeated (without the need to disassemble the composite).

E.5 – Eddy currents procedures

Electromagnetic induced field testing used an Olympus™ pencil probe, with frequency range from 50KHZ to 500KHZ and 3 mm diameter. The methodology used to analyze the material electromagnetic induced field consisted in:

1. Mount sample onto the X–Y table and secure it;
2. Set a frequency on the Olympus® NORTEC 500 C device;
3. Set the pencil probe on top of the normalizing area;
4. Calibrate the angle;
5. Press null to zero normalize the impedance values;
6. Run the step motors in the LabVIEW® specially designed program;
7. Output the data files;
8. Repeat steps 1 to 7 for further testing.

Several conditions must be fulfilled in order to validate testing results, and those are:

- Avoid edge effect – eddy currents are distorted because they are unable to flow beyond the edge of a part – by start testing with an offset from the composite edge (the distance interval may be assessed by trial-and-error);
- Calibrate probe before each testing, use the same position for several tests in order to compare results between different passes;
- Guarantee an even probe, or lift-off, distance along the test width (small changes have strong effects on the field of the coil).

For electrical conductivity testing (in % IACS) with an Olympus probe 60 KHz pencil probe and an Olympus® NORTEC 500 C eddy current flaw detector, these steps should be followed:

1. The process requires the unit calibration upon each set of tests, a series of metallic plates, with normalized % IACS values, are used to normalized the impedance values according to electric conductivity (in % IACS);
2. Test any sample by deploying the pencil probe on top of any material, without lift-off;
3. Wait until the measured values stabilize;
4. Take note and repeat 2 to 3 steps for further testing.